ABSTRACT

Title of dissertation: THEORY OF GRAPHENE
                                TRANSPORT PROPERTIES

                                Qiuzi Li, Doctor of Philosophy, 2013

Dissertation directed by: Professor Sankar Das Sarma
                                Department of Physics

Graphene is of great fundamental interest and has potential applications in disruptive novel technologies. In order to study the novel phenomena in graphene, it is essential to understand its electron transport properties and in particular the main factors limiting its transport mobility. In this dissertation, we study the transport properties of graphene in the presence of electron-hole puddles induced by charged impurities which are invariably present in the graphene environment. We calculate the graphene conductivity by taking into account the non-mean-field two-component nature of transport in the highly inhomogeneous density and potential landscape, where activated transport across the potential fluctuations in the puddle regimes coexists with regular metallic diffusive transport. Our theoretical calculation explains the non-monotonic feature of the temperature dependent transport, which is experimentally generically observed in low mobility graphene samples. Our theory also predicts the existence of an intriguing "disorder by order" phenomenon in graphene transport where higher-quality (and thus more ordered) samples, while having higher mobility at high carrier density, will manifest more strongly insulating (and thus ef-

fectively more disordered) behavior as the carrier density is lowered compared with lower quality samples (with higher disorder), which exhibit an approximate resistivity saturation phenomenon at low carrier density near the Dirac point. This predicted behavior, simulating a metal-insulator transition, arises from the suppression of Coulomb disorder induced inhomogeneous puddles near the charge neutrality point in high quality graphene samples. We then study carrier transport through graphene on $SrTiO_3$ substrates by considering the relative contributions of Coulomb and resonant impurity scattering to graphene resistivity. We establish that the non-universal high-density behavior of $\sigma(n)$ in different graphene samples on various substrates arises from the competition among different scattering mechanisms, and it is entirely possible for graphene transport to be dominated by qualitatively different scattering mechanisms at high and low carrier densities. Finally, we calculate the graphene conductivity as a function of carrier density, taking into account possible correlations in the spatial distribution of the Coulomb impurity disorder in the environment. We find that the conductivity could increase with increasing impurity density if there is sufficient inter-impurity correlation present in the system.

THEORY OF GRAPHENE TRANSPORT PROPERTIES

by

Qiuzi Li

Dissertation submitted to the Faculty of the Graduate School of the
University of Maryland, College Park in partial fulfillment
of the requirements for the degree of
Doctor of Philosophy
2013

Advisory Committee:
Professor Sankar Das Sarma, Chair/Advisor
Professor Theodore Einstein
Professor Victor Galitski
Professor Christopher Jarzynski
Professor Victor Yakovenko

Dedication

To Haitan, Amelia and my parents

Acknowledgments

During these five years of my Ph.D. study, many people provided help in various forms. First and foremost, I would like to thank my advisor, Professor Sankar Das Sarma, for his constant guidance and encouragements. He has brought various research projects to my attention. I feel incredibly lucky to be able to work with him, and he remains a role model for me.

I would like to express my gratitude to Professor Xuedong Hu for his help and useful advice on my first research project in Maryland and on my job application. I am thankful to Professor Michael Fuhrer, as well as his group members, Dohun Kim and Jun Yan, for the stimulating discussions and for showing me their exciting experimental results. I acknowledge Euyheon Hwang for his patient and useful guidance in solving difficult and detailed problems. I appreciate the help from my other collaborators Enrico Rossi, Lukasz Cywinski, Dimitrie Culcer, Parag Ghosh, Jay Sau, and Sumanta Tewari. The collaboration with them has greatly improved my paper writing skills.

I thank Professor Victor Galitski and Professor Michael Levin for their wonderful graduate courses. I would also like to thank the entire dissertation committee for their time and effort, and for their valuable comments to improve the quality of the dissertation.

My life in Maryland would not be so enjoyable without so many friends. I owe my gratitude to three great friends, Jason, Jacob and Anne, who have provided much help throughout past five years here on my family. I have also enjoyed many

Table of Contents

List of Figures

List of Abbreviations

MLG	Monolayer Graphene
BLG	Bilayer Graphene
CNP	Charge Neutrality Point
SCBA	Self-Consistent Born Approximation
TFD	Thomas-Fermi-Dirac
EMT	Effective Medium Theory

Chapter 1

Introduction

Graphene, as a novel gapless two dimensional (2D) chiral electron-hole system, has attracted great interest in recent years, both experimentally and theoretically[1, 2, 3, 4, 5]. Its transport properties have been at the center of key fundamental and technological efforts with vast potential for applications in future nanotechnology[6]. For monolayer graphene (MLG), the fundamental interest arises from its unique linear chiral Dirac carrier dispersion with a zero energy gap between conduction and valence band[7, 8]. One of the most studied properties of graphene is its electrical conductivity as a function of the applied gate voltage which translates directly into the carrier density (n) dependent conductivity $\sigma(n)$ [1]. The functional dependence of $\sigma(n)$ at low temperatures contains information [1] about the nature of disorder in the graphene environment giving rise to the dominant resistive carrier scattering mechanism. The purpose of the this chapter is to give a brief review of the fundamental aspects of carrier transport in graphene.

The most important features of the experimentally observed $\sigma(n)$ [7, 8, 9, 10, 11, 12, 13] in graphene are: (1) a nonuniversal sample-dependent minimum conductivity $\sigma(n \approx 0) \equiv \sigma_{min}$ at the charge neutrality point (CNP) where the average carrier density vanishes; (2) a linearly increasing, $\sigma(n) \propto n$, conductivity with in-

creasing carrier density on both sides of the CNP up to some sample dependent characteristic carrier density; (3) a sublinear $\sigma(n)$ for high carrier density, making it appear that the very high density $\sigma(n)$ may be saturating.

In the remainder of this chapter, we will discuss the graphene transport at high and low carrier density separately.

1.1   Transport at high carrier density
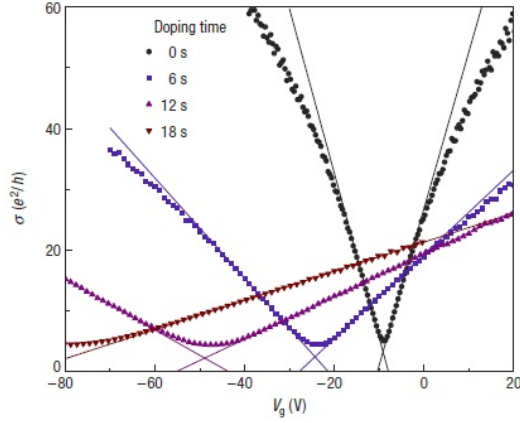
Figure 1.1: The conductivity versus gate voltage for the pristine sample and three different doping concentrations taken at 20 K in ultrahigh vacuum. Adapted from Fig. 2 of Ref. [10].

The experiments (Fig. 1.1) showed that the density dependence of conductivity is roughly linear away from the Dirac point. In addition, the density dependent conductivity shows a sublinear behavior when the carrier density is further increased. For lower mobility samples, the carrier density dependent conductivity is more linear.

1.1.1 Boltzmann transport theory

These features are well described by the Boltzmann transport theory, which involves an interplay between long-range charged impurity and short-range disorder scattering. From the Boltzmann transport theory, within the "relaxation time approximation", the electronic conductivity σ is given by the following equation[1]:

$$\sigma(n, T) = \frac{e^2}{2} \int d\epsilon D(\epsilon) v_F^2 \tau(\epsilon, T) \left(-\frac{\partial f(\epsilon)}{\partial \epsilon} \right) \quad (1.1)$$

where e is the electron charge, $D(\epsilon) = 2\epsilon/(\pi \hbar^2 v_F^2)$ the density of states of MLG at energy ϵ, $v_F = 10^6$ m/s the Fermi velocity, $f(\epsilon) = 1/(1 + e^{\beta(\epsilon-\mu)})$ the Fermi-Dirac distribution, $\beta = 1/(k_B T)$, μ the chemical potential, and τ the total transport mean free time due to the electron scattering off quenched disorder. One thing that we must emphasize is that Eq. (1.1) is valid as long as the system is homogeneous (i.e. spatial density fluctuations effects are small enough so that the average density n is a meaningful quantity, an approximation which would break down for low n).

The energy dependent scattering time $\tau(\epsilon)$ due to quenched disorder is given by

$$\frac{\hbar}{\tau(\epsilon_{p\mathbf{k}})} = 2\pi n_{dis} \int \frac{d^2 k'}{(2\pi)^2} |\langle V_{p\mathbf{k},p\mathbf{k}'}\rangle|^2 g(\theta_{\mathbf{kk}'})$$

$$\times [1 - \cos\theta_{\mathbf{kk}'}] \, \delta(\epsilon_{p\mathbf{k}'} - \epsilon_{p\mathbf{k}}) \quad (1.2)$$

where $\epsilon_{p\mathbf{k}} = p\hbar v_F k$ is the carrier energy for the pseudospin state "p" and $\mathbf{k}$ is the 2D wave vector, $\langle V_{p\mathbf{k},p\mathbf{k}'}\rangle$ is the matrix element of the impurity disorder potential in the system environment, $\theta_{\mathbf{kk}'}$ is the scattering angle between in- and out- wave vectors $\mathbf{k}$ and $\mathbf{k}'$, $g(\theta_{\mathbf{kk}'}) = [1 + \cos\theta_{\mathbf{kk}'}]/2$ is a wave function form factor associated

3

with the chiral nature of MLG (and is determined by its band structure). n_{dis} is the appropriate 2D areal concentration of the impurity centers giving rise to the random disorder potential[14]. We consider two different kinds of disorder scattering mechanisms: (i) randomly distributed screened Coulomb disorder for which $n_{dis}|\langle V_{p\mathbf{k},p\mathbf{k'}}\rangle|^2 = n_{imp}|V(q)/\varepsilon(q)|^2$, where $V(q) = 2\pi e^2/(\kappa q)$ is the Fourier transform of the 2D Coulomb potential in an effective background lattice dielectric constant κ and $\varepsilon(q) \equiv \varepsilon(q,T) = 1 + V(q)\Pi(q,T)$ is the 2D finite temperature static RPA dielectric function[15, 16, 17]. $\Pi(q,T)$ is the irreducible finite temperature polarizability function, which is given by the bare bubble diagram[17]:

$$\Pi(q,T) = -\frac{4}{L^2}\sum_{\mathbf{k},s,s'}\frac{f_{s,\mathbf{k}} - f_{s',\mathbf{k'}}}{\epsilon_{s,\mathbf{k}} - \epsilon_{s',\mathbf{k'}}}g(\theta_{\mathbf{kk'}}) \tag{1.3}$$

with $s, s' = \pm 1$. Note that we use n_{imp} to denote the charged impurity density; (ii) short-range disorder for which $n_{dis}|\langle V_{p\mathbf{k},p\mathbf{k'}}\rangle|^2 = n_d V_0^2$ where n_d is the 2D impurity density and V_0 is a constant short-range (i.e. a δ-function in real space) potential strength. Note that the use of the Born approximation for short-range disorder requires weak scattering condition[18], which is verified by the disorder parameters we use in our calculation.

To minimize the number of parameters entering the theory we have assumed that the impurities are randomly distributed in a 2D plane located at an effective distance d from graphene. It is straightforward to include in the theory a more complex three-dimensional distribution of quenched impurities, but given the lack of experimental information about the distribution of unintentional and unknown quenched impurity disorder in the system, it is theoretically more meaningful to use

4

a minimal model with just two unknown parameters n_{dis} and d, which can simulate essentially any realistic disorder distribution in an approximate manner– we note that $d = 0$ implies that the charged impurities are simply located on the graphene surface.

At zero temperature, the long-range Coulomb disorder leads to the linear density dependent conductivity, [1].

$$\sigma_{imp} = \frac{e^2}{h} \frac{n}{2n_{imp}r_s^2 G_1(r_s)} \tag{1.4}$$

where $r_s = e^2/(\hbar v_F \kappa)$ is the graphene fine structure constant and $G_1(x) = \frac{\pi}{4} + 6x - 6\pi x^2 + 4x(6x^2 - 1)g(x)$ with $g(x) = \operatorname{sech}^{-1}(2x)/\sqrt{1 - 4x^2}$ for $x < \frac{1}{2}$ and $\sec^{-1}(2x)/\sqrt{4x^2 - 1}$ for $x > \frac{1}{2}$.

On the other hand, the short-range disorder scattering time τ_{sd} is given by[1]

$$\frac{\hbar}{\tau_{sd}(\epsilon_{\mathbf{k}})} = \frac{k}{4\hbar v_F} n_{sd} V_0^2 \tag{1.5}$$

where n_{sd} is the 2D short-range impurity density and V_0 is a constant short-range (i.e. a δ-function in real space) potential strength. The conductivity at low temperature induced by this short-range impurity has the following form,

$$\sigma_{sd} = \frac{8e^2}{h} \frac{(\hbar v_F)^2}{n_{sd} V_0^2} \tag{1.6}$$

which is independent of carrier density ($\sigma(n) \sim$ constant).

1.2 Transport at low carrier density

Close to the Dirac point, the random charged impurity induced disorder potential causes the carrier density landscape to become strongly inhomogeneous, a
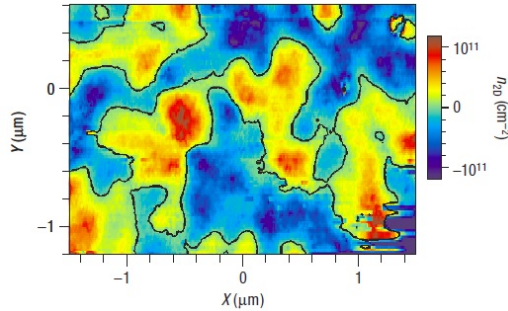
Figure 1.2: Carrier density profile map at the CNP with a scalable single-electron transistor. Adapted from Fig. 3(a) of Ref. [19].

fact that has been observed in Ref. [19]. Fig. 1.2 shows the experimental observation of electron-hole puddles in graphene using scanning single-electron transistor. The inhomogeneous puddles control transport properties of graphene at low density.

1.2.1 Self-consistent theory

Two theories have been proposed to explain the transport properties of graphene close to the Dirac point. The first one is called the self-consistent theory. The self-consistent theory is needed because the increased charged impurity density will increase the induced potential fluctuations and the induced carrier density. An increased carrier density screens more effectively which decreases the potential fluctuations and decreases the induced carrier density. Within the random phase approximation, the potential fluctuation can be calculated as[20]:

$$s^2 = 2\pi n_{imp} \left(\frac{e^2}{\kappa}\right)^2 C_0(r_s, a = 4k_F d) \tag{1.7}$$

where

$$
\begin{aligned}
C_0(r_s, a) &= -1 + \frac{2e^{-a}r_s}{1+2r_s} + \frac{4E_1[a]}{(2+\pi r_s)^2} \\
&\quad + e^{2r_s a}(1+2r_s a)(E_1[2r_s a] - E_1[a + 2r_s a]),
\end{aligned}
\tag{1.8}
$$

6

and $E_1[z] = \int_z^\infty t^{-1}e^{-t}dt$ is the exponential integral function. The difficulty arises from the fact that the function C_0 depends on the density via the Fermi wavevector k_F that, in the presence of disorder, at the Dirac point cannot, because of fluctuations, be taken to be simply zero. In the self-consistent approximation one assumes that at the Dirac point the system can be approximated by a homogeneous system having an effective carrier density $\hat{k}_F^2 = \pi\hat{n}$ such that $\hat{E}_F^2 = s^2$. Using this relation and Eq. (1.7) we obtain the following self-consistent equation for the carrier density at the CNP:

$$\frac{n^*}{n_{imp}} = 2r_s^2 C_0(r_s, a = 4d\sqrt{\pi n^*}). \tag{1.9}$$

By solving Eq. (1.9) self-consistently, we obtain the value of n^*, leading to an approximately constant minimum conductivity by putting n^* in to Eq. 1.4. This simple self-consistent theory has been found to be in good agreement with experimental measurement at low temperatures[10]. However, this theory did not include the highly heterogeneous structure near the charge neutrality point and the thermally activation effects at finite temperatures, which then cannot explain the observed nonmonotonic temperature-dependent transport in low mobility graphene samples [21].

1.2.2 Thomas-Fermi-Dirac theory

A more elaborate approach to consider the density inhomogeneity effects is the Thomas-Fermi-Dirac-Theory (TFDT) first introduced in Ref. [22]. In the TFDT, similarly to the Density Functional Theory (DFT), the energy of the system is given
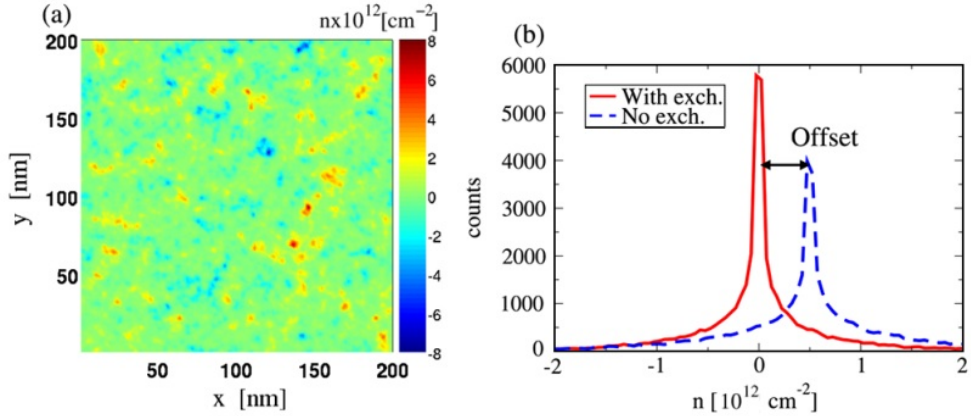
Figure 1.3: TFDT Results at the Dirac point for a disorder realization with $n_{imp} = 10^{12}$ cm^{-2}, $d = 1$ nm, and $\kappa = 2.5$. (a) Color plot of $n(\mathbf{r})$. (b) Density distribution for $n(\mathbf{r})$ shown in (a). Adapted from Ref. [22].

by a functional of the density profile $n(\mathbf{r})$, which can be calculated by minimizing the following energy functional $E[n]$[22].

$$E[n] = \hbar v_F \left[\frac{2\sqrt{\pi}}{3} \int d^2 r \, sgn(n)|n|^{3/2} + \frac{r_s}{2} \int d^2 r \int d^2 r' \frac{n(\mathbf{r})n(\mathbf{r}')}{|\mathbf{r} - \mathbf{r}'|} \right.$$
$$\left. + \frac{E_{xc}[n]}{\hbar v_F} + r_s \int d^2 r V_D(\mathbf{r})n(\mathbf{r}) - \frac{\mu}{\hbar v_F} \int d^2 r n(\mathbf{r}) \right] \qquad (1.10)$$

The energy functional $E[n]$ includes the charged impurity induced disorder potential, exchange effects and non-linear screening effects. By minimizing the Thomas-Fermi energy functional, we can obtain the density profile and potential distribution function. Fig. 1.3 shows the density profile at the Dirac point, where electron and hole puddles are almost equally distributed. The results of TFDT are visually very similar to the ones observed in experiments [19, 23], but a quantitative comparison can be achieved by calculating the disorder-averaged statistical properties.

The great advantage of a functional formalism is that it is not perturbative with respect to the spatial fluctuations of the carrier density and therefore can take into account nonlinear screening effects that dominate close to the Dirac point.

TFDT is just well-suited to describe the situation with large disorder-induced spatial density inhomogeneity as in the low carrier density case whereas in the high-density situation, it simply gives the homogeneous density result with small fluctuations around the average density. In the TFDT, in contrast to DFT, also the kinetic energy term is replaced by a density functional. This simplification makes the TFDT very efficient computationally and therefore able to obtain disorder averaged quantities, a task that cannot be accomplished using DFT. As long as the characteristic length-scale over which the density varies is larger than the local Fermi wavelength λ_F, i.e. $|\nabla n/n|^{-1} \gg \lambda_F$, [22, 24, 25] the TFDT returns reliable results [22, 26, 27]. It has been showed that the condition $|\nabla n/n|^{-1} \gg \lambda_F$ is satisfied in typical experimental conditions [22] . Close to the charge neutrality point (CNP) the density inside the electron-hole puddles is always different from zero (so that λ_F is always finite) and of the order of n_{rms} (root-mean-square of the density fluctuation). The great advantage of TFDT over DFT (to which TFDT is an approximation, as it uses the non-interacting kinetic energy functional) is that its relative numerical and computational ease enables one to use it for the calculation of transport properties using the computed ground state inhomogeneous spatial density profile, which would be completely computationally impossible for DFT to do.

Using the TFDT we can characterize completely the carrier density profile in the presence of a disorder potential. We can obtain the typical length scale L_D and root mean square fluctuation n_{rms} of the disorder-induced carrier density inhomogeneities. Using the Boltzmann theory we obtain the relation between the mean free path and the doping, $\ell(n) = v_F \tau(n)$, valid in the homogeneous limit. In the limit

in which $\ell(n_{\mathrm{rms}}) \ll L_D$ the number of scattering events inside a single homogeneous region, puddle, of the inhomogeneous landscape is large enough that the Boltzmann theory is valid locally. In addition, due to Klein tunneling, as in graphene [28, 29, 30, 31, 32, 33, 34], the resistance due to the boundaries between the puddles can be neglected in comparison to the resistance arising from scattering events inside the puddles [24]. Under these conditions, due to the random distribution of the puddles, graphene transport can be described by the effective medium theory (EMT) [35, 36, 37, 24, 38, 1]. In the EMT, which is extensively used in science and engineering to quantitatively describe properties of highly inhomogeneous systems, the conductivity of the inhomogeneous system is obtained as the conductivity σ_{EMT} of an equivalent homogeneous effective medium by averaging over disorder realizations the local values $\sigma(n(\mathbf{r}))$ given by the Boltzmann theory. The resulting implicit equation for σ_{EMT} is:

$$\int dn \frac{\sigma(n) - \sigma_{EMT}}{\sigma(n) + \sigma_{EMT}} P[n] = 0 \qquad (1.11)$$

where $P[n]$ is the disorder-averaged carrier density probability distribution that we obtain using the TFDT. This integral equation is derived by using the fact that the spatial average of the electric field fluctuations is zero. A solution of the implicit EMT integral equation defined by Eq. 1.11 provides the effective conductivity of the inhomogeneous system. In graphene the TFDT+EMT method has been shown to give results in remarkable agreement with experiments [1] even in the highly inhomogeneous situation very close to the Dirac point and with full quantum transport analysis [39, 34].

The TFD-EMT technique, described above, successfully explains the graphene transport properties in the theoretically difficult inhomogeneity-dominant regime near the charge neutral point, but this approach fails to explain the temperature dependence of the conductivity for a wide range of temperatures.

1.3 Outline of the thesis

In this thesis, we theoretically study in a comprehensive manner the temperature and carrier density dependence of graphene transport properties.

In Chapter 2, We calculate the graphene conductivity by taking into account the non-mean-field two-component nature of transport in the highly inhomogeneous density and potential landscape, where activated transport across the potential fluctuations in the puddle regimes coexists with regular metallic diffusive transport. The existence of puddles allows the local activation at low carrier densities, giving rise to an insulating temperature dependence in the conductivity of both monolayer and bilayer graphene systems. We also critically study the qualitative similarity and the quantitative difference between monolayer and bilayer graphene transport in the presence of puddles. Our theoretical calculation explains the non-monotonic feature of the temperature dependent transport, which is experimentally generically observed in low mobility graphene samples. We establish the 2-component nature (i.e., both activated and diffusive) of graphene transport arising from the existence of potential fluctuation induced inhomogeneous density puddles. The temperature dependence of the graphene conductivity arises from many competing mechanisms,

11

even without considering any phonon effects, such as thermal excitation of carriers from the valence band to the conduction band, temperature dependent screening, thermal activation across the potential fluctuations associated with the electron-hole puddles induced by the random charged impurities in the environment, leading to very complex temperature dependence which depends both on the carrier density and the temperature range of interest. The work in this chapter has led to the publication of Ref. [40].

In Chapter 3, we consider an intriguing "disorder by order" phenomenon in graphene transport where higher-quality (and thus more ordered) samples, while having higher mobility at high carrier density, will manifest more strongly insulating (and thus effectively more disordered) behavior as the carrier density is lowered compared with lower quality samples (with higher disorder) which exhibit an approximate resistivity saturation phenomenon at low carrier density near the Dirac point. This behavior simulating a metal-insulator transition, which we believe to have recently been observed in an experiment at Manchester University [41], arises from the suppression of Coulomb disorder induced inhomogeneous puddles near the charge neutrality point in high quality graphene samples. The work in this chapter has led to the publication of Ref. [42].

In Chapter 4, we study carrier transport through graphene on $SrTiO_3$ substrates by considering relative contributions of Coulomb and resonant impurity scattering to graphene resistivity. We establish that charged impurity scattering must dominate graphene transport as the charge neutrality point is approached by lowering the carrier density, and in the higher density regime away from the neutral-

ity point a dual model including both charged impurities and resonant defects gives an excellent description of graphene transport on SrTiO$_3$ substrates. We further establish that the non-universal high-density behavior of $\sigma(n)$ in different graphene samples on various substrates arises from the competition among different scattering mechanisms, and it is in principle entirely possible for graphene transport to be dominated by qualitatively different scattering mechanisms at high and low carrier densities. The work in this chapter has led to the publication of Ref. [43].

In Chapter 5, We study both monolayer and bilayer graphene transport properties taking into account the presence of correlations in the spatial distribution of charged impurities. In particular we find that the experimentally observed sublinear scaling of the graphene conductivity can be naturally explained as arising from impurity correlation effects in the Coulomb disorder. We find that also in bilayer graphene correlations among impurities induce a crossover of the scaling of the conductivity at higher carrier densities. We show that in the presence of correlation among charged impurities the conductivity depends nonlinearly on the impurity density n_i and can even increase with n_i. The work in this chapter has led to the publication of Ref. [44, 45].

In Chapter 6, we present our conclusions.

Chapter 2

Disorder-induced temperature-dependent transport in graphene: Puddles, impurities, activation, and diffusion

Much of the early work on graphene transport focused on the density-dependent (i.e., gate voltage tuned)[1, 7, 8, 9, 10, 13, 46] and temperature-dependent [1, 47, 48, 49, 50] conductivity in homogeneous MLG and BLG systems. The basic graphene transport properties, particularly at high densities far from the charge neutral Dirac point, are now reasonably well-understood[1].

However, unintended charged impurities, which are invariably present in the graphene environment, (e.g., the substrate-graphene interface), lead to the formation of inhomogeneous electron-hole puddles in the system [16, 24], which have been confirmed by experiments[19, 51, 52, 53] using the techniques of scanning potential and tunneling microscopies. Although MLG samples show a metallic behavior at high densities a weak "insulating" temperature-dependent conductivity $\sigma(T)$ has been measured at low carrier density and at the charge neutrality point (CNP) [47]. (We define insulating/metallic temperature dependence of conductivity $\sigma(T)$ as $d\sigma(T)/dT$ being positive/negative at fixed gate voltage.) In addition, a recent

experiment[21] on low mobility MLG grown by chemical vapor deposition (CVD) shows a strong "insulating" behavior at low temperatures and a metallic feature at high temperatures manifesting a non-monotonic temperature dependence in the measured electrical conductivity. Figs. 2.1(a) and (b) show the temperature dependence of resistivity with reference to $\rho(4.2K)$ at carrier densities near the charge neutrality point for device A and B, respectively [21]. The characteristic observed feature of carrier transport in low mobility sample A [Fig. 2.1(a)] is a strong insulating behavior at low temperatures ($T < 200$ K) for all densities (up to 7.2×10^{11} cm^{-2}). For carrier density larger than 2.9×10^{11} cm^{-2}) a nonmonotonicity in the temperature-dependent resistivity develops. The observed insulating behavior and nonmonotonicity at high density in low mobility samples is not observed in high mobility samples B [Fig. 2.1(b)], where the measured resistivity shows a metallic temperature dependence at higher densities even though the experimental conductivity manifests an insulating behavior at very low carrier density (up to 2.0×10^{11} cm^{-2}) [21]. The negative $d\rho/dT$ at the Dirac point is about 40% for both samples independent of sample mobility [21]. These observed effects are consistent with the predictions of our theory developed in this chapter.

In BLG samples [54, 12, 55, 56] the strong insulating behavior in the temperature dependent conductivity has been observed not only near CNP but also at carrier densities as high as 10^{12}cm^{-2} or higher. To be more specific, in Ref. [54], $\sigma(T)$ in BLG increases by $20 - 40\%$ as temperature T increases from $4 - 300$ K for carrier density in the range $3.19 \times 10^{12} - 7.16 \times 10^{12}$ cm^{-2}. Fig. 2.2 presents the temperature dependence of the hole mobility at various carrier densities for bi-
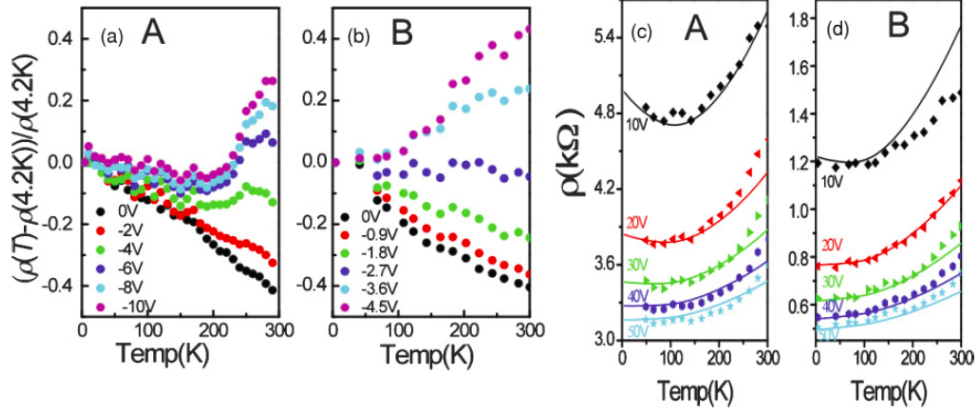
Figure 2.1: Transport measurement in monolayer graphene. (a) and (b) Resistivity at different gate voltages near the charge neutrality point. (a) device A, (b) device B;(c) and (d) Resistivity at higher gate voltages. (c) device A, (d) device B. Adapted from Figs. 2 and 3 of Ref. [21].

layer graphene devices, where the mobility increases with temperature. Fig. 2.2 also shows that the minimum conductance increases dramatically as the temperature increases.

To understand this anomalous temperature dependence in $\sigma(T)$, both MLG and BLG, it is essential to know the role of disorder in graphene transport. We note that phonon scattering (Ref. [57, 58]), although being weak in graphene, always contributes an increasing resistivity with increasing temperature and thus always leads to metallic behavior, and thus cannot be the mechanism for the intriguing insulating temperature dependence often observed in graphene transport at lower carrier densities – in fact, at very high temperatures (> 300 K) graphene should always manifest metallic temperature dependence in its conductivity due to phonon scattering effects which we ignore. Our goal in this chapter is to theoretically study in a comprehensive manner the temperature dependence of graphene transport properties arising entirely from the disorder effects.

16
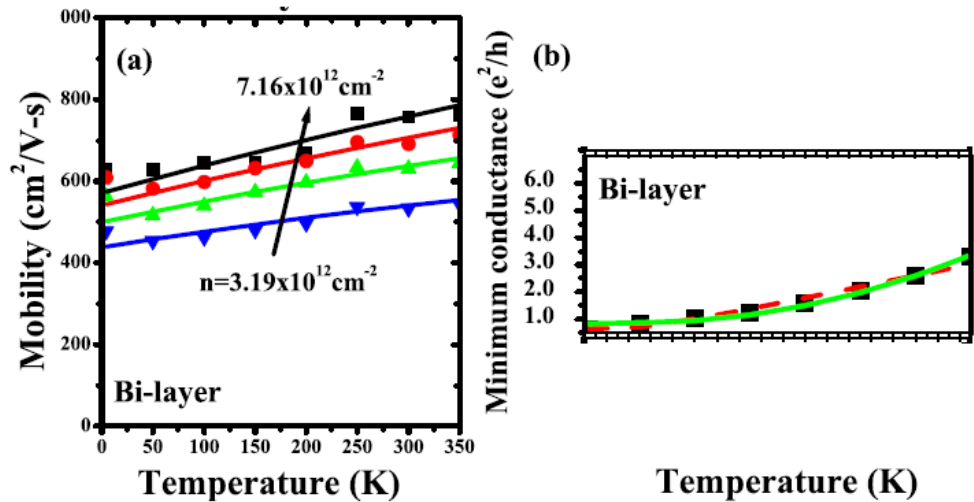
Figure 2.2: Transport measurement in bilayer graphene. (a) Hall mobility for holes as a function of temperature at various carrier densities; (b) Minimum conductance as a function of temperature. Adapted from Figs. 2 and 6 of Ref. [54].

In this chapter, we apply an analytic statistical theory to MLG systems and explain the intriguing coexistence of both metallic and insulating features of MLG $\sigma(T)$. In the presence of large fluctuating potentials $V(\mathbf{r})$ associated with microscopic configurations of Coulomb disorder in the system, the local Fermi level, $\mu(\mathbf{r}) = E_F - V(\mathbf{r})$, would necessarily have large spatial fluctuations. We carry out an analytical theory implementing this physical idea by assuming that the value of the potential at any given point follows a Gaussian distribution, parametrized by $s = V_{rms}$ (the root-mean-square fluctuations or the standard deviation in $V(\mathbf{r})$ about the average potential). This distribution can then be used to average the local density of states to obtain effective carrier densities, which can then be used to compute the physical quantities of interest[59]. The observed anomalous temperature dependent $\sigma(T)$ is then understood as the competition between the thermal activation of carrier density and temperature-dependent screening effects. Our theory explains

17

the suppression of the insulating behavior in higher mobility samples with lower disorder, which is consistent with experimental observations. We also provide the similarity and the quantitative difference between monolayer and bilayer graphene transport in the presence of puddles.

The motivation of our theory comes from the observation that the electron-hole puddles, which dominate the low-density graphene landscape, allow for a 2-component semiclassical transport behavior, where the usual metallic diffusive carrier transport is accompanied by transport by activated carriers which have been locally thermally excited above the potential fluctuations imposed by the static disorder. This naturally allows for both insulating and metallic transport behavior occurring preferentially, respectively, at lower and higher carrier densities since the puddles disappear with increasing carrier density due to screening. At zero temperature (where no activation is allowed) or at very high carrier density (where puddles are suppressed), only diffusive transport is possible. But at any finite temperatures and at not too high densities, there would always be a 2-component transport with both activated and diffusive carriers contributing to conductivity. Our theory develops this idea into a concrete description. We emphasize that our theory explicitly takes into account the inhomogeneous nature of the graphene landscape and is non-mean-field as a matter of principle.

We first introduce the analytical statistical theory to describe random electronic potential fluctuations created by charged impurities in the environment. We also calculate the modified density of states and the corresponding temperature-dependent effective carrier density in monolayer graphene. Then, we describe the

18

calculations and the main features of the temperature-dependent conductivity of MLG in the presence of density inhomogeneity. We elaborate and extend our earlier results for the interplay between density inhomogeneity and temperature in bilayer graphene (BLG) transport. We further discuss the connection of our theory to earlier theories. We discuss the similarities and quantitative differences among the effects of inhomogeneity (i.e., the puddles) on MLG and BLG transport and summarize our results. In Appendix A, we discuss a microscopic theory to calculate the effects of potential fluctuation on graphene systems, providing a self-consistent formulation of graphene density of states in the presence of random charged impurities near graphene/substrate interface, showing in the process that this microscopically calculated density of states agrees well with the model density of states obtained from the Gaussian fluctuations.

2.1 Temperature dependent carrier density for inhomogeneous MLG

It is well known that MLG breaks up into an inhomogeneous landscape of electron-hole puddles, especially around the charge neutral point (CNP) [19, 22, 51, 52, 53]. Below we derive an analytic statistical theory taking account of the effects of inhomogeneous density in monolayer graphene (MLG) to explain the nonmonotonic temperature dependent transport observed in MLG [47, 21]. We start by assuming that charged impurities, located in the substrate or near the graphene, create a local electrostatic potential, which fluctuates randomly about its average value across the

surface of the graphene sheet. The potential fluctuations themselves are assumed to be described by a statistical distribution function $P(V)$ where $V = V(\mathbf{r})$ is the fluctuating potential energy at the point $\mathbf{r} \equiv (x, y)$ in the 2D MLG plane. We approximate the probability $P(V)dV$ of finding the local electronic potential energy within a range dV about V to be a Gaussian form, i.e.,

$$P(V) = \frac{1}{\sqrt{2\pi s^2}} \exp(-V^2/2s^2), \tag{2.1}$$

where s is the standard deviation (or equivalently, the strength of the potential fluctuation), which is used as an adjustable parameter to tune the tail-width[60]. In the Appendix, we provide a microscopic approach to self-consistently solve the strength of potential fluctuations in the presence of charged impurities. Due to the electron-hole symmetry in the problem, we only provide the formalism and equations for electron like carriers and the hole part can be obtained simply by changing E to $-E$.

The potential fluctuations given by Eq. (2.1) affect the overall electronic density of states (DOS) in MLG. In our model we do not assume that the size of the puddles to be identical, but we take the puddle sizes to be completely random controlled by the distribution function given in Eq. 2.1. We emphasize that our assumption of a Gaussian distribution for the potential fluctuations, equivalently implying a Gaussian distribution for the density fluctuations associated with the puddles, is known to be an excellent quantitative approximation to the actual numerically calculated puddle structures in graphene[1, 22]. The characteristics of the puddles are determined by both the sign and the magnitude of $V - E_F$, i.e., a neg-

ative (positive) $V - E_F$ indicates an electron (hole) region. A different approach utilizing equal size puddles with a certain potential V has been used to calculate transport coefficients using a numerical transfer matrix technique [61, 62, 63]. Then in the presence of electron-hole puddles the density of states is increased by the allowed electron region fraction and given by [64, 65, 60]

$$
\begin{aligned}
D_e(E) &= \int_{-\infty}^{E} \frac{g_s g_v (E - V)}{2\pi(\hbar v_F)^2} P(V) dV \\
&= D_1 \Big[\frac{E}{2} \text{erfc}(-\frac{E}{\sqrt{2}s}) + \frac{s}{\sqrt{2\pi}} \exp(-\frac{E^2}{2s^2}) \Big],
\end{aligned}
\tag{2.2}
$$

where $\text{erfc}(x)$ is the complementary error function,

$$
\text{erfc}(x) = \frac{2}{\sqrt{\pi}} \int_{x}^{\infty} e^{-t^2} dt,
\tag{2.3}
$$

and $D_1 = \dfrac{g_s g_v}{2\pi(\hbar v_F)^2}$, where v_F is the graphene Fermi velocity, $g_s = 2$ and $g_v = 2$ are the spin and valley degeneracies, respectively. We have $D_1 = 1.5 \times 10^8$ cm^{-2}/meV^2 with the Fermi velocity $v_F = 10^6$ m/s. Note that the tail of the DOS is determined by the potential fluctuation strength s. For the case $s = 0$, the system becomes homogeneous and $D_e(E) = D_1 E$. In this case there is no carrier density at Dirac point $(E = 0)$ at zero temperature. It is apparent that in the presence of potential fluctuations, the $D_e(E)$ starts at finite value $\frac{D_1 s}{\sqrt{2\pi}}$ at $E = 0$ and approaches $D_1 E$ in high energy limit. For high-energy limit, the carrier is essentially free since nearly every point of the system is accessible. In Fig. 2.3, we show the normalized density of states as a function of energy for both electrons and holes in MLG. We mention that the self-consistent microscopic theory gives the same structure for the density of states of graphene systems (see Appendix A).

Since monolayer graphene is a semi-metal or zero-gap semiconductor, the elec-

21
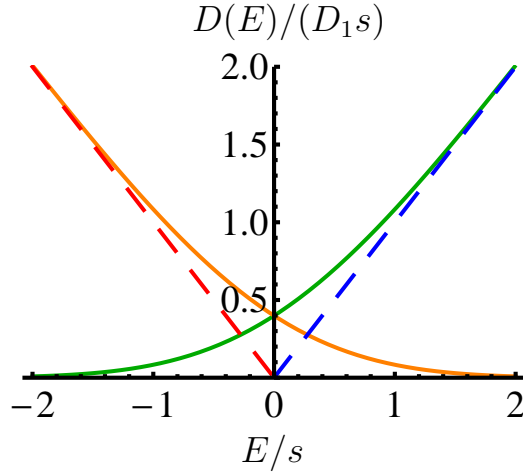
Figure 2.3: Normalized density of states for both electron and hole in MLG. The solid and dashed lines are for the DOS in inhomogeneous and homogeneous systems, respectively. The electron (hole) band tail locates at $E < 0$ ($E > 0$), which gives rise to electron (hole) puddles at $E < 0$ and $E > 0$.

tron density at finite temperatures increases due to the direct thermal excitation from valence band to conduction band, which is one of the important sources of temperature dependent transport at low carrier densities. Therefore, we first consider the temperature dependence of thermally excited electron density. The total electron density is given by

$$n_e = \int_{-\infty}^{\infty} D_e(E) \frac{dE}{e^{\beta(E-\mu)} + 1}, \qquad (2.4)$$

where $\beta = 1/k_B T$ and μ is the chemical potential. At $T = 0$, μ becomes the Fermi energy $\mu(T = 0) = E_F$.

2.1.1 $n_e(T)$ of MLG at CNP ($E_F = 0$)

When the Fermi energy is zero (or at CNP) all electrons are located in the band tail at $T = 0$ and the electron and hole densities in the band tail are given by

$$n_0 = n_e(E_F = 0) = n_h(E_F = 0) = D_1 \frac{s^2}{4}. \qquad (2.5)$$

22

Note that the electron (or hole) density in the band tails increases quadratically with the standard deviation s. At finite temperatures the behavior of $n_e(T)$ at CNP becomes

$$n_e(T) = n_0 \left[1 + \frac{\pi^2}{3} \left(\frac{k_B T}{s} \right)^2 \right]. \tag{2.6}$$

The leading order temperature dependence in $n_e(T)$ is quadratic. For homogeneous MLG ($s = 0$) with the linear-in-energy behavior of the DOS, the electron density is given by $n_e(T) = \frac{D_1 \pi^2}{12} k_B^2 T^2$. In particular, in the ballistic regime the number of propagating channels increases due to the thermal smearing of the Fermi surface, which leads to the observation of an insulating behavior in $\sigma(T)$ at CNP for high mobility suspended graphene samples[66, 67, 68]. The presence of the band tail does not change the quadratic temperature dependence in the thermal excitation when the system is at the charge neutral point ($E_F = 0$). But the inhomogeneous MLG has n_0 electrons in the band tails. In Fig. 2.4(a) we show the temperature dependent electron density at CNP for different values of standard deviation s.
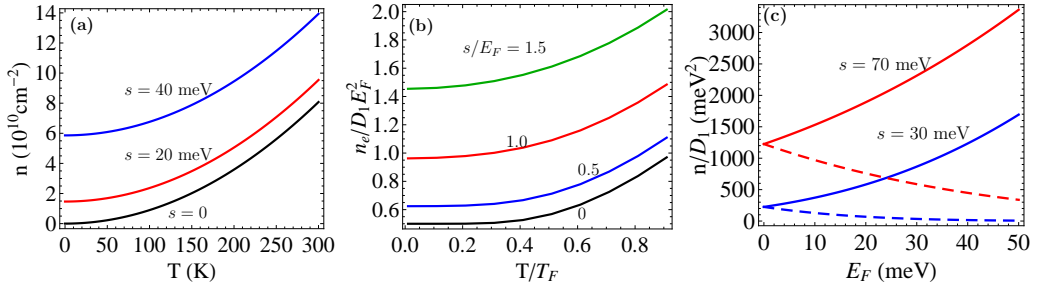
Figure 2.4: (a) The electron density of MLG at CNP as a function of temperature for different s. At $T = 0$ the density is given by $n_0 = D_1 s^2/4$. (b) The temperature dependent electron density of MLG at finite E_F for different s. For $s/E_F \neq 0$ the leading order behavior is quadratic. (c) Total electron densities (solid lines) and hole densities (dashed lines) of MLG as a function of E_F for two different $s = 30$ meV and 70 meV. The densities at the band tails are given by $n_e(E_F = 0) = n_h(E_F = 0) = D_1 s^2/4$.

2.1.2 $n_e(T)$ of MLG at finite doping $(E_F > 0)$

In the case of finite doping (or gate voltage), i.e., $E_F \neq 0$, the electron density

of the homogeneous MLG (i.e., $s = 0$) is given by

$$
\begin{aligned}
n_{0e}(T) &= D_1 \int_0^\infty \frac{E dE}{\exp(\beta(E - \mu_0)) + 1} \\
&= -D_1 \frac{F_1(\mu_0 \beta)}{\beta^2}
\end{aligned}
\tag{2.7}
$$

where $F_1(x) = \int_0^\infty \frac{t\, dt}{1 + \exp(t - x)}$, and μ_0 is the chemical potential of homogeneous

MLG and is determined by the conservation of the total electron density. Then the

chemical potential is given by the following relation, $\dfrac{E_F^2 \beta^2}{2} = F_1(\beta \mu_0) - F_1(-\beta \mu_0)$.

Using the asymptotic forms [49] of the function $F_1(x)$ for $x \ll 1$ and $x \gg 1$, i.e.,

$$
F_1(x) \approx \frac{\pi^2}{12} + x\ln 2 + \frac{x^2}{4} \quad \text{for} \quad |x| \ll 1
\tag{2.8}
$$

$$
F_1(x) \approx \left[\frac{x^2}{2} + \frac{\pi^2}{6} \right] \theta(x) + x\ln(1 + e^{-|x|}) \text{ for } |x| \gg 1,
$$

we have the asymptotic formula for the chemical potential in both low- and high-

temperature limits for homogeneous MLG

$$
\mu_0(T) \simeq E_F \left[1 - \frac{\pi^2}{6} \left(\frac{T}{T_F} \right)^2 \right] \quad \text{for} \quad T \ll T_F
\tag{2.9}
$$

$$
\mu_0(T) \simeq \frac{E_F}{4\ln 2} \frac{T_F}{T} \quad \text{for} \quad T \gg T_F.
$$

Then the corresponding asymptotic formula of the electron density (Eq. 2.7) are

given by

$$
n_{0e}(T) \simeq \frac{D_1 E_F^2}{2} \left(1 + \frac{\pi^4}{36} \frac{T^4}{T_F^4} \right) \quad \text{for} \quad T \ll T_F
\tag{2.10}
$$

$$
n_{0e}(T) \simeq \frac{D_1 E_F^2 \pi^2}{12} \frac{T^2}{T_F^2} \quad \text{for} \quad T \gg T_F
$$

Since the direct thermal excitation is suppressed due to the finite Fermi energy, the excited electron density at low temperatures $(T \ll T_F)$ increases quartically rather than quadratically. But at high temperatures $(T \gg T_F)$, the total electron density becomes a quadratic function of temperature as shown for an undoped MLG.

Next, we derive the temperature dependence of thermally excited electron density in the presence of electron-hole puddles $(s \neq 0)$ at finite doping $(E_F \neq 0)$. At zero temperature the electron density for the inhomogeneous MLG can be written as:

$$n_e(0) = \frac{D_1 E_F^2}{4} \left[(1 + \tilde{s}^2)\mathrm{erfc}(-\frac{1}{\sqrt{2}\tilde{s}}) + \sqrt{\frac{2}{\pi}}\tilde{s}\exp(-\frac{1}{2\tilde{s}^2}) \right]$$

(2.11)

$$n_h(0) = \frac{D_1 E_F^2}{4} \left[(1 + \tilde{s}^2)\mathrm{erfc}(\frac{1}{\sqrt{2}\tilde{s}}) - \sqrt{\frac{2}{\pi}}\tilde{s}\exp(-\frac{1}{2\tilde{s}^2}) \right]$$

where $\tilde{s} = s/E_F$. The presence of electron-hole puddles does not induce any additional charge in the MLG system, so that the net carrier density $n = n_e - n_h$ should be conserved. Then, the finite temperature chemical potential $\mu(T)$ changes as a function of both temperature and the strength of potential fluctuation s, and it should satisfy the following relation:

$$\int_{-\infty}^{E_F} D_e(E)dE \; - \int_{E_F}^{\infty} D_h(E)dE$$

(2.12)

$$= \int_{-\infty}^{\infty} \frac{D_e(E)dE}{1 + \exp(\beta(E - \mu))} - \int_{-\infty}^{\infty} \frac{D_h(E)dE}{1 + \exp(\beta(\mu - E))},$$

where $D_e(E)$ is the electronic density of states given by Eq. 2.2 and $D_h(E) = D_e(-E)$ is the density of states for holes. The asymptotic analytical formula of the

chemical potential $\mu(T)$ for inhomogeneous MLG is obtained as:

$$\mu(T) \simeq E_F\left[1 - \frac{\pi^2}{6}(\frac{T}{T_F})^2 A(\tilde{s})\right] \quad \text{for} \ \ T \ll T_F$$

(2.13)

$$\mu(T) \simeq E_F B(\tilde{s}, t) \quad \text{for} \quad T \gg T_F$$

where functions $A(\tilde{s})$ and $B(\tilde{s})$ are given as follows:

$$A(\tilde{s}) = e^{\frac{1}{2\tilde{s}^2}}\text{erf}\left[\frac{1}{\sqrt{2}\tilde{s}}\right] \Big/ \left(\sqrt{\frac{2}{\pi}}\tilde{s} + e^{\frac{1}{2\tilde{s}^2}}\text{erf}\left[\frac{1}{\sqrt{2}\tilde{s}}\right]\right)$$

(2.14)

$$B(\tilde{s}, t) = \left(\frac{e^{-\frac{1}{2\tilde{s}^2}}\tilde{s}}{\sqrt{2\pi}} + \frac{1}{2}(\tilde{s}^2 + 1)\text{erf}\left[\frac{1}{\sqrt{2}\tilde{s}}\right]\right) \Big/ \left(2\ln 2 \ t + \frac{\tilde{s}^2}{4t}\right)$$

where $t = T/T_F$ and $\text{erf}(x) = \frac{2}{\sqrt{\pi}}\int_0^x e^{-t^2}dt$ is the error function.

Combining Eqs. 2.2, 2.4 and 2.13, we obtain the asymptotic analytical formula of the electron density for inhomogeneous MLG at low- and high-temperature limits as:

$$n_e(T) \simeq n_e(0) + D_1 E_F^2 \frac{\pi^2}{12}\frac{T^2}{T_F^2}(1 - A(\tilde{s})) \quad \text{for} \ \ T \ll T_F$$

(2.15)

$$n_e(T) \simeq n_{0e}(T) + n_e(0) - \frac{D_1 E_F^2}{4} \quad \text{for} \quad T \gg T_F$$

In the low temperature limit ($T \ll T_F$), the leading order term for the electron density has the same quadratic behavior as in undoped homogeneous MLG ($E_F = 0$), but the coefficient is strongly suppressed by fluctuation for the case of $s < E_F$, i.e., the high carrier density sample. While in the case of $s > E_F$, i.e., the low carrier density sample, the existence of electron-hole puddles gives rise to a notable quadratic behavior for electron density $n_e(T)$ [see Fig. 2.4(b)].

26

2.2 Conductivity of inhomogeneous MLG

In this section, we calculate the finite temperature conductivity for inhomogeneous MLG with the temperature-dependent effective carrier density derived above. The existence of electron-hole puddles allows the current to flow through "percolation channels", and the transport properties of the inhomogeneous MLG system can be derived using the self-consistent effective medium theory of conductance in composite mixtures[69], where the number of electrons per puddle is not an important issue for our theory. The percolation assumption is valid as long as the potential fluctuation is larger than the thermal energy of the carriers. Otherwise transport due to disorder scattering dominates. We emphasize that in our formalism the crossover from the percolation transport to ordinary scattering-dominated diffusive transport is guaranteed as the temperature is increased since we are explicitly taking into account both diffusive transport of free carriers and activated transport of the classically-localized carriers in our theory. The only effects we neglect are quantum tunneling through the potential barriers and quantum interference since ours is a semiclassical theory. We also do not consider Klein tunneling explicitly because the Klein tunneling occurs at zero temperature for normal incident carriers at the electron-hole puddle boundary. We also apply the Boltzmann transport theory, where we include the scattering mechanism with screened Coulomb impurities and short-range disorder[49]. Note that the application of Boltzmann transport theory is justifiable because quantum interference effects are not experimentally observed in the temperature regime of interest to us. It is conceivable that quantum

27

interference and localization play some roles in graphene transport at very low temperatures. We also neglect all phonon effects since electron-phonon coupling is weak in graphene. Phonon effects are relevant at high temperatures (> 100 K) and have been considered in the literature[57, 58].

At CNP ($E_F = 0$) electrons and holes are equally occupied. As the Fermi energy increases, more electrons occupy increasingly larger proportion of space. As the Fermi energy increases to $E_F \gg s$, nearly all space is populated by the electrons [see Fig. 2.4(c)] and the conductivity of the system approaches the characteristic of the homogeneous material. Thus, there is a possible coexistence of metallic and thermally-activated transport in the presence of electron-hole puddles. When electron puddles occupy more space than hole puddles, most electrons follow the continuous metallic paths extended throughout the system, but it is possible at finite temperatures that the thermally activated transport of electrons persists above the hole puddles. On the other hand, holes in hole puddles propagate freely, but when they meet electron puddles, activated holes conduct over the electron puddles. Carrier transport in each puddle is characterized by propagation of weak scattering transport theory[69]. The activated carrier transport of prohibited regions, where the local potential energy V is less (greater) than Fermi energy for electrons (holes), is proportional to the Fermi factor. If σ_e and σ_h are the average conductivity of electron and hole puddles, respectively, then the activated conductivities are given

by

$$\sigma_e^{(a)}(V) = \sigma_e \exp[\beta(E_F - V)], \tag{2.16a}$$

$$\sigma_h^{(a)}(V) = \sigma_h \exp[\beta(V - E_F)], \tag{2.16b}$$

where the density and temperature dependent average conductivities (σ_e and σ_h) are given within the Boltzmann transport theory [1] by $\sigma_e \propto n_e \langle \tau \rangle$ and $\sigma_h \propto n_h \langle \tau \rangle$, where n_e and n_h are average electron and hole densities, respectively, and $\langle \tau \rangle$ is the average transport relaxation time which includes the thermal smearing effects and depends explicitly on the scattering mechanism [1] and it is given by,

$$\langle \tau \rangle = E_F \frac{\int d\epsilon D_e(\epsilon) \tau(\epsilon)(-\partial f/\partial \epsilon)}{\int d\epsilon D_e(\epsilon) f(\epsilon)} \tag{2.17}$$

where $\tau(\epsilon)$ and $f = 1/(1 + e^{\beta(\epsilon - \mu)})$ are, respectively, the energy-dependent transport scattering time and the finite temperature Fermi distribution function. Because the density inhomogeneity effects already been considered in the variation of effective carrier density, we use the DOS of homogeneous MLG $D_e(\epsilon) = D_1 \epsilon$ in Eq. 2.17 to avoid double counting. $\tau(\epsilon)$ is given by Eq. 5.10.

Now we denote the electron (hole) puddle as region '1' ('2'). In region 1 electrons occupy more space than holes when $E_F > 0$. The fraction of the total area occupied by electrons with Fermi energy E_F is given by $p = \int_{-\infty}^{E_F} P(V)dV$. Then the total conductivity of region 1 can be calculated,

$$\begin{aligned}
\sigma_1 &= \frac{1}{p} \int_{-\infty}^{E_F} (\sigma_e + \sigma_h^{(a)}) P(V) dV, \\
&= \sigma_e + \frac{\sigma_h}{2p} e^{\frac{\beta^2 s^2}{2} - \beta E_F} \mathrm{erfc}\left(-\frac{E_F}{\sqrt{2}s} + \frac{\beta s}{\sqrt{2}}\right).
\end{aligned} \tag{2.18}$$

At the same time the holes occupy the area with a fraction $q = 1 - p$ and the total conductivity of region 2 becomes

$$
\begin{aligned}
\sigma_2 &= \frac{1}{q} \int_{E_F}^{\infty} (\sigma_e^{(a)} + \sigma_h) P(V) dV \\
&= \sigma_h + \frac{\sigma_e}{2q} e^{\frac{\beta^2 s^2}{2} + \beta E_F} \mathrm{erfc}\left(\frac{E_F}{\sqrt{2}s} + \frac{\beta s}{\sqrt{2}} \right).
\end{aligned}
\tag{2.19}
$$

The σ_1 and σ_2 are distributed according to the binary distribution. The conductivity of binary system can be calculated by using the effective medium theory of conductance in mixtures[69]. The result for a 2D binary mixture of components with conductivity σ_1 and σ_2 is given by [69]

$$
\sigma_t = \left(p - \frac{1}{2}\right) \left[(\sigma_1 - \sigma_2) + \sqrt{(\sigma_1 - \sigma_2)^2 + \frac{4\sigma_1 \sigma_2}{(2p-1)^2}} \right].
\tag{2.20}
$$

This result can be applied for all Fermi energy. For a large doping case, in which the hole puddles disappear, we have $p = 1$ and $\sigma_2 = 0$, then Eq. (2.20) becomes $\sigma = \sigma_1$, i.e., the conductivity of electrons in the homogeneous system.
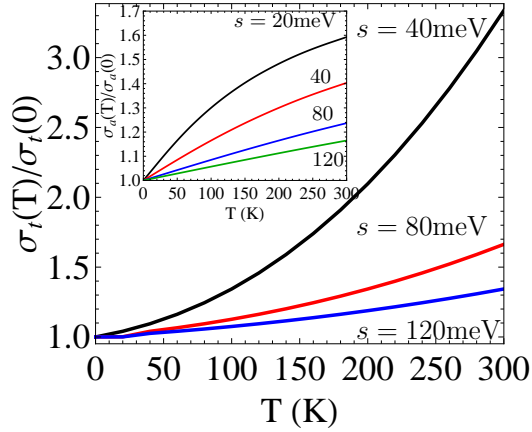
Figure 2.5: $\sigma_t(T)$ of MLG at charge neutral point for different s (Eq. 2.21a and n_e as given in Eq. 2.6). Inset shows the thermally activated conductivity of MLG as a function of temperature, where $\sigma_a(T)/\sigma_a(0) = 1 + e^{\beta^2 s^2 / 2} \mathrm{erfc}(\beta s / \sqrt{2})$.

2.2.1 $\sigma(T)$ of MLG at CNP ($E_F = 0$)

We first consider the conductivity at CNP ($E_F = 0$). The conductivities in each region are given by

$$\sigma_1 = \sigma_e \left[1 + \frac{\eta}{2p} e^{\beta^2 s^2/2} \text{erfc}(\beta s/\sqrt{2})\right], \tag{2.21a}$$

$$\sigma_2 = \sigma_h \left[1 + \frac{1}{2q\eta} e^{\beta^2 s^2/2} \text{erfc}(\beta s/\sqrt{2})\right], \tag{2.21b}$$

where $\eta = n_h/n_e$ is the ratio of the hole density to the electron density. Since the electrons and holes are equally populated, we have $p = q = 1/2$ and $\sigma_e = \sigma_h$, then the total conductivity becomes $\sigma_t = \sqrt{\sigma_1 \sigma_2} = \sigma_1$. The asymptotic behavior of the conductivity at low temperatures ($k_B T \ll s$) becomes

$$\sigma_t(T) = \sigma_e \left[1 + \sqrt{\frac{2}{\pi}} \frac{k_B T}{s} - \frac{2}{\sqrt{\pi}} \frac{(k_B T)^3}{s^3}\right]. \tag{2.22}$$

The activated conductivity increases linearly with a slope $\sqrt{2/\pi} k_B/s$ as temperature increases. Typically s is smaller in higher mobility samples, which gives rise to stronger insulating behavior at low temperatures. The next order temperature correction to conductivity arises from the thermal excitation given in Eq. (2.6) which gives quadratic (T^2) temperature corrections. Thus, in the low temperature limit the total conductivity at the CNP is given by:

$$\sigma_t = \sigma(0) \left[1 + \sqrt{\frac{2}{\pi}} \frac{k_B T}{s} + \frac{\pi^2}{3} \left(\frac{k_B T}{s}\right)^2\right]. \tag{2.23}$$

At high temperatures ($k_B T \gg s$) we have

$$\sigma_t = \sigma_e \left[2 - \sqrt{\frac{2}{\pi}} \frac{s}{k_B T} + \frac{s^2}{2(k_B T)^2}\right]. \tag{2.24}$$

where the temperature dependence of σ_e has been given in Eq. (2.6). The total conductivity due to the activation behavior approaches a limiting value and all temperature dependence comes from the thermal excitation through the change of the effective carrier density in the presence of the inhomogeneity given in Eq. (2.6). Thus at very high temperatures $(T \gg s/k_B)$ the MLG conductivity at the charge neutral point increases quadratically regardless of the sample quality. In Fig. 2.5 the temperature dependent conductivity has been calculated at the charge neutral point, where the temperature dependent scattering mechanism can be neglected. In Ref. [21], about 60% increase of conductivity is observed as the temperature increases from 4 K to 300 K. We estimate the potential fluctuation parameter $s \sim 80$ meV for this sample based on our theoretical analysis as compared with the data.

2.2.2 $\sigma(T)$ of MLG at finite doping $(E_F > 0)$

At finite doping $(E_F > 0)$ the temperature dependent conductivities are very complex because three energies $(E_F, s, \text{ and } k_B T)$ are competing among them. Especially when $k_B T \ll s$, regardless of E_F, we have the asymptotic behavior of conductivities in region 1 and 2 from Eqs. (5.1) and (2.19), respectively,

$$\sigma_1 = \sigma_e \left[1 + \frac{\eta}{2p} e^{-1/2\tilde{s}^2} \sqrt{\frac{2}{\pi}} \frac{1}{\tilde{s}/t - 1/\tilde{s}} \right], \qquad (2.25a)$$

$$\sigma_2 = \sigma_h \left[1 + \frac{1}{2q\eta} e^{-1/2\tilde{s}^2} \sqrt{\frac{2}{\pi}} \frac{1}{\tilde{s}/t + 1/\tilde{s}} \right], \qquad (2.25b)$$

where $\tilde{s} = s/E_F$ and $t = T/T_F$. The leading order correction is linear but the coefficient is exponentially suppressed by the term $\exp(-E_F^2/2s^2)$. This fact indicates that in the high mobility sample with small s, the activated conductivity is weakly

32

temperature dependent except at low density regimes, i.e. $E_F < s$. Since the density increase by thermal excitation is also suppressed exponentially by the same factor [see Eq. (2.15)], the dominant temperature dependent conductivity arises from the scattering time [1], which manifests metallic behavior. On the other hand, for a low mobility sample with a large s, the linear temperature dependence due to thermal activation can be observed even at high carrier densities $E_F \gtrsim s$.
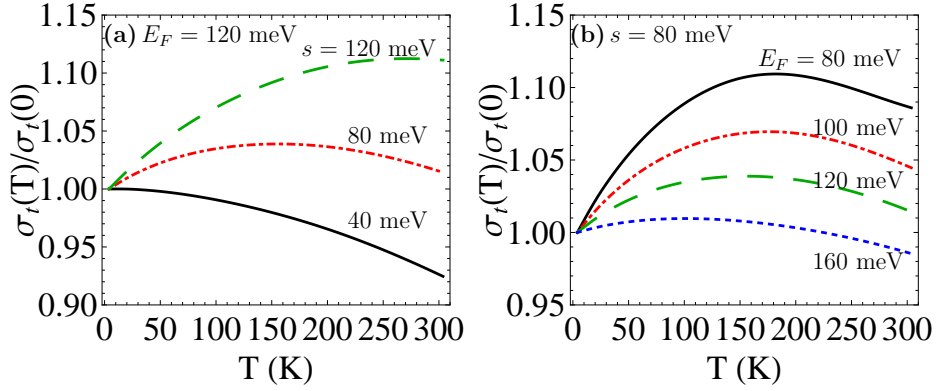
Figure 2.6: Calculated total conductivity $\sigma_t(T)/\sigma_t(0)$ of MLG with the following parameters: $n_i = 10^{12}$ cm^{-2} and $n_d V_0^2 = 2$ (eV Å)^2. (a) $\sigma_t(T)$ for $E_F = 120$ meV and for different s. (b) $\sigma_t(T)$ of MLG for $s = 80$ meV and for several $E_F = 80, 100,$ 120, 160 meV, which correspond to the net carrier densities $n = n_e - n_h \simeq 0.9 \times 10^{12}$, 1.2×10^{12}, 1.5×10^{12}, and 2.3×10^{12} cm^{-2}.

In Fig. 2.6 we present the total conductivities of inhomogeneous MLG as a function of temperature (a) for a fixed Fermi energy and several s and (b) for a fixed s and several Fermi energies. The calculations for Fig. 2.6 are all carried out for MLG on SiO$_2$ substrate (corresponding to dielectric constant $\kappa \approx 2.5$), charged impurity density $n_i = 10^{12}$ cm^{-2} and short-ranged disorder strength $n_d V_0^2 = 2$ (eV Å)^2. For total conductivity, the thermally activated insulting behavior competes with the temperature-dependent screening effects, where the latter always give the metallic behavior in conductivity for MLG samples. When s is small, the activated behavior

is suppressed and the total conductivity shows metallic behavior. While for large

value of s, i.e., low mobility samples, the thermal activation overwhelms the metallic

temperature dependence and the system manifests insulating behavior. For $s \sim E_F$

the situation becomes much complex. At low temperatures, the leading order of

the temperature dependence is linear (the second term in Eq. (2.25)) and the total

conductivity starts at weakly insulating behavior. As the temperature increases,

screening effects begin to dominant, leading to metallic behavior. As a result, the

temperature evolution of the conductivity becomes non-monotonic and for large s

(or low mobility samples) the nonmonotonic behavior can be more pronounced as

shown in experiments [21]. Note that electron-phonon will always lead to a metallic

temperature dependence with conductivity decreasing with temperature. At high

enough temperature $T > 200$ K, phonons will eventually dominate, and all graphene

samples should eventually exhibit metallic transport properties.

2.3 Temperature dependent carrier density of inhomogeneous BLG

In the following of this chapter, we extend our previous study[70] on insulating behavior in metallic bilayer graphene and compare it with the MLG situation.

The most important difference between MLG and BLG comes from the fact that,

in BLG, the two layers are weakly coupled by interlayer tunneling, leading to an

approximately parabolic band dispersion with an effective mass about $m \simeq 0.033 m_e$

(m_e corresponds to the bare electron mass) in contrast to linear-dispersion Dirac

carrier system for MLG. As done for MLG, we assume the electronic potential fluctuations in BLG system to be a Gaussian form given in Eq. 2.1 and this potential is felt equally by both layers[59].
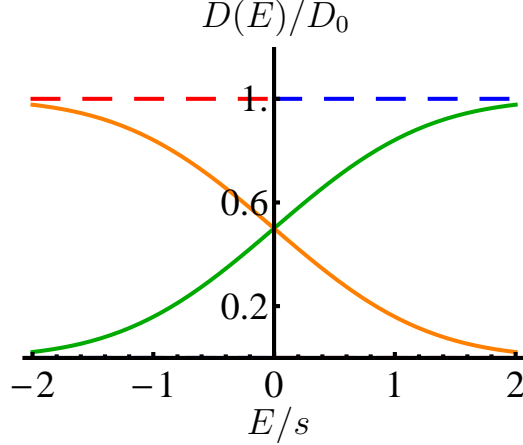
Figure 2.7: Normalized density of states for both electron and hole in BLG. The solid and dashed lines are for the DOS in inhomogeneous and homogeneous systems, respectively. The electron (hole) band tail locates at $E < 0$ ($E > 0$), which gives rise to electron (hole) puddles at $E < 0$ and $E > 0$.

In the presence of potential fluctuations the density of states (DOS) for disordered BLG is given by $D_e(E) = \int_{-\infty}^{E} D_0 P(V) dV = D_0 \text{erfc}(-E/\sqrt{2}s)/2$, where $D_0 = g_s g_v m/(2\pi\hbar^2)$ is the DOS in a homogeneous BLG system, where $g_s = 2$ and $g_v = 2$ are the spin and valley degeneracies, respectively. We have $D_0 = 2.8 \times 10^{10}$ cm^{-2}/meV assuming $m = 0.033 m_e$. The DOS of holes can be calculated from the following relation: $D_h(E) = D_e(-E)$. In Fig. 2.7, the density of states of both electron and hole are shown for the inhomogeneous BLG system. In the presence of potential fluctuations, the electron and hole coexist for certain amount of regions near CNP and their DOS approach to the homogeneous case as the carrier energy further increases.

Because BLG is also a gapless semiconductor like MLG, the direct thermal

excitation from valence band to conduction band at finite temperatures composes an important source of temperature dependent transport in BLG. Thus, the temperature dependence of thermally excited electron density is first to be considered.

2.3.1 $n_e(T)$ of BLG at CNP ($E_F = 0$)

With the help of Eq. 2.4, we could get the total electron density for BLG in the presence of electron-hole puddles. We first consider the situation at CNP, where all electrons are located in the band tail at $T = 0$ and the electron density in the band tail is given by $n_0 = n_e(E_F = 0) = D_0 s/\sqrt{2\pi}$[59]. In contrast to the quadratic dependence of s in MLG, the electron density in the band tail for BLG is linearly proportional to the standard deviation s. Unlike MLG, which has the exact formula for $n_0(T)$ (i.e., Eq. (2.6)), we could only find the asymptotic behavior of $n_0(T)$ at finite temperatures for BLG. The low temperature ($k_B T/s \ll 1$) behavior of electron density at CNP becomes

$$n_e(T) = n_0 \left[1 + \frac{\pi^2}{6} \left(\frac{k_B T}{s} \right)^2 \right]. \tag{2.26}$$

Thus, the electron density increases quadratically in the low temperature limit. For homogeneous BLG with the constant DOS the electron density at finite temperatures is given by $n_e(T) = D_0 \ln(2) k_B T$, which has the universal slope $D_0 \ln(2) k_B$. The presence of the band tail suppresses the thermal excitation of electrons and gives rise to the quadratic behavior. However, in the high temperature limit, the density increases linearly with the same slope approaching to the homogeneous system, i.e.,

$$n(T) \sim D_0 \left[\ln(2) k_B T + \frac{1}{8} \frac{s^2}{(k_B T)^2} \right]. \tag{2.27}$$

36

In Fig. 2.8(a) we show the temperature dependent electron density at CNP for different standard deviations. Compared with the inset of Fig. 2.5, it is apparent that, even for the same strength of potential fluctuation s, the effects of thermal excitation of carrier density are much stronger in BLG than in MLG sample, which leads to more easily observed insulating behavior in BLG samples.
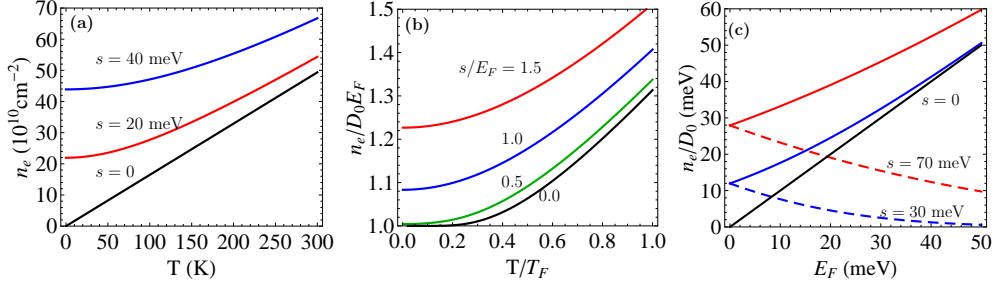
Figure 2.8: (a) The electron density of BLG at CNP as a function of temperature for different s. At $T = 0$ the density is given by $n_0 = D_0 s/\sqrt{2\pi}$. (b) The temperature dependent electron density of BLG at finite E_F for different s. For $s/E_F \neq 0$ the leading order behavior is quadratic while at $s = 0$ the density is exponentially suppressed. (c) Total electron densities (solid lines) and hole densities (dashed lines) of BLG as a function of E_F for two different $s = 30$ meV and 70 meV. The linear line represents the density difference $n = n_e - n_h = D_0 E_F$, which linearly depends on the Fermi energy. The densities at the band tails are given by $n_e(E_F = 0) = n_h(E_F = 0) = D_0 s/\sqrt{2\pi}$.

2.3.2 $n_e(T)$ of BLG at finite doping $(E_F > 0)$

In this subsection, we derived the total electron density at finite temperatures for inhomogeneous BLG away from CNP. Contrary to MLG, we need to calculate the finite temperature chemical potential (i.e., Eqs. 2.9 and 2.13). The charge conservation relation in both homogeneous and inhomogeneous BLG gives the temperature independent chemical potential $\mu \equiv E_F$, allowing us to directly calculate the total effective electron (hole) density. In the case of finite gate voltage, i.e., $E_F \neq 0$, the

electron density of the homogeneous BLG for $s = 0$ is given by

$$n_{0e}(T) = D_0 E_F \left[1 + t \ln \left(1 + e^{-1/t} \right) \right], \tag{2.28}$$

where $t = T/T_F$ and $T_F = E_F/k_B$. The thermal excitation is exponentially suppressed due to the Fermi function at low temperatures ($T \ll T_F$), while at high temperatures ($T \gg T_F$) it increases linearly. In the presence of finite potential fluctuations ($s \neq 0$), the electron and hole density at zero temperature for the inhomogeneous system are given by:

$$n_e(0) = D_0 E_F \left[\frac{1}{2} \text{erfc} \left(\frac{-1}{\sqrt{2}\tilde{s}} \right) + \frac{\tilde{s}}{\sqrt{2\pi}} e^{-1/2\tilde{s}^2} \right],$$

$$\tag{2.29}$$

$$n_h(0) = D_0 E_F \left[-\frac{1}{2} \text{erfc} \left(\frac{1}{\sqrt{2}\tilde{s}} \right) + \frac{\tilde{s}}{\sqrt{2\pi}} e^{-1/2\tilde{s}^2} \right]$$

where $\tilde{s} = s/E_F$ and the difference of electron and hole density ($n = n_e - n_h = D_0 E_F$) is independent of the strength of potential fluctuation s (see Fig. 2.8(c)). At low temperatures ($T \ll T_F$) the asymptotic behavior of the electron density is given by

$$n_e(T) = n_e(0) + D_0 E_F \frac{\pi^2}{12\sqrt{2}} \frac{e^{-1/2\tilde{s}^2}}{\tilde{s}} \left(\frac{T}{T_F} \right)^2. \tag{2.30}$$

The leading order quadratic behavior of $n_e(T)$ as in undoped BLG ($E_F = 0$) is strongly suppressed by potential fluctuation. For the situation $s > E_F$, the existence of electron-hole puddles gives rise to a notable quadratic behavior [see Fig. 2.8(b)]. At high temperatures ($T \gg T_F$) we find

$$n_e(T) = n_{0e}(T) + \frac{D_0 E_F}{(1 + e^{\beta E_F})^2} \frac{\tilde{s}^2}{2} \frac{T_F}{T}. \tag{2.31}$$

where the linear temperature dependence of electron density is dominant as the homogeneous system.

2.4 Conductivity of inhomogeneous BLG

With the help of total electron and hole density calculated above, we will derive the temperature dependent conductivity for BLG in the presence of electron-hole puddles. We will apply both Boltzmann theory[14] and effective medium theory[69] to interpret the intriguingly insulating behavior observed in BLG samples[54, 12, 56].

The density and temperature dependent average conductivities in BLG, denoted as σ_e and σ_h, are given within the Boltzmann transport theory:

$$\sigma_e = \frac{n_e e^2 \langle \tau \rangle}{m}$$

$$(2.32)$$

$$\sigma_h = \frac{n_h e^2 \langle \tau \rangle}{m}$$

where n_e and n_h are average electron and hole densities, respectively. $\langle \tau \rangle$ is the transport relaxation time for bilayer graphene:

$$\langle \tau \rangle = \frac{\int d\epsilon D_e(\epsilon) \epsilon \tau(\epsilon) (-\partial f/\partial \epsilon)}{\int d\epsilon D_e(\epsilon) f(\epsilon)} \tag{2.33}$$

and $\tau(\epsilon)$ is calculated with Eq. 5.10. But for BLG systems, one needs to use the parabolic dispersion relation $\epsilon_{p\mathbf{k}} = p\hbar^2 k^2/2m$ for the pseudo-spin state "p" and the static dielectric screening function derived in Ref. [71]. The wave function form factor associated with the chiral nature of BLG is also different from the case in MLG, which is given by $g(\theta_{\mathbf{kk'}}) = [1 + \cos 2\theta_{\mathbf{kk'}}]/2$. To determine the average scattering time in BLG, we take into account the long-range charged impurity scattering and short-range defect scattering, which has been established that both contribute significantly to bilayer graphene transport properties[14]. The activated conductivities should also be included in the presence of density inhomogeneity in the BLG, which

follow the same relation as given for MLG :

$$\sigma_e^{(a)}(V) = \sigma_e \exp[\beta(E_F - V)], \tag{2.34a}$$

$$\sigma_h^{(a)}(V) = \sigma_h \exp[\beta(V - E_F)], \tag{2.34b}$$

2.4.1 $\sigma(T)$ of BLG at CNP

When electron-hole puddles form in the BLG samples (denote the electron (hole) puddle as region '1' ('2')), the transport properties can be treated with effective medium theory as described in Sec. 2.2. And Eqs. 5.1-2.22 for the inhomogeneous MLG also apply to the inhomogeneous BLG system. We will first discuss the total conductivity of BLG at CNP ($E_F = 0$). In this case, the electron and hole are equally occupied and the total conductivity $\sigma_t = \sigma_1$ (see Eq. 2.21a and 2.22). At low temperature limit ($T \ll s/k_B$), the activated conductivities increase linearly with a slope $\sqrt{2/\pi}k_B/s$ as the temperature increases. The next order temperature correction to the conductivity is quadratic T^2, which arises from the thermal activation (see Eq. 2.26). Thus, at low temperature limit the total conductivity at CNP is given by

$$\sigma_t(T) = \sigma(0)\left[1 + \sqrt{\frac{2}{\pi}}\frac{k_BT}{s} + \frac{\pi^2}{6}\left(\frac{k_BT}{s}\right)^2\right]. \tag{2.35}$$

At high temperatures ($k_BT \gg s$), the total conductivity is given by:

$$\sigma_t = \sigma_e\left[2 - \sqrt{\frac{2}{\pi}}\frac{s}{k_BT} + \frac{s^2}{2(k_BT)^2}\right]. \tag{2.36}$$

It is apparent that the activation behavior approaches a limiting value in the high temperature limit ($T \gg s/k_B$) while the thermally activated electron density becomes dominant, which increases linearly with a universal slope $\ln(2)$ regardless

of the sample quality. Thus, all temperature dependence of the total conductivity comes from the thermal excitation through the change of the carrier density given in Eq. (2.27). In Fig. 2.9 we show the calculated temperature dependent conductivity at charge neutral point. The inset present the activated conductivity versus the temperature. In Ref. [54], $\sigma_t(T)$ at the CNP of the BLG sample increases almost two times as temperature T varies from 4 K to 300 K. Our theoretical analysis using a potential fluctuation parameter $s \sim 40$ meV gives reasonable agreement with the experimental data.
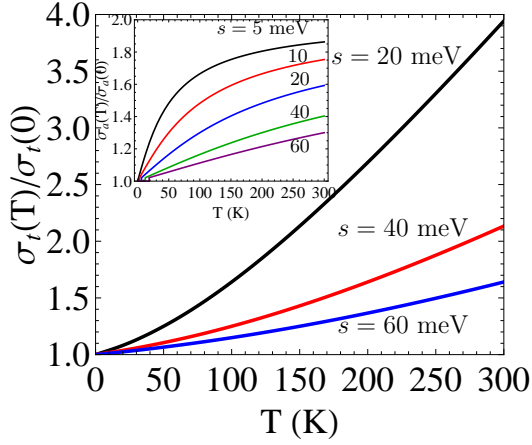
Figure 2.9: $\sigma_t(T)$ of BLG at charge neutral point for different s (Eq. 2.21a with n_e for BLG). Inset shows the thermally activated conductivity in BLG as a function of temperature, where $\sigma_a(T)/\sigma_a(0) = 1 + e^{\beta^2 s^2/2}\mathrm{erfc}(\beta s/\sqrt{2})$, the same as for the MLG case.

2.4.2 $\sigma(T)$ of BLG at finite doping ($E_F > 0$)

The temperature dependent conductivities at finite doping ($E_F > 0$) are very complex because three energies (E_F, s, and $k_B T$) are competing. Regardless of E_F, when $k_B T \ll s$, we have the asymptotic behavior of conductivities in region 1 and 2 the same as MLG situation, given in Eq. (2.25). But the average electron and

hole conductivities (σ_e and σ_h) are quite different from the MLG case, which is determined by the specific band dispersion relation and also the dielectric function $\epsilon(q, T)$. Thus, the leading order correction to σ_t in BLG is also linear, which comes from the activated conductivity, but the coefficient is exponentially suppressed by the term $\exp(-E_F^2/2s^2)$. In the high mobility sample with small s, the activated conductivity is weakly temperature dependent except around CNP, i.e. $E_F < s$. Since the density increase by thermal excitation is also suppressed exponentially by the same factor [see Eq. (2.30)] the dominant temperature dependent conductivity arises from the scattering mechanism[1]. On the other hand, in the low mobility sample with large value of s, the linear temperature dependence due to thermal activation can be observed even at high carrier densities $E_F \gtrsim s$.
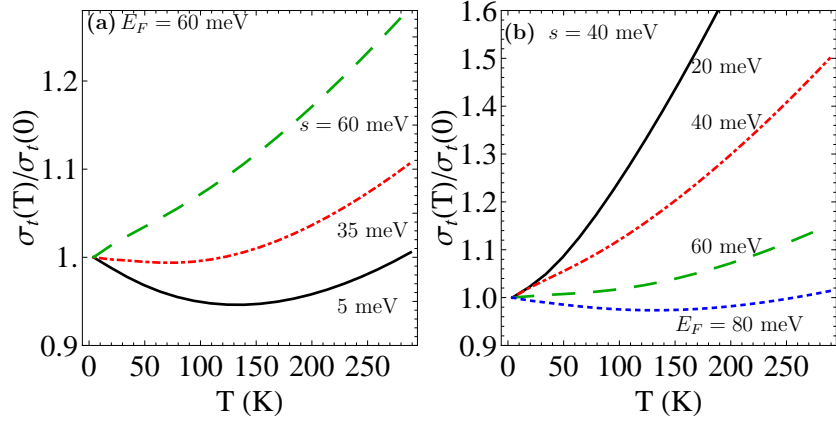
Figure 2.10: Calculated total conductivity $\sigma_t(T)/\sigma_t(0)$ of BLG with the following parameters: $n_i = 10^{12}$ cm^{-2} and $n_d V_0^2 = 2$ (eV Å)^2. (a) $\sigma_t(T)$ for $E_F = 60$ meV and for different s. (b) $\sigma_t(T)$ for $s = 40$ meV and for several $E_F = 20, 40, 60, 80$ meV, which correspond to the net carrier densities $n = n_e - n_h = 0.55 \times 10^{12}$, 1.1×10^{12}, 1.6×10^{12}, and 2.2×10^{12} cm^{-2}.

In Fig. 2.10 we calculate the total conductivities (a) for a fixed E_F and several s and (b) for a fixed s and several E_F. Even for homogeneous BLG, there are two

scattering mechanism competing with each other. The short-range disorder in BLG contributes to a strong insulating transport behavior for all temperature, whereas screened Coulomb scattering always leads to a metallic behavior for $T \ll T_F$[14]. At low temperature limit, the total conductivity $\sigma_t(T)$ decreases with increasing temperature, but at higher temperatures, the short-range disorder contribution becomes quite big and leads to a $\sigma_t(T)$ increasing with T. Therefore, when s is small, the scattering mechanism is dominant and the total conductivity displays a non-monotonic temperature dependence (see Fig. 2.10(a)). However, for large s the activated temperature dependence behavior overwhelms the metallic temperature dependence, and the system shows insulating behavior (see Fig. 2.10(b)). It clearly shows that the insulating behavior in the BLG sample appears at carrier densities as high as 10^{12} cm^{-2} or higher. We mention that in bilayer graphene, the transport property is dominated by Coulomb scattering even at room-temperature because phonons are effectively screened by the additional graphene layers[54]. Our analytic theory appears to be in excellent qualitative agreement with the existing experimental results[54].

2.5 Connection to earlier theories

We have demonstrated theoretically that the observed insulating behavior in temperature-dependent monolayer and bilayer graphene conductivity can be explained by the thermal activation between puddles. There are also other theories which have been elaborated to explain low carrier density graphene transport

[20, 24, 14]. In this section, we establish the bridge to connect our current theory and earlier theories on graphene transport due to the formation of inhomogeneous electron-hole puddles near the charge neutrality point.

The key qualitative difference between our theory and all earlier graphene transport theories is the introduction of the 2-component transport model where regular diffusive metallic carrier transport coexists with local activated transport due to activation across potential fluctuations in the puddles. Our theory just explicitly accounts for the inhomogeneous landscape in the system, which earlier theories ignored. This 2-component nature of graphene transport, where both metallic and insulating behavior coexist because of the existence of puddles, produces the experimentally observed complex temperature dependence with the low-density behavior being primarily insulating-like and the high-density behavior being primarily metallic-like.

Two different theories have been developed to study the low-density transport in graphene, where the strong density inhomogeneity is dominated. In Ref. [20] Adam et $al.$ qualitatively explained the plateau-like approximate nonuniversal minimum conductivity at low carrier density observed in monolayer graphene samples. The basic idea is to introduce an approximate pinning of the carrier density at $n = n^* \approx n_i$ at low carrier density limits $|n| < |n_i|$, where n_i is an impurity density. The constant minimum conductivity is then given by $\sigma_{min} \sim \sigma(n = n_i)$ for $n < n_i$. This simple theory for monolayer graphene transport qualitatively explained the existence of conductivity minimum plateau and the extent to which the minimum conductivity is not universal, which was in good agreement with

the observed density-dependent conductivity over a wide range of charged impurity densities[9, 10]. However, this theory did not take account of the highly heterogeneous structure near charge neutrality point and the thermally activated conductivity at finite temperatures, which then can not explain the observed non-monotonic temperature dependent transport in low mobility graphene samples[21].

A more elaborate Thomas-Fermi-Dirac (TFD) theory and an effective medium approximation (EMT) have been introduced in Refs. [22] and [24] to study the electrical transport properties of disordered monolayer graphene. The ground state density landscape $n(\mathbf{r})$ can be obtained within this TFD approach and the resultant electrical transport can be calculated by averaging over disorder realizations and the effective medium theory. This theory gives a finite minimum conductivity and is able to explain the crossover of the density-dependent conductivity from the minimum value at the Dirac point to its linear behavior at higher doping. Later, this TFD-EMT theory is also applied to calculate the conductivity of disordered bilayer graphene in Ref. [14]. The TFD-EMT technique successfully explains the graphene, both MLG and BLG, transport properties in the theoretically difficult inhomogeneity-dominant regime near the charge neutral point, but this approach fails to explain the temperature dependence of the conductivity for a wide range of temperatures.

In our current model discussed above, we include three effects, the electron-hole structure formation, the thermal activated conductivities and the temperature dependence of screening effects, to explain the temperature-dependent conductivity in both monolayer and bilayer graphene systems. The nonmonotonic temperature-

45

dependent conductivity in graphene systems is then naturally understood from the competition between the thermal activation of charge carriers and the temperature-dependent screening effects. Our transport theory qualitatively explains the observed coexisting metallic and insulating transport behavior in both MLG and BLG systems. For low mobility MLG samples, the dominant role on graphene conductivity switches from the thermally activated transport of inhomogeneous electron-hole puddles to metallic temperature-dependent screening effects, which gives rise to a nonmonotonic behavior from the strong insulating behavior at low temperatures to metallic behavior at high temperatures. On the other hand, another nonmonotonic temperature-dependent transport can be observed in very high mobility bilayer graphene devices, i.e., from metallic behavior at low temperatures due to the screening effects of Coulomb scattering to insulating behavior at high temperatures due to the short-range disorder. The merit of our model is that it is so simple that we could get the asymptotic behavior at low and high temperature limits analytically. Moreover, it provides a clear physical picture of the dominant mechanisms at different regimes as discussed above.

2.6 Discussions

We first discuss the similarity and the difference between MLG and BLG transport from the perspective of our transport-theory considerations. We find that both manifest an insulating behavior in $\sigma_t(T)$ for low mobility samples. We also find that both systems could exhibit a non-monotonic temperature dependent

conductivity for low mobility samples. However, the physical origin for the non-monotonic temperature dependence is quite different in the two systems: in the MLG the non-monotonic feature comes from the competition between thermal activation and the metallic screening effects, which leads to $\sigma_t(T)$ first increasing and then decreasing with increasing temperature (see Fig. 2.6(a)). For BLG, the competition between short-range insulating scattering and metallic Coulomb screening effects leads to $\sigma_t(T)$ first decreasing and then increasing as temperature increases (see Fig. 2.10(a)). Most important quantitative difference between MLG and BLG transport comes from their band dispersions, which leads to much weaker effects of density inhomogeneity in MLG so that the anomalous insulating temperature dependence of $\sigma(T)$ is typically not observed in MLG away from the CNP although the gate voltage dependence of MLG and BLG conductivities are similar[72, 73]. The linear Dirac carrier system for MLG leads to linear DOS, which goes to zero at CNP, but the parabolic band dispersion relation in BLG leads to a constant DOS. Due to the difference in the density of states between homogeneous MLG and BLG, the modified DOS in inhomogeneous MLG is increased (see Fig. 2.3) rather than decreased in inhomogeneous BLG (see Fig. 2.7). The dimensionless potential fluctuation strength $\tilde{s}$ ($\equiv s/E_F$) is much weaker in MLG than in BLG from simple estimates: $\tilde{s}_{BLG}/\tilde{s}_{MLG} \sim 32/\sqrt{\tilde{n}}$ where $\tilde{n} = n/10^{10}$, and $\tilde{s}_{BLG} \gg \tilde{s}_{MLG}$ upto $n = 10^{13}$ cm^{-2}. Direct calculations [1] show that the self-consistent values of s tend to be much larger in BLG than in MLG for identical impurity disorder. In addition, the qualitatively different DOS leads to much stronger effective short-range scattering in BLG compared with MLG even for the same bare scattering

47

strength. Thus, the insulating behavior in $\sigma_t(T)$ will show up at high temperatures even for relatively higher mobility BLG samples (i.e., small s). In contrast, only in very low mobility MLG samples, where s is very large, can the insulating behavior of temperature dependent resistivity be observed[47, 21]. No simple picture would apply to a gapped (Δ_g) BLG system, since four distinct energy scales ($s, E_F, k_B T$, and Δ_g) will compete and the conceivable temperature dependence depends on their relative values[2, 74, 75]. Our assumption of BLG quadratic band dispersion is valid only at low ($\lesssim 5 \times 10^{12}$ cm^{-2}) carrier densities, where most of the current transport experiments are carried out. At higher densities the band dispersion is effectively linear and the disorder effects on $\sigma_t(T)$ are weaker.

We emphasize that our theory is physically motivated since puddles are experimental facts in all graphene samples. Puddles automatically imply a 2-component nature of transport since both diffusive carriers and activated carriers can, in principle, contribute to transport in the presence of puddles. Of course, the effect of puddles is much stronger at low carrier densities, explaining why insulating (metallic) temperature dependence is more generic at low (high) graphene carrier densities. We emphasize that local carrier activation in puddles is just one of (at least) four different independent transport mechanisms contributing to the temperature dependent conductivity. The other three are temperature dependent screening (Ref. [49]), phonons (Refs. [57, 58]), and Fermi surface thermal averaging (Refs. [49, 68]). Our theory presented here includes the three electronic mechanisms for temperature dependence: screening, Fermi surface averaging, and puddle activation. We leave out phonons, which have been considered elsewhere (Ref. [57, 58]) and will simply add to

the temperature dependent resistivity. The weak phonon contribution to graphene resistivity makes it possible for the electronic mechanisms to dominate even at room temperatures, but obviously at high enough temperatures, the system will, except perhaps at the lowest densities around the CNP, manifest metallic temperature dependence with the resistivity increasing with temperature because of phonon scattering. Similarly, the puddle effects dominate low densities and therefore, the insulating behavior will persist to very high temperatures around the zero-density CNP since activation across potential fluctuations are dominant at the CNP. It is gratifying to note that these are precisely the experimental observations. We note that in general the temperature dependent conductivity of graphene could be very complex since many distinct mechanisms could in principle contribute to the temperature dependence depending on the carrier density, temperature range, and disorder in the system. Inclusion of phonons (at high temperatures) and quantum localization (at low temperatures) effects, which are both neglected in our theory, can only complicate things further. What we have shown is that the low-density conductivity near the CNP is preferentially dominated by density inhomogeneity and thermal carrier activation effects leading to an insulating temperature dependence in the conductivity whereas the high-density conductivity, where the puddles are screened out, is dominated by a metallic conductivity due to temperature-dependent screening effects. This general conclusion is consistent with all experimental observations in both MLG and BLG systems to the best of our knowledge except at very high temperatures where phonon effects would eventually lead to metallic behavior at all densities.

Chapter 3

Disorder by order in graphene

An electronic material, metal or doped semiconductor, typically exhibits higher low-temperature conductivity as the amount of quenched random disorder is decreased in the system, i.e., as the system becomes more ordered. It is therefore a universal expectation that a purer metal with lower impurity disorder would always exhibit higher low-temperature conductivity than a dirtier metal with higher disorder.

In this chapter, we theoretically establish a counter-intuitive possibility in graphene which is in sharp contrast to the universal scenario of increasing conductivity with increasing order. We show that in monolayer graphene, with its gapless chiral linear 2D electron-hole Dirac band dispersion, the resistivity (conductivity) will increase (decrease) monotonically with decreasing carrier density near the charge neutrality (Dirac) point provided the system is sufficiently pure, i.e., ordered, with very little residual background charged impurity disorder. Not only will the Dirac point resistivity be anomalously large in high-purity graphene, the transport behavior itself will be insulating-like at the charge neutrality point with the resistivity increasing monotonically with decreasing temperature! On the other hand, as the carrier density increases, the resistivity will decrease with the eventual

restoration of the metallic behavior manifesting a weakly temperature dependent resistivity above a non-universal crossover density which would depend on the residual background charged impurity disorder and the temperature. At high density, far away from the charge neutrality point with vanishing average charge density, the high-purity graphene sample would behave in a perfectly normal manner manifesting very high mobility (and very long mean free path) consistent with the highly ordered nature of the system with very little residual Coulomb impurity scattering. We dub this strange dichotomy where decreasing disorder drives the graphene layer into an effective insulating state at low carrier density near the charge neutrality point, while maintaining very high mobility at high carrier density consistent with its low disorder, the phenomenon of "disorder by order". We emphasize that our predicted disorder by order phenomenon is not a $T = 0$ quantum phase transition as in an Anderson or Mott transition, it is a transport crossover phenomenon manifesting itself as an effective density-tuned metal-insulator transition. In particular, quantum localization plays no role in our theory which is developed entirely within the semiclassical Boltzmann transport model neglecting all quantum interference corrections. The disorder by order phenomenon arises from an interplay among charged impurity disorder, density inhomogeneity (the so-called "electron-hole" puddles[20, 76, 19, 52, 51, 1]), and the peculiar gapless linear chiral band dispersion of graphene. Our predicted novel semiclassical phenomenon would dominate low-density transport in ultrapure graphene samples as long as quantum interference induced localization corrections are small, i.e., in the effective high-temperature semiclassical regime where the inelastic phase breaking length is comparable to or

51
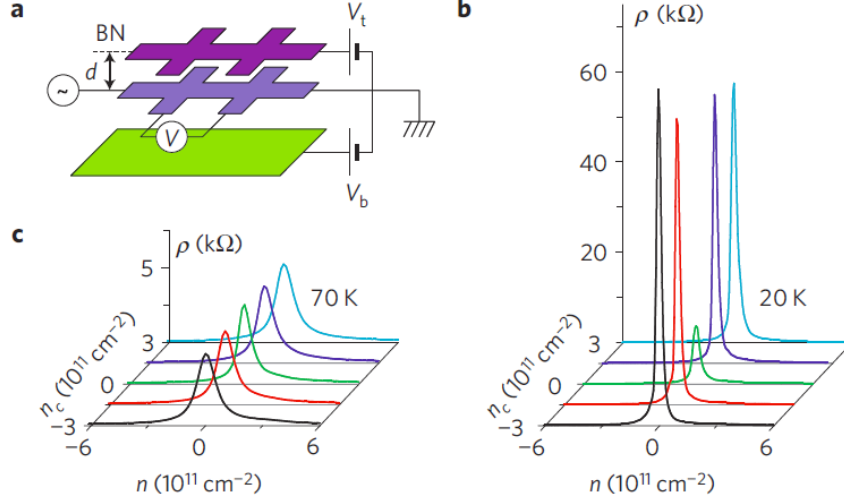
Figure 3.1: Electron transport measured in graphene-boron nitride heterostructures. (a) Schematic diagram of graphene-boron nitride heterostructure devices and measurement geometry. (b) and (c) Resistivity ρ as a function of carrier density n in the studied graphene layer for different doping n_c of the control layer at two temperatures. The device has a 4 nm BN spacer. Adapted from Fig. 1 of Ref. [41].

smaller than the elastic transport mean free path.

We believe that our predicted graphene "disorder by order" phenomenon has recently been experimentally observed by Ponomarenko et $al.$ [41], who, however, interpret their observation as the manifestation of a density-tuned metal-insulator localization transition. The experiment studied a double-layer electronic system made of two closely-spaced but electrically isolated graphene monolayers sandwiched in boron nitride [41] (see Fig. 3.1(a)). The top and the bottom layer are referred to as the studied and control layers. When the carrier density n_c is low in the control layer, the studied layer exhibits the standard behavior with a minimum metallic conductivity. However, for $n_c > 10^{11}$ cm^{-2}, the resistivity of the studied layer diverges near the neutrality point (NP) at $T < 70K$ (see Figs. 3.1 (b) and (c)). In addition, it has been found that charge fluctuations in the studied layer
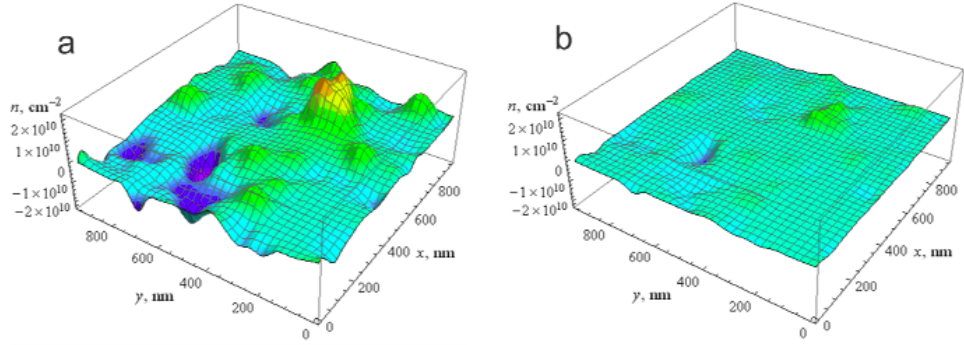
Figure 3.2: Simulated e-h puddles in the studied graphene layer for carrier densities $n_c = 0$ and 5×10^{11} cm^{-2} of the control layer (top and bottom panels, respectively). Adapted from Fig. S4 in the Supplementary Information of Ref. [41].

are strongly suppressed for highly doped control layer (see Fig. 3.2). All aspects of the experimental data reported in Ref. [41], in particular the density and the temperature dependence of the measured conductivity, agree spectacularly well with our predictions, and we therefore contend that the observation in Ref. [41] is a direct experimental verification of our predicted "disorder by order" phenomenon. Particularly germane in this context is the fact that the transport data of Ref. [41] were taken in the relatively high-temperature $(10 - 100$ K$)$ regime where quantum interference effects are not important, and our semiclassical transport theory should apply.

In this chapter, the basic transport theory and the numerical results are presented. Then, we discuss the results compared to experimental data.

3.1 Theory and Numerical results

We first provide a simple physical picture underlying the "disorder by order" phenomenon. Let us assume that the graphene sample is pristine with essentially no

background random charged impurities so that the effective transport relaxation or scattering time τ is very long, leading to very high (low) conductivity (resistivity) at an electron density of n. The conductivity is given (at $T = 0$) within the Boltzmann transport theory[1, 16] by $\sigma = \frac{e^2 v_F^2}{2} D(E_F)\tau(E_F)$, where v_F is the constant graphene Fermi velocity defining its linear band dispersion, $D(E_F) \propto \sqrt{n}/v_F$ is the graphene density of states at the Fermi energy $E_F \propto v_F\sqrt{n}$. The scattering time $\tau(E_F)$ for the screened Coulomb scattering due to random background charged impurities has been calculated [1, 16, 77, 15] in the literature, giving $\tau \propto \sqrt{n}$, which leads to the now-well-known formula [16] for graphene conductivity due to random charged impurity scattering given by

$$\sigma(n) = A \frac{n}{n_i} \frac{e^2}{h} \tag{3.1}$$

where n_i is the effective background 2D concentration of the random charged impurities (including its location and strength) whereas A is a constant which depends on the dielectric environment of the system (e.g., substrate)–for graphene on SiO_2 (h-BN), $A \approx 20$ (26). The result given in Eq. 3.1 and the underlying general theory for graphene carrier transport have been well-verified experimentally in the literature[10, 9, 78, 54, 79, 80, 21]. An immediate consequence of Eq. 3.1, interpreted naively, is that the graphene resistivity $\rho(\equiv 1/\sigma)$ diverges as n^{-1} at the Dirac point where the carrier density vanishes by virtue of the vanishing density of states at the Dirac point.

In reality, however, this divergent Dirac point resistivity (or equivalently, vanishing conductivity) is not observed experimentally in real graphene samples, which

manifest a conductivity saturation phenomenon at low carrier density ($|n| \lesssim n^*$[20]) with an approximate minimum conductivity plateau $\sigma_{min} \sim An^*/n_i$, where n^* is a characteristic disorder-dependent density[20, 1]. This conductivity minimum phenomenon was already apparent in the pioneering graphene experiments by Novoselov and Geim[81, 7, 8], and was later studied extensively quantitatively[10, 9, 78, 54, 79, 80], and is now accepted as arising from the charged impurity disorder induced inhomogeneous electron-hole density puddles which dominate the graphene landscape[19, 52, 51] at low carrier density. These puddles of strong real-space density inhomogeneities arise from the low-density failure of screening of the individual charged impurities with electrons/holes preferably accumulating near/far from individual discrete impurities depending on the sign of the impurity charge[22]. Thus, as the gate voltage decreases, the average density decreases, but electron-hole puddle formation leads to an effective saturation of the conductivity at some low sample-dependent minimum value. The inhomogeneous puddles simply cut off the $\rho \sim 1/n$ behavior of graphene resistivity for $n \lesssim n^*$ since the real 2D density across the graphene sample never vanishes although the average density does, allowing for percolating transport through the electron-hole puddles at the charge neutrality point[20].

What would happen if the electron-hole puddles are somehow eliminated or suppressed in the system? Within the semiclassical Boltzmann picture, the resistivity will become very large as the average density is decreased by lowering the gate voltage since the puddles leading to the low-density conductivity saturation phenomenon no longer exist! This is a direct (and dramatic) manifestation of the

gaplessness of graphene, and cannot happen in the semiconductors with band gaps.

The easiest way to eliminate (or suppress) the puddles is, of course, to reduce the environmental charged impurity density (n_i) which induces the puddles to start with. But such a low-disorder system will necessarily manifest very low resistivity (since $\rho \propto n_i$) at high carrier density ($\rho \propto 1/n$), but very high resistivity near the Dirac point since $n \to 0$. If the puddles disappear completely, the resistivity will diverge as $1/n$ as the carrier density decreases. Therefore, the disorder-by-order phenomenon is peculiar to gapless graphene with its linear dispersion. It is obvious from the above physically-motivated discussion based on a qualitative extension of existing results in the literature[20, 1, 16, 22] that this counter-intuitive "disorder-by-order" phenomenon would be more apparent if the inhomogeneous electron-hole puddles could be further suppressed around the Dirac point by applying an external screening potential through a gate which would screen out the puddles, as has been successfully done in Ref. [41].

The above-discussed semiclassical "disorder-by-order" phenomenon has recently been observed in the experiment of Ponomarenko *et al.* [41], who reported monotonic increase of the graphene resistivity with decreasing carrier density in an ultrapure sample on h-BN substrate. This remarkable resistivity enhancement with decreasing density occurs only in the presence of a second nearby high-density graphene layer which screens out the puddles, thus avoiding the "minimum-conductivity" saturation phenomenon around the Dirac point.

In Fig. 4.3 we present our theoretically calculated transport results as a function of average carrier density for the experimental situation studied by Pono-

marenko *et al.* [41]. The different colors in Fig. 4.3 correspond to different temperatures whereas different panels correspond to different electron-hole puddle configurations characterized by the disorder induced potential fluctuation parameter 's' where 's' corresponds to the root mean square potential fluctuations in the probability distribution function $P(V)$ for the impurity-induced disorder, $P(V) \sim e^{-V^2/2s^2}/\sqrt{2\pi s^2}$, assumed to be Gaussian for simplicity – the Gaussian approximation is very accurate compared with the realistic numerical calculations[22, 1] of $P(V)$. The inhomogeneity parameter 's', which depends on the impurity disorder in the system, is directly connected to the root-mean-square density fluctuation n_{rms} in the inhomogeneous electron-hole puddles. The precise relationship between s and n_{rms} can only be obtained through a full numerical self-consistent calculation[22, 1], but within a simple mean-field theory $n_{rms} \propto s^2$. We note that $n_{rms} \sim n^*$ defines the cut-off for the minimum conductivity $\sigma_{min} \sim n_{rms} \sim s^2$ around the Dirac point as discussed above. As $s \to 0$, $\rho_{CNP} = 1/\sigma_{min}$ diverges as s^{-2} in mean field theory. We note that the potential fluctuation s (or equivalently, the root mean square density fluctuation in the puddles) is being controlled by external gating through the second graphene layer in Ref. [41], and the new feature of Ref. [41], not achieved before, is that s could be made very small.

For the sake of comparison, we have reproduced in Fig. 4.3(f) the corresponding experimental results from Ref. [41]. The agreement between our calculated theoretical results and the experimental data is striking: In the presence of substantial (vanishing) electron-hole puddles characterized by larger (smaller) values of the disorder fluctuation parameter s, the calculated $\rho(n)$ saturates (increases mono-

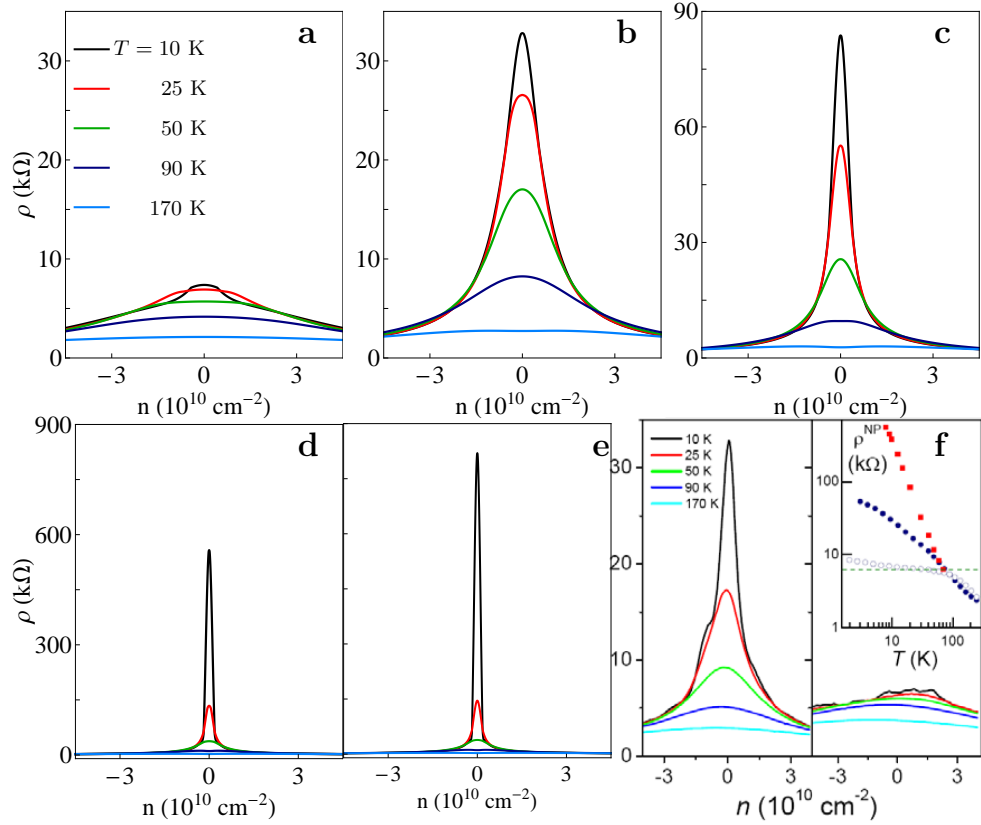Figure 3.3: Calculated $\rho(n)$ at different temperatures T for $n_i = 16 \times 10^{10}$ cm^{-2}. (a) The potential fluctuation parameter $s = 22$ meV. (b) $s = 10$ meV. (c) $s = 6.0$ meV. (d) $s = 1.0$ meV. (e) $s = 0.1$ meV. (f) Experimental data as shown in Ref. [41]. Comparison between (b) and (f) indicates a potential fluctuation parameter $s \sim 10$ mev in the experimental sample[41].

tonically) at lower average carrier density exactly as observed experimentally in the presence (absence) of the puddles. We emphasize that the theoretical results obtained in Fig. 4.3 use exactly the same parameters for all cases except for varying the value of the potential fluctuation parameter 's' as given in the figure (which mimics the effect of the suppression of s through screening by the second graphene layer in Ref. [41]). One interesting prediction of our theory is that $\rho(n)$ never truly diverges as $1/n$ in our theory as $n \to 0$ (unless $s = 0$ exactly, which is unphysical) since there is always a low-density cut-off n^* defining the conductivity minimum regime with n^* decreasing with decreasing s. This low-density cut-off (and the corresponding "maximum resistivity" ρ_{max}) depends strongly on the puddle parameter 's' – the suppression of 's' dramatically increases (decreases) $\rho_{max}(n^*)$.

Before discussing our results for the temperature dependence of the resistivity $\rho(T)$, we briefly discuss our transport theory [20, 1, 16, 22, 70, 40] for graphene conductivity in the presence of electron-hole puddle induced strong density inhomogeneity. The conductivity is obtained by using the effective medium theory (EMT) by solving the integral equation

$$\int dn \frac{\sigma(n) - \sigma_{EMT}}{\sigma(n) + \sigma_{EMT}} P[n] = 0 \qquad (3.2)$$

where σ_{EMT} is the effective conductivity of the sample and $\sigma(n)$ is the density $n(\boldsymbol{r})$ dependent local conductivity with the carrier density n having the distribution $P(n) = \exp[-(n - n_0)^2/2n_{rms}^2]/\sqrt{2\pi n_{rms}^2}$ defining the electron-hole puddles – here n_0 is the average density defined by the external gate voltage (i.e., $n_0 = 0$ at the charge neutral Dirac point) and n_{rms} is the root-mean-square density fluctuation

59

due to the existence of density inhomogeneity associated with the puddles. We calculate $\sigma(n)$ using the finite-temperature Boltzmann-RPA transport theory using screened random quenched charged impurity centers (of 2D concentration n_i) in the environment as the resistive scattering mechanism. The Boltzmann transport theory, which has been described in details elsewhere[1, 16, 70, 49, 68, 40] , includes five distinct temperature-dependent contributions: (1) thermal activation of electron-hole occupancy (i.e. thermal excitation of electrons from the valence band to the conduction band); (2) finite temperature thermal averaging around the Fermi surface according to the Fermi distribution function; (3) the thermal activation of carriers over the potential fluctuations associated with the electron-hole puddles; (4) finite temperature screening by the carriers themselves; (5) phonon effects (which are straightforward to include[57, 58], but are neglected here since electron-phonon coupling is weak in graphene). The thermal effects (1)-(3) above produce 'insulating' temperature dependence, i.e., the temperature-dependent resistivity $\rho(T)$ increases with decreasing T, whereas the last two effects lead to a 'metallic' $\rho(T)$ decreasing with decreasing temperature. All the thermal effects are suppressed with increasing carrier density (or more precisely, increasing E_F), and they are the strongest at the charge neutral Dirac point (where the nominal E_F vanishes). We note that in our figures, $\rho \equiv \sigma_{EMT}^{-1}$ whereas the density $n \equiv n_0$, i.e., the average density.

In Fig. 3.4 we depict our calculated $\rho(T)$ at fixed n including puddle effects (characterized by the parameter s) within the Boltzmann transport theory as described above (and elsewhere[70, 49, 68, 40]). The calculated temperature dependent resistivity is identical to the experimental observations of Ref. [41], as reproduced

60
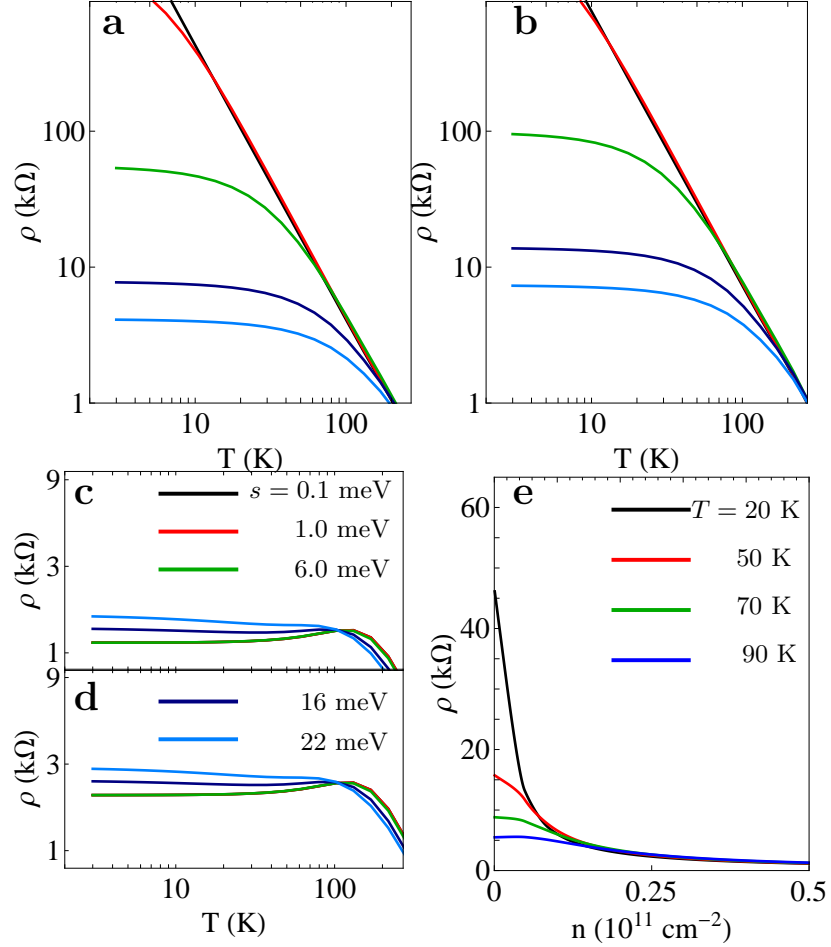
Figure 3.4: Calculated $\rho(T)$ for different values of the potential fluctuation parameter s. (a) and (b) correspond to $n = 0$, i.e., the Dirac point. (c) and (d) correspond to high carrier density $n = 5 \times 10^{10}$ cm^{-2}. (a) and (c) $n_i = 9 \times 10^{10}$ cm^{-2} with mobility at high carrier density $\mu = 10^5$ cm^2/Vs. (b) and (d) $n_i = 16 \times 10^{10}$ cm^{-2} with mobility at high carrier density $\mu = 6 \times 10^4$ cm^2/Vs. The decrease of ρ for $T > 100$ K in (c) and (d) is a real effect arising from the Fermi surface averaging[49, 68] which becomes quantitatively important at these densities – this effect is suppressed by phonon scattering which comes into play for $T > 100$ K. (e) $\rho(n)$ for different values of T are shown for $s = 5$ meV and $n_i = 9 \times 10^{10}$ cm^{-2}.

in our Fig. 4.3(f), with the Dirac point resistivity increasing strongly with lowering temperature for smaller values of s (i.e., when the potential fluctuations associated with the electron-hole puddles are strongly suppressed) whereas the resistivity at high carrier density manifesting almost temperature-independent behavior. We emphasize, however, that within our semiclassical transport theory, in spite of the very strong increase of the Dirac point $\rho(T)$ with lowering T for small s, eventually $\rho(T)$ saturates at some large s-dependent (and n_i-dependent) value at low enough $T \ll s$ even at the Dirac point – empirically we find that $\rho(T)$ at the Dirac point saturates for $T \lesssim s/5$. Then, the Dirac point behavior of $\rho(T)$ for different values of s is qualitatively similar if plotted as a function of $k_B T/s$. Therefore, one clear prediction of our semiclassical theory is that at low enough temperatures the experimentally measured $\rho(T)$ will always saturate even at the Dirac point, but the crossover temperature for this saturation would be very low when the electron-hole puddles are strongly suppressed. Thus, $\rho(n, T)$ in our theory would behave very much like a density-tuned metal-insulator transition, as observed in Ref. [41], for all practical purposes except that the temperature dependence would be a power law (and not an exponential as in a strongly localized system), exactly as seen in Ref. [41].

3.2   Discussion

One point we should make clear here about the "disorder by order" phenomenon is that it arises from the suppression of the electron-hole puddles associated with the density inhomogeneity around the Dirac point induced by Coulomb

disorder, and not simply from an impurity-induced collisional broadening effect in the graphene density of states. In particular, one may wonder whether the impurity broadening effect leading to a finite carrier density of states at the Dirac point could by itself lead to the disorder by order phenomenon since this would imply that a cleaner system would have a lower density of states at the Dirac point and hence a higher resistivity. While this is certainly true in general, i.e. when a material exhibits a density of states minimum, addition of disorder leads to an increased density of states near this minimum due to smearing which then leads to a higher Drude conductivity, this is not the primary operational mechanism for the disorder by order phenomenon. As we show in Appendix B, such an enhanced disorder-broadened density of states indeed leads to higher conductivity near the Dirac point for more disordered graphene samples, but the conductivity always vanishes at the Dirac point ($n = 0$) in this situation as long as Coulomb disorder (i.e. random charged impurities in the environment) is present in the system independent of whether the density of states is zero or finite at the Dirac point. In our proposed order by disorder mechanism, by contrast, the conductivity is *always* finite at the Dirac point because of the disorder-induced inhomogeneous puddles except that this finite minimum Dirac point conductivity arising from the puddles is much lower for the more ordered systems than it is for the more disordered systems while the reverse is true at high density. Thus, the presence (suppression) of puddles is the important physics in our disorder by order mechanism, not the disorder-induced smearing of the graphene density of states around the Dirac point. We discuss the issue of the density of states smearing effect on the graphene conductivity in Appendix B.

We now provide a critical discussion of our theory as applied to the experimental observations of Ref. [41]. First, our results provide an excellent description of the experimental observations with respect to the dependence of the measured resistivity as a function of carrier density, temperature, and disorder associated with the electron-hole puddles. Indeed, the agreement between our theory and the experimental data is striking, lending credence to our claim that the observation of Ref. [41] is an experimental verification of our predicted "disorder by order" phenomenon in monolayer graphene. A compelling point in this context is that the analytical prediction of our theory at the Dirac point, $\rho(T) \sim T^{-2}$ for $T > s$, is obeyed well both by our numerical results and by the experimental data of Ref. [41], arguing in favor of the disorder by order phenomenon being operational in the experimental observation in contrast to some other mechanism, e.g. localization, which typically leads to exponential T-dependence in the resistivity. In Ref. [41], the potential fluctuations associated with electron-hole puddles in the graphene layer were suppressed by a second close-by graphene layer with a very high carrier concentration. We have verified by direct numerical simulations that such a suppression can indeed be caused by the second high-density graphene layer separated by a distance d acting as a gate which screens the potential fluctuations reducing them substantially below their pristine value arising from the random charged impurity distribution. A simple electrostatic analytic calculation shows that the suppression of s would be approximately by a factor $1/(k_F d)$ when $k_F d \ll 1$. For $n \sim 10^{10}$ cm^{-1} and $d \sim 1$ nm, s could thus be suppressed by a factor as large as 50! Thus our basic picture of the suppression of the potential fluctuation parameter 's' leading to

the disorder by order phenomenon at the Dirac point is applicable to Ref. [41]. In Ref. [41], it is also found that the disorder-by-order phenomenon is itself suppressed by the application of a weak magnetic field $B \sim 10$ mT. We mention that a magnetic field $B \sim 10$ mT corresponds to a minimum Landau level energy separation ~ 4 meV which is comparable to E_F for $n \sim 10^9$ cm^{-2}. Thus, a 10 mT magnetic field is not a weak field at the Dirac point, which would nonperturbatively modify the physics, considerably suppressing the disorder by order phenomenon.

We believe that the disorder by order phenomenon should occur in any Dirac material with chiral gapless linear energy spectrum as long as quantum interference effects are negligible, and as such, we predict the existence of the same phenomenon in the 2D surface transport[82, 83] in 3D topological insulators provided that the surface puddles are suppressed in the system and the temperature is not too low. In fact, all gapless semiconductors will manifest the disorder by order phenomenon if impurity-induced potential fluctuations can be suppressed in the low carrier density regime. Indeed, we believe that some earlier graphene experiments [67, 66] observing anomalous temperature dependence of the Dirac point resistivity are observing exactly the same disorder-by-order phenomenon as reported in Ref. [41] except that the authors of Ref. [67, 66] interpret their observations as ballistic transport whereas Ponomarenko *et al.* [41] invoke Anderson localization!

Chapter 4

Graphene on SrTiO$_3$

The substrate material has significant influence on graphene transport properties, which has been confirmed by many different experimental groups[9, 10, 46, 54, 13, 55, 21, 84, 78, 66, 85, 80]. The extensively used model [1, 16, 20, 24, 40] of Coulomb disorder in the environment has earlier been found to provide a reasonable theoretical description for graphene transport on SiO$_2$ substrates from many different groups [9, 10, 46, 54, 13, 55, 21, 84] as well as on several other substrates [86, 80, 87]. In a recent paper [88], however, Couto *et al.* claim that the long-range Coulomb impurities do not play an important role based on their measured conductivity, $\sigma(n)$, of graphene at high carrier densities on SrTiO$_3$ substrates. In addition, they argued that their transport data can be explained quantitatively by a so-called "resonant scattering" model [89, 18], which gives the following expression for the carrier density (n) dependence of the conductivity σ: $\sigma(n) = \frac{2e^2}{\pi h} \frac{n}{n_i} \ln^2(\sqrt{n\pi R^2})$, where n_i, R are respectively the concentration and the range of the resonant scattering defects in graphene (see Fig. 4.1). Fig. 4.1(a) shows that the Dirac peaks measured at all different temperatures overlap nearly perfectly despite the large change in the background dielectric constant of the substrate [88] as shown in Fig. 4.2. The measured dielectric constant ε is approximately 200 at room temperature and it
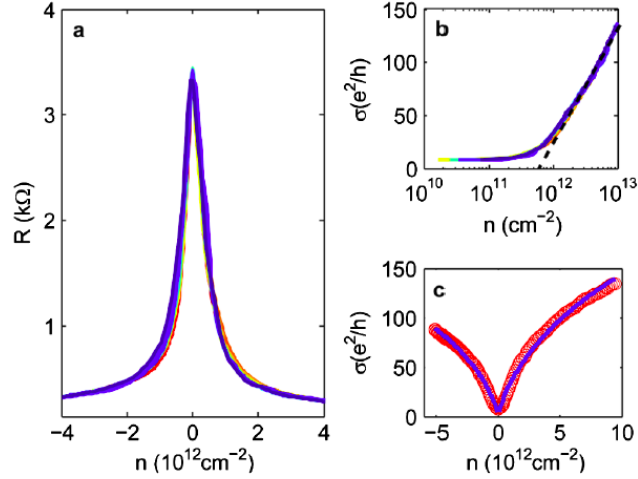
Figure 4.1: (a) Resistance of graphene on $SrTiO_3$ measured at different temperatures between 250 mK and 50 K, as a function of carrier density. (b) Conductivity of graphene on SrTiO3 as a function of n (in log scale) at different temperatures. (c) Fitting the experimental data by taking into account resonant scattering focusing on high carrier density regime. Adapted from Fig. 2 of Ref. [88].

increases monotonically with lowering temperature, reaching 7000 at 4K [88]. In addition, the value of ε strongly depends on the precise concentration of impurities in the $SrTiO_3$ crystals [88].

Motivated by this experiment[88], we revisit the question of the role of various types of disorder on different substrates in controlling the density-dependent conductivity of graphene, comparing, in particular, the low- and high-density conductivity limited by distinct scattering mechanisms. In particular, the low-density graphene transport behavior on $SrTiO_3$ (or for that matter, on any other substrate) is likely to be always dominated by long-range Coulomb disorder, independent of the other scattering mechanisms (e.g. short-range disorder, resonant scattering) which may be operational at high carrier density. One important finding of this work is to show that it is indeed possible for graphene transport to be determined by different scattering mechanisms at low and high carrier densities, a result which has been
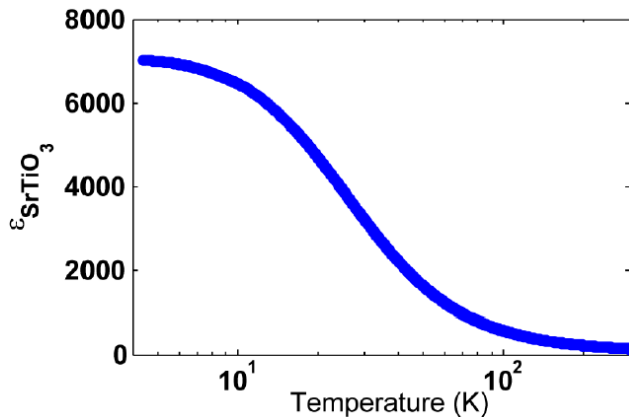
Figure 4.2: Experimentally measured SrTiO$_3$ substrates dielectric constant as a function of temperature. Adapted from Fig. S1 in the Supplementary Information of Ref. [88].

implicit in earlier works in this subject.

First, we note that a conductivity formula with $\sigma \sim \frac{n}{n_i} \ln^2(\sqrt{n/n_0})$ cannot, by definition, qualitatively account for the most important aspect of graphene transport, namely, the existence of the low-density minimum conductivity for a finite range of density around the Dirac (i.e. charge neutrality) point. Thus, the resonant scattering model, even in the most favorable circumstances, can only be a rather phenomenological data-fitting scheme for $\sigma(n)$ in an intermediate density range $n_c < n < n_0$ where n_c defines the density regime for the graphene minimum conductivity plateau around the Dirac point (taken to be at $n = 0$ in this comment) and $n_0 \equiv (\pi R^2)^{-1}$. Second, as no physical evidence for the existence of these "resonant scattering" short-range atomic defects (with $n_i \sim 3 \times 10^{11}$ cm^{-2}) is presented in Ref. [88] except for providing an intermediate-density phenomenological fit to their conductivity data, it is not clear whether the resonant scattering is the only scattering mechanism for graphene on SrTiO$_3$.

One interesting observation in Ref. [88] is the apparent absence of much temperature dependence in the graphene conductivity while the substrate dielectric constant $\kappa(T)$ is changing substantially as a function of temperature as the substrate material, i.e. $SrTiO_3$ undergoes a paraelectric to ferroelectric transition with the lowering of temperature. One possibility that cannot be ruled out in this context is that the substrate impurity density is also changing substantially during this temperature-induced substrate structural ferroelectric transition. In this work, we explicitly incorporate such a possibility in the theory for disorder limited graphene conductivity to compare with the data of Ref. [88]. We believe that the presence of some background Coulomb disorder is essential for understanding the low-density minimum conductivity behavior near the charge neutrality point in graphene on any substrate.

In this chapter, we show our best theoretical fits to the data of Ref. [88] in Fig. 4.3, finding that a dual model involving both Coulomb and resonant scattering disorder can well explain the data of Ref. [88] with the single assumption of a variable background charged impurity density with varying temperature. The assumption of a temperature-dependent charged impurity density for $SrTiO_3$ substrates is not an arbitrary data fitting ploy because the complicated lattice ferroelectric properties of $SrTiO_3$ leading to the strong functional dependence of the dielectric constant on temperature may very well also produce a temperature dependent charged impurity density increasing strongly with decreasing temperature just as the actual carrier density in graphene on $SrTiO_3$ increases rapidly with decreasing temperature at a fixed gate voltage (see Fig. 2 in the Supplementary Information of Ref. [88]).

In the remainder of this chapter, we demonstrate that resonant scattering by itself can never explain the experimental data in the whole carrier density range for any substrate since the low-density minimum conductivity behavior cannot be understood based on a model which includes only resonant scattering. We present our best theoretical fits to the experimental data in Ref. [88] for $SrTiO_3$ using the new theory of long-range Coulomb disorder and the resonant scattering defects. We establish that a simple model of a single type of scattering mechanism can not describe the transport data both at low and high carrier density for complex oxide substrates. We also compare three different models to explain transport properties of graphene on different substrates, finding that different behaviors of $\sigma(n)$ for different samples on different substrates are attributed to the competition among different scattering sources. The main message of this chapter illustrated through concrete calculations, but not emphasized explicitly in earlier works (although it might have been implicit), is that the high-density transport in graphene is nonuniversal and reflects the combination of various scattering processes arising from the substrate whereas the low-density transport is always dominated by long-range Coulomb disorder. In addition to the $SrTiO_3$ substrates used in Ref. [88], we also consider graphene transport on several other common substrates (e.g. SiO_2, h-BN, and vacuum) to make our point about the universality (nonuniversality) of the transport behavior at low(high) densities.
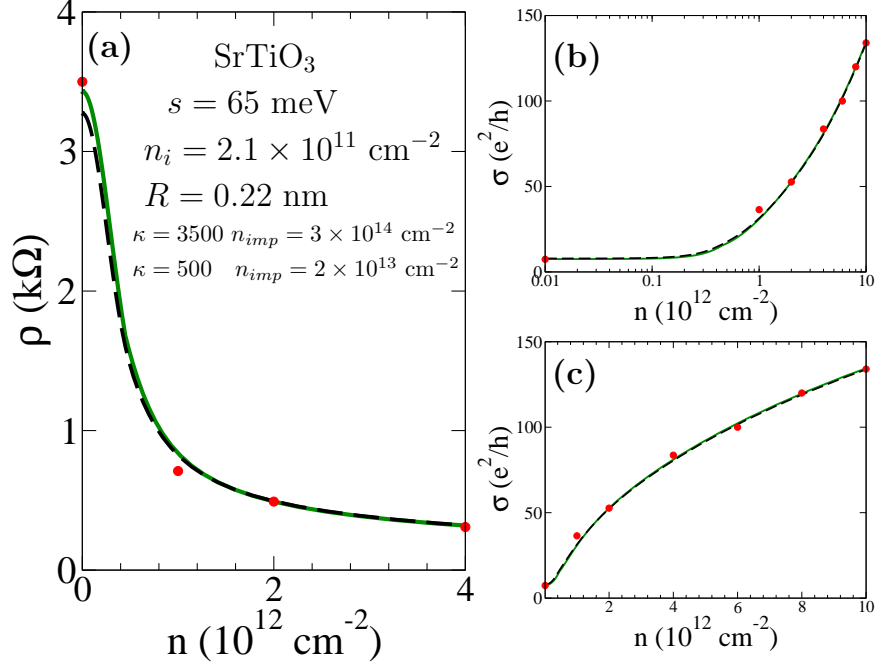
Figure 4.3: Fits to the experimental data of graphene on $SrTiO_3$ (Fig. 2 of Ref. [88]) including Coulomb impurity n_{imp} and resonant impurity n_i. (a) Resistance ρ as a function of carrier density n. (b) Conductance σ as a function of n (in semi-logarithmic scale). (c) Conductance σ as a function of n (in linear scale). The solid (dashed) line is for the temperature $T = 0.25$ (50) K, $\kappa = 3500$ (500) and $n_{imp} = 3 \times 10^{14}$ (2×10^{13} cm^{-2}). Note that we use the theory presented in Ref. [40], s denotes the potential fluctuation associated with the puddles induced by Coulomb disorder [19, 22, 51, 53], the average distance of the charged impurity from the graphene sheet used in (a), (b) and (c) is $d = 1$ Å and the range of the resonant scattering defects $R = 0.22$ nm. Solid (red) dots represent the experimental data extracted from Ref. [88].

4.1 Theoretical formalism

In this section, we first discuss the effects of various scattering mechanisms on the electronic transport of graphene. We will analyze four different sources of disorder covering the various realistic possibilities for resistive disorder scattering in graphene (a) randomly distributed long-range screened Coulomb impurity[1, 16, 20, 24], (b) short-range point defects[1], (c) resonant disorder[89, 18], and (d) correlated long-range Coulomb impurity[44, 45] in the following. The inverse of the total scattering time $1/\tau_{tot}$ is the sum of different inverse scattering times due to various scattering mechanisms at low temperatures. We further discuss three different models leading to the sub-linear behavior of $\sigma(n)$ of graphene on various substrates: (1) the standard model including randomly distributed Coulomb impurities and short-range scattering mechanism; (2) the resonant scattering mechanism; (3) the recently proposed correlated charged impurity model[44, 45]. We note that at densities above the puddle-dominated density regime, the conductivity is strictly linear in carrier density for scattering by long-range Coulomb disorder.

First, the scattering time due to randomly distributed charged impurity, denoted as τ_{imp}, is given by[1],

$$\frac{\hbar}{\tau_{imp}(\epsilon_{p\mathbf{k}})} = 2\pi n_{imp} \int \frac{d^2 k'}{(2\pi)^2} \left| \frac{v_i(q)}{\varepsilon(q)} \right|^2 g(\theta_{\mathbf{k}\mathbf{k}'})$$

$$\times \left[1 - \cos \theta_{\mathbf{k}\mathbf{k}'} \right] \delta(\epsilon_{p\mathbf{k}'} - \epsilon_{p\mathbf{k}}) \qquad (4.1)$$

where $\epsilon_{p\mathbf{k}} = p\hbar v_F k$ is the energy of non-interacting Dirac fermion with the Fermi velocity v_F for the pseudospin state "p" and 2D wave vector $\mathbf{k}$, $\theta_{\mathbf{k}\mathbf{k}'}$ is the scattering angle between in- and out- wave vectors $\mathbf{k}$ and $\mathbf{k}'$, $\mathbf{q} = \mathbf{k} - \mathbf{k}'$, $g(\theta_{\mathbf{k}\mathbf{k}'}) = \left[1 + \cos \theta_{\mathbf{k}\mathbf{k}'} \right] /2$

is a wave function form factor associated with the chiral matrix of monolayer graphene (and is determined by its band dispersion relation). n_{imp} is the 2D density of the randomly distributed screened Coulomb impurity[14]. $v_i(q) = 2\pi e^2/(\kappa q)$ is the Fourier transform of the two-dimensional (2D) Coulomb potential in an effective background dielectric constant κ, $\varepsilon(q)$ is the static dielectric function of graphene within random-phase approximation (RPA)[17]. This long-range Coulomb disorder leads to the linear density dependent conductivity at low temperatures, [1].

$$\sigma_{imp} = \frac{e^2}{h} \frac{n}{2n_{imp}r_s^2 G_1(r_s)} \qquad (4.2)$$

where $r_s = e^2/(\hbar v_F \kappa)$ is graphene fine structure constant and $G_1(x) = \frac{\pi}{4} + 6x - 6\pi x^2 + 4x(6x^2-1)g(x)$ with $g(x) = \mathrm{sech}^{-1}(2x)/\sqrt{1-4x^2}$ for $x < \frac{1}{2}$ and $\sec^{-1}(2x)/\sqrt{4x^2-1}$ for $x > \frac{1}{2}$.

We then provide the short-range disorder scattering time τ_{sd}, given by[1]

$$\frac{\hbar}{\tau_{sd}(\epsilon_\mathbf{k})} = \frac{k}{4\hbar v_F} n_{sd} V_0^2 \qquad (4.3)$$

where n_{sd} is the 2D short-range impurity density and V_0 is a constant short-range (i.e. a δ-function in real space) potential strength. The conductivity at low temperature induced by this short-range impurity has the following form,

$$\sigma_{sd} = \frac{8e^2}{h} \frac{(\hbar v_F)^2}{n_{sd} V_0^2} \qquad (4.4)$$

which is independent of carrier density ($\sigma(n) \sim$ constant).

The scattering time due to resonant defects τ_i has been shown to have the following form[89, 18]

$$\frac{1}{\tau_i(\epsilon_\mathbf{k})} = \frac{\pi^2 v_F n_i}{k(\ln kR)^2} \qquad (4.5)$$

73

where n_i is the concentration of the resonant defects and R is the potential range of the resonant scattering defects. The logarithmic term in the scattering time of resonant defects gives rise to the sublinear density dependent conductivity[89, 18],

$$\sigma_i = \frac{2e^2}{\pi h} \frac{n}{n_i} \ln^2(\sqrt{n\pi R^2}) \qquad (4.6)$$

We now turn to the discussion of the scattering time due to the spatially correlated charged impurity τ_c is given by[44, 45]

$$
\begin{aligned}
\frac{\hbar}{\tau_c(\epsilon_{p\mathbf{k}})} &= 2\pi n_{imp} \int \frac{d^2 k'}{(2\pi)^2} \left| \frac{v_i(q)}{\varepsilon(q)} \right|^2 S(q) \\
&\times \ g(\theta_{\mathbf{kk'}})\left[1 - \cos\theta_{\mathbf{kk'}}\right]\delta(\epsilon_{p\mathbf{k'}} - \epsilon_{p\mathbf{k}})
\end{aligned}
\qquad (4.7)
$$

where $S(q) = 1 - 2\pi n_{imp}\dfrac{r_0}{q}J_1(qr_0)$ is the structure factor using the simple continuum analytic model[44, 45], $J_1(x)$ is the Bessel function of the first kind and the correlation effects is defined by the length scale $r_0 < r_i \equiv (\pi n_{imp})^{-1/2}$, the so-called correlation length. The asymptotic form of conductivity at low "k_F" arising from correlated long-range Coulomb disorder is found to be[44, 45],

$$\sigma_c = \frac{e^2}{h} \frac{n}{2n_{imp}r_s^2 G_1(r_s)} \frac{1}{1 - a + Ba^2 n/n_{imp}} \qquad (4.8)$$

where $a = \pi n_{imp} r_0^2$ and $B = G_2(r_s)/[2G_1(r_s)]$ with $G_2(y) = \frac{\pi}{16} - \frac{4y}{3} + 3\pi y^2 + 40y^3[1 - \pi y + \frac{4}{5}(5y^2 - 1)]g(y)$. The correlated Coulomb disorder also leads to a sub-linear density-dependent conductivity, which was adopted to explain the enhancement of both sublinearity of $\sigma(n)$ and mobility reported in Ref. [90].

Comparing different scattering mechanisms discussed above, it is obvious that the long-range Coulomb disorder dominates $\sigma(n)$ at low carrier density since the corresponding scattering rate is asymptotically the largest in the vanishing density
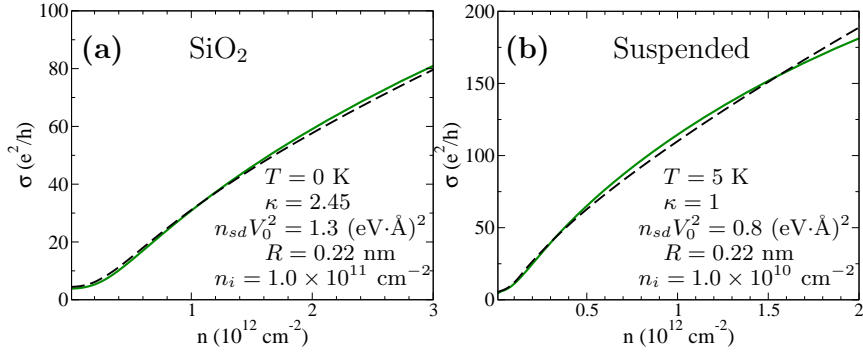
Figure 4.4: Theoretical fits to $\sigma(n)$ for graphene on other substrates. The solid line is the fit including Coulomb impurity n_{imp} and short-range point defect $n_{sd}V_0^2$. The dashed line is the fit including Coulomb impurity n_{imp} and resonant impurity n_i. (a) Fits to the $\sigma(n)$ data for graphene on SiO_2 (Fig. 2 of Ref. [78]). The potential fluctuation $s = 55$ meV, the effective dielectric constant $\kappa = 2.45$, and the average distance of the charged impurity from the graphene sheet is $d = 1$ Å. (b) Fits to the $\sigma(n)$ data of suspended graphene (Fig. 3(c) of Ref. [11]). The potential fluctuation $s = 10$ meV, the temperature $T = 5$ K, the dielectric constant $\kappa = 1.0$, and the average distance of the charged impurity from the graphene sheet is $d = 1$ Å.

limit, implying that as the density decreases, only Coulomb disorder would matter near the Dirac point. The long-range Coulomb disorder is also essential in order to explain the electron-hole puddle induced low-density minimum conductivity[1]. In addition to the resonant and correlated long-range Coulomb scattering, we note that a standard model involving both long-range ($\sigma(n) \sim n$) and short-range scatterers can explain the sublinearity of $\sigma(n)$ at higher carrier density, which has successfully explain the conductivity of graphene on boron nitride substrates[87]. We argue that the sample dependent $\sigma(n)$ at high carrier density may well arise from the competition between different scattering mechanisms.

4.2 Numerical results

In this section, we show our theoretical fits to some representative $\sigma(n)$ data for graphene on four different substrates. The analytical formula for $\sigma(n)$ shown in the last section are calculated for homogeneous systems. To capture the inhomogeneous nature of the graphene landscape close to the charge neutrality point (CNP), we assume a Gaussian form of potential fluctuation, parametrized by "s" and apply the effective medium theory of conductance with binary mixture of component, i.e., electron-hole puddles, the details of which have been given in Ref. [40]. The minimum conductivity plateau of the puddle dominated regime in graphene around the charge neutrality point is just well-captured in our theory.

In Fig. 4.3, we show our best theoretical fits to graphene transport data of Ref. [88], using a dual scattering models: the new theory of long-range Coulomb disorder and the resonant scattering defects, which give $\sigma(n) \sim n\ln^2(\sqrt{n\pi R^2})$. The Coulomb disorder theory of transport follows Ref. [40] and includes the effect of Coulomb disorder-induced electron-hole puddles through the potential fluctuation parameter "s". The new model explains the conductivity of graphene on $SrTiO_3$ in the whole range of carrier density. Couto *et al.* in Ref. [88] pointed out that at fixed value of external gate voltage, the carrier density n and the dielectric constant of $SrTiO_3$ substrate would increase by approximately one order of magnitude as the temperature is lowered from 50 K down to 250 mK, which may also lead to the temperature-dependent charged impurity density. Resonant scattering may account for the conductivity of graphene on $SrTiO_3$ away from the Dirac point. Note, how-

ever, that Coulomb disorder induced electron-hole puddles, which give rise to the existence of minimum conductivity, dominate the transport properties of graphene on $SrTiO_3$ close to the Dirac point and thus some charged impurity scattering must be present in the samples of Ref. [88].

In Fig. 4.4, we present the comparison of the $\sigma(n)$ results between the standard model and the new model for graphene on SiO_2 substrate [78] and the suspended graphene[67, 11]. Both models can fit the experimental data very well. Fig. 4.4 shows that the above mentioned two distinct dual scattering models are equally successful in describing the experimental data for both SiO_2-based and suspended graphene, and there is no particular reason, within the transport data fitting scheme without additional information, to preferably choose one model over the other. We mention that the parameters of the models (n_{imp}, $n_{sd}V_0^2$ in the standard model and n_{imp}, n_i in the new model) are not absolutely unique, and it is possible to get equivalent fits by adjusting the parameter sets somewhat. This is expected because $\sigma(n)$ is a smooth function at higher density and somewhat different parameter sets for disorder cannot be distinguished since the models have only qualitative and semi-quantitative predictive power. We emphasize, however, that the resonant scattering model by itself cannot explain the minimum conductivity phenomenon around the charge neutrality point in graphene, existing all the way to the room temperature and above, which is a generic observation for graphene on all substrates.

In Fig. 4.5(a), we compare the theoretical fits between the new model and the correlated disorder model proposed in Ref. [44, 45] for suspended graphene. Because the annealing procedure is routinely used in preparing suspended graphene
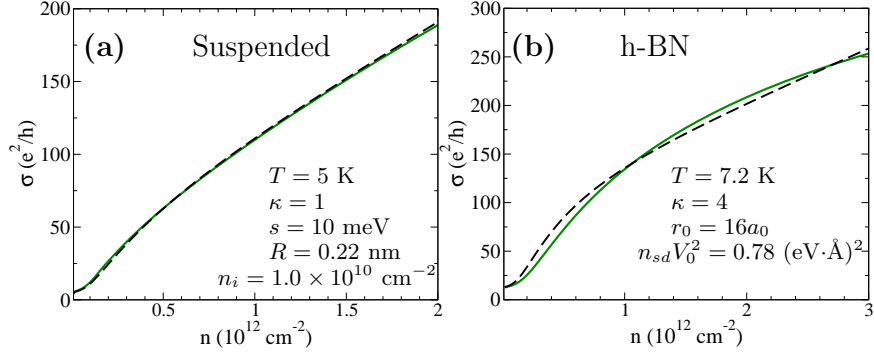
Figure 4.5: (a) Fits to the $\sigma(n)$ data of suspended graphene (Fig. 3(c) of Ref. [11]). The solid line is the fit including the Coulomb impurity $n_{imp} = 0.15 \times 10^{10}$ cm^{-2} and resonant scattering n_i. The dashed line is the fit including correlated Coulomb impurity $n_{imp} = 1.6 \times 10^{10}$ cm^{-2} and correlation length $r_0 = 60a_0$ with $a_0 = 4.92$ Å. (b) Fits to the $\sigma(n)$ data for graphene on boron nitride (Fig. 3(a) of Ref. [85]). The solid line is the fit including Coulomb impurity $n_{imp} = 1.4 \times 10^{11}$ cm^{-2} and short-range point defect $n_{sd}V_0^2$, the potential fluctuation $s = 44$ meV. The dashed line is the fit including correlated Coulomb impurity $n_{imp} = 3.7 \times 10^{11}$ cm^{-2}, and the potential fluctuation $s = 38$ meV. Note that the average distance of the charged impurity from the graphene sheet used in (a) and (b) is $d = 0$ Å.

samples, it is very likely to introduce some spatial correlation among the Coulomb impurities. In Fig. 4.5(b), we compare the standard model with the correlated disorder model for graphene on hexagonal boron nitride (h-BN) substrate. Graphene on boron nitride may also induce some inter-impurity correlations imposed by the similarity between boron nitride and graphene lattice structure. We know, from Fig. 4.5, all of these three models can give reasonable fits to the experimental data of the density-dependent conductivity. They capture the experimentally observed strong-nonlinearity in the density-dependent conductivity $\sigma(n)$. The long-range Coulomb impurity leads to the density inhomogeneity in the graphene system, which is essential in explaining the conductivity plateau close to the Dirac point.

4.3 Discussion

We argue that the resonant scattering theory with $\sigma \sim \frac{n}{n_i} \ln^2(\sqrt{n/n_0})$ predicts a vanishing of graphene conductivity as the carrier density approaches the Dirac point ($n = 0$) which is not observed in the experiments of Ref. [88], where $\sigma(n)$ becomes an approximate constant at low density around the Dirac point in complete contrast with the resonant scattering predictions and thus, the resonant scattering theory cannot obviously be the complete story underlying the transport mechanisms in Ref. [88]. We emphasize that the high-density behavior of $\sigma(n)$ in graphene is, in general, known [1] to be nonuniversal with different samples on different substrates showing different behaviors [9, 10, 46, 54, 13, 55, 21, 84] arising from the competition among Coulomb disorder, short-range disorder, ripples, and (perhaps even) resonant scattering disorder. It is entirely possible that the transport data of Ref. [88] is best described by a combination of Coulomb disorder and resonant scattering, where the low-density minimum conductivity arises from the Coulomb disorder and the intermediate (sublinear in) density conductivity arises from resonant scattering as shown in Fig.4.3, assuming dual independent scattering by charged impurity and resonant scattering centers. The fact that we get excellent agreement over the whole density range of the experimental data indicates that our dual scattering model is a more reasonable description than the pure resonant scattering model. We have also obtained similar good theoretical fits to the existing graphene data as shown in Fig. 4.4 and 4.5. Thus, the possibility that the resonant scattering mechanism is operational at some level in graphene transport at higher densities on any substrate

79

(not just SrTiO₃) cannot definitively be ruled out as we show by considering several different substrates. What can be stated rather definitively is that the low-density transport must always be dominated in graphene by charged impurity scattering.

Chapter 5

Effect of charged impurity correlations on transport in monolayer and bilayer graphene

The scaling of the conductivity σ as a function of gate-voltage, proportional to the average carrier density n, is invaluable in characterizing the properties of graphene [81]. The functional dependence of $\sigma(n)$ at low temperatures contains information [1, 4] about the nature of disorder in the graphene environment (i.e., quenched charged impurity centers, lattice defects[91], interface roughness [92], ripples[93, 94], resonant scattering centers [89, 95, 96, 18], etc.) giving rise to the dominant scattering mechanism. At finite temperatures electron-phonon scattering contributes to the resistivity [97, 57, 58]. However, in graphene the electron-phonon scattering is very weak and it becomes important only at relatively high temperatures ($\gtrsim 400K$), as evidence also from the fact that around room temperature the temperature dependence of σ appears to be dominated by activation processes [40, 21]. The quantitative weakness of the electron-phonon interaction in graphene gives particular impetus to a thorough understanding of the disorder mechanisms limiting graphene conductivity since this may enable substantial enhancement of room temperature graphene-based device for technological applications. This is in sharp contrast to other high-mobility 2D systems such as GaAs-based devices whose

room-temperature mobility could be orders of magnitude lower than the corresponding low-temperature disorder-limited mobility due to strong carrier scattering by phonons[98]. Therefore, a complete understanding of the disorder mechanisms controlling $\sigma(n)$ in graphene at $T = 0$ is of utmost importance both from a fundamental and a technological prospective.

The experimental study of $\sigma(n)$ in gated graphene goes back to the original discovery of 2D graphene,[81, 8] and is a true landmark in the physics of electronic materials. Essentially, all experimental work on graphene begins with a characterization of $\sigma(n)$ and the mobility, $\mu = \sigma/(ne)$. A great deal is therefore known [81, 8, 9, 10, 11, 12] about the experimental properties of $\sigma(n)$ in graphene. The most important features of the experimentally observed $\sigma(n)$ [7, 8, 9, 10, 11, 12, 13] in monolayer graphene (MLG) are: (1) a non-universal sample-dependent minimum conductivity $\sigma(n \approx 0) \equiv \sigma_{min}$ at the charge neutrality point (CNP) where the average carrier density vanishes; (2) a linearly increasing, $\sigma(n) \propto n$, conductivity with increasing carrier density on both sides of the CNP upto some sample dependent characteristic carrier density; (3) a sublinear $\sigma(n)$ for high carrier density, making it appear that the very high density $\sigma(n)$ may be saturating.

To explain the above features of $\sigma(n)$ a model has been proposed [1, 20, 24, 16, 15, 77] with two distinct scattering mechanisms: the long-range Coulomb disorder due to random background charged impurities and static zero-range (often called "short-range") disorder. The net graphene conductivity with these two scattering sources is then given by $\sigma \equiv \rho^{-1} = (\rho_c + \rho_s)^{-1}$, where ρ_c and ρ_s are resistivities arising respectively from charged impurity and short-range disorder. It has been

shown that [1, 20, 24, 16, 15, 77] $\rho_c \sim 1/n$ and $\rho_s \sim$ constant in graphene, leading to $\sigma(n)$ going as

$$\sigma(n) = \frac{n}{A + Cn},\tag{5.1}$$

where the density independent constants A and C are known [1] as functions of disorder parameters; A, arising from Coulomb disorder, depends on the impurity density (n_i) (and also weakly on their locations in space) and the background dielectric constant (κ) whereas the constant C, arising from the short-range disorder [1, 16], depends on the strength of the white-noise disorder characterizing the zero-range scattering. Eq. (5.1) clearly manifests the observed $\sigma(n)$ behavior of graphene for $n \neq 0$ since $\sigma(n \ll A/C) \sim n$, and $\sigma(n \gg A/C) \sim 1/C$ with $\sigma(n)$ showing sublinear $(C + A/n)^{-1}$ behavior for $n \sim A/C$.

The above-discussed scenario for disorder-limited graphene conductivity, with both long-range and short-range disorder playing important qualitative roles at intermediate $(n_i \lesssim n \leqslant A/C)$ and high $(n > A/C)$ carrier densities respectively, has been experimentally verified by several groups [9, 10, 11, 12, 13]. There have been occasional puzzling conductivity measurements [e.g., Ref. [99, 100] reported in the literature which do not appear to be explained by the standard model of independent dual scattering by long- and short-range disorder playing equivalent roles.

Recently, we propose a novel theoretical model in Ref. [44] that is able to semiquantitatively explain all the major features of $\sigma(n)$ observed experimentally assuming only the presence of charged impurities. The key insight on which the model relies is the fact that in experiments, in which the samples are prepared at

room temperature and are often also current annealed, it is very likely that spatial correlations are present among the charged impurities. In particular this model is able to explain the linear (sublinear) scaling of $\sigma(n)$ in MLG at low (high) n without assuming the presence of short-range scattering centers.

In this work, we theoretically revisit graphene transport properties as a function of carrier density, taking into account possible correlations in the spatial distribution of the Coulomb impurity disorder in the environment. We then extend it to the case of BLG. We find that the presence of spatial-correlations among impurities is able to explain a crossover of the scaling of $\sigma(n)$ from low n to high n in both MLG and BLG, as observed in experiments, and that, because of the spatial correlations, σ depends non-monotonically on the impurity density n_i.

In this chapter, we first present the model and the results for the structure factor $S(\mathbf{q})$ that characterizes the impurity correlations. With the structure factor calculated in Sec. 5.1 we provide the transport theory in Section 5.2 and Section 5.3. We study the density-dependent conductivity $\sigma(n)$ of monolayer graphene in the presence of correlated charged impurities. We calculate $\sigma(n)$ at higher carrier density using the Boltzmann transport theory. We also evaluate $\sigma(n)$ applying both Thomas-Fermi-Dirac theory [22] and effective medium theory [24] to characterize the strong carrier density inhomogeneities close to the charge neutrality point. In Section 5.3, we apply the Boltzmann transport theory and the effective medium theory for correlated disorder to bilayer graphene and discuss the qualitative similarities and the quantitative differences between monolayer and bilayer graphene. We briefly discuss the experimental situation at the end of this chapter.

5.1 Structure factor $S(\mathbf{q})$ of Correlated disorder

In this section we describe the model used to calculate the structure factor $S(\mathbf{q})$ for the charged impurities. We then present results for $S(\mathbf{q})$ obtained using this model via Monte Carlo simulations. The Monte Carlo results are then used to build a simple continuum approximation for $S(\mathbf{q})$, which captures all the features of $S(\mathbf{q})$ that are relevant for the calculation of $\sigma(n)$.

5.1.1 Model for the structure factor $S(\mathbf{q})$

To calculate $S(\mathbf{q})$ we follow the procedure presented in Ref. [101], adapted to the case of a honeycomb structure. The approach was applied to study the effects of impurity scattering in GaAs heterojunctions and successfully explained the experimental observation of high-mobilities (e.g. greater than 10^7 cm^2/(V·s)) in modulation-doped GaAs heterostructures. The possible charged impurity positions on graphene form a triangular lattice specified by $\mathbf{r}_{LM} = \mathbf{a}L + \mathbf{b}M$. The vectors $\mathbf{a} = (1,0)a_0$ and $\mathbf{b} = (\sqrt{3}/2, 1/2)a_0$ defined in the x-y plane, with $a_0 = 4.92$Å, which is two times the graphene lattice constant since the most densely packed phase of impurity atoms (e.g. K as in Ref. [10]) on graphene is likely to be an $m \times m$ phase with $m = 2$ for K [102]. The structure factor, including the Bragg scattering term, is given by the following equation:

$$S(\mathbf{q}) = \frac{1}{N_i}\langle\sum_{i,j} e^{i\mathbf{q}\cdot(\mathbf{r}_i - \mathbf{r}_j)}\rangle \tag{5.2}$$

where $\mathbf{r}_i, \mathbf{r}_j$ are the random positions on the lattice $\mathbf{r}_{LM}$ of the charged impurities and the angle brackets denote averages over disorder realizations. Introducing the

fractional occupation $f \equiv N_i/N$ of the total number of available lattice sites N by the number of charged impurities N_i, and the site occupation factor ϵ_{LM} equal to 1 if site $\mathbf{r}_l$ is occupied or zero if unoccupied, we can rewrite Eq. (5.2) as

$$S(\mathbf{q}) = \frac{1}{f} \sum_{LM} \langle \epsilon_{LM} \epsilon_0 \rangle e^{i\mathbf{q} \cdot \mathbf{r}_{LM}} \qquad (5.3)$$

in which the sum is now over all the available lattice sites (not only the ones occupied by the impurities). By letting $C_{LM} \equiv \langle \epsilon_{LM} \epsilon_0 \rangle / f^2$ we can rewrite Eq. (5.3) as:

$$S(\mathbf{q}) = f \sum_{LM} C_{LM} e^{i\mathbf{q} \cdot \mathbf{r}_{LM}}. \qquad (5.4)$$

We then subtract the Bragg scattering term from this expression considering that it does not contribute to the resistivity obtaining

$$S(\mathbf{q}) = f \sum_{LM} (C_{LM} - 1) e^{i\mathbf{q} \cdot \mathbf{r}_{LM}}. \qquad (5.5)$$

It is straightforward to see that for the totally random case, the structure factor is given by $S(\mathbf{q}) = 1 - f$ and $n_i \simeq 4.8f \times 10^{14} \text{cm}^{-2}$. For the correlated case we assume that two impurities cannot be closer than a given length $r_0 < r_i \equiv (\pi n_i)^{-1/2}$ defined as the correlation length. This model is motivated by the fact that two charged impurities cannot be arbitrarily close to each other because the Coulomb repulsion among the impurities during device growth and there must be a minimum separation between them.

5.1.2   Monte Carlo results for $S(\mathbf{q})$

Using Monte Carlo simulations carried out on a 200×200 triangular lattice with 10^6 averaging runs and periodic boundary conditions we have calculated the
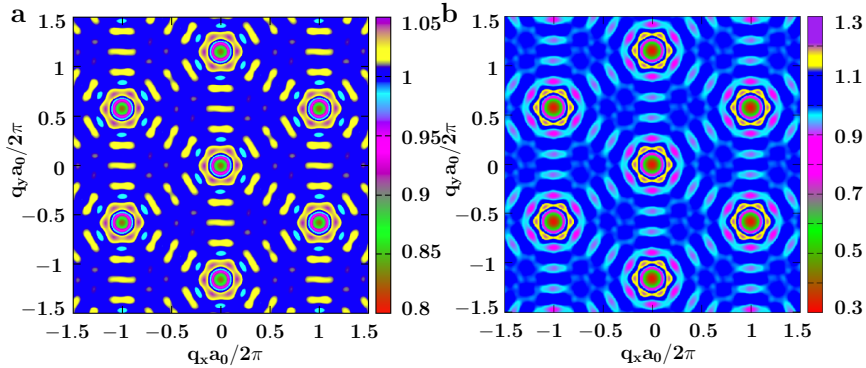
Figure 5.1: (a) Density plot of the structure factor $S(\mathbf{q})$ obtained from Monte Carlo simulations for $a_0 = 4.92$ Å and $r_0 = 5a_0$. (a) $n_i = 0.95 \times 10^{12}$ cm^{-2}; (b) $n_i = 4.8 \times 10^{12}$ cm^{-2}.

structure factor given by Eq. (5.5). In the Monte Carlo calculation a lattice site is chosen randomly and becomes occupied only if it is initially unoccupied and has no nearest neighbors within the correlation length r_0. This process is repeated until the required fractional occupation for a given impurity density is obtained. Once the configuration is generated, the C_{LM} can be numerically determined after doing the ensemble average. In the numerical calculations, we use only statistically significant C_{LM}, i.e., $|\mathbf{r}_{LM} - \mathbf{r}_{00}| \le 3r_0$, since C_{LM} is essential unity for $|\mathbf{r}_{LM} - \mathbf{r}_{00}| > 3r_0$.

In Fig. 5.1, we present a contour plot of the structure factor $S(\mathbf{q})$ obtained from the Monte Carlo simulations for two different values of the impurity density. For $r_0 \ne 0$ the structure factor is suppressed at small momenta. Moreover the suppression of $S(\mathbf{q})$ at small momenta is more pronounced, for fixed r_0, as n_i is increased as can be seen comparing the two panels of Fig. 5.1. The magnitude of $S(\mathbf{q})$ at small $\mathbf{q}$ mostly determines the d.c. conductivity and therefore, from the results of Fig. 5.1, is evident that the presence of spatial correlations among the charged impurities will strongly affect the value of the conductivity.

87

5.1.3 Continuum model for $S(\mathbf{q})$

Given that the value of the d.c. conductivity depends almost entirely on the value of $S(\mathbf{q})$ at small momenta, as discussed in Sections 5.2 and 5.3, it is convenient to introduce a simple continuum model, which is able to reproduce for small $\mathbf{q}$ the structure factor obtained via Monte Carlo simulations. A reasonable continuum approximation to the above discrete lattice model is given by the following pair distribution function $g(\mathbf{r})$ ($\mathbf{r}$ is a 2D vector in the graphene plane),

$$
g(\mathbf{r}) = \begin{cases} 0 & |\mathbf{r}| \le r_0 \\ \\ 1 & |\mathbf{r}| > r_0 \end{cases} .
\tag{5.6}
$$

for the impurity density distribution. In terms of the pair correlation function $g(\mathbf{r})$ the structure factor is given by:

$$
S(\mathbf{q}) = 1 + n_i \int d^2 r\, e^{i\mathbf{q}\cdot\mathbf{r}}[g(\mathbf{r}) - 1]
\tag{5.7}
$$

For uncorrelated random impurity scattering, as in the standard theory, $g(\mathbf{r}) = 1$ always, and $S(\mathbf{q}) \equiv 1$. With Eqs. (5.6) and (5.7), we have

$$
S(q) = 1 - 2\pi n_i \frac{r_0}{q} J_1(q r_0)
\tag{5.8}
$$

where $J_1(x)$ is the Bessel function of the first kind. Fig. 5.2 shows $S(\mathbf{q})$ obtained both via Monte Carlo simulations and by using the simple continuum analytic model [Eq. (5.8)] for a few values of r_0 and n_i. We can see that the continuum model reproduces extremely well the dependence of the structure factor on $\mathbf{q}$ for small momenta, i.e. the region in momentum space that is relevant for the calculation of σ.
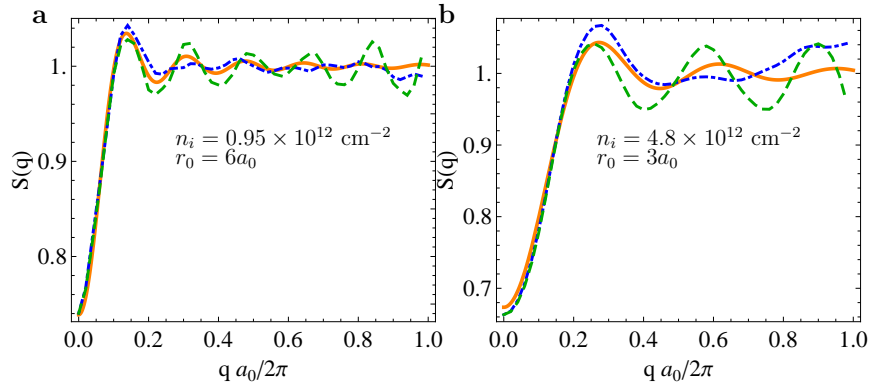
Figure 5.2: (a) and (b) show the calculated structure factor $S(\mathbf{q})$ for two values of impurity density n_i. (a) $n_i = 0.95 \times 10^{12}$ cm^{-2}; (b) $n_i = 4.8 \times 10^{12}$ cm^{-2}. The solid lines show $S(\mathbf{q})$ using Eq. (5.8). Dot-dashed and dashed lines show the Monte Carlo results for two different directions of $\mathbf{q}$ from x-axis, $\theta = 0$ and $\theta = 30°$, respectively.

5.2 Monolayer graphene conductivity

In this section, we explore how the spatial correlations among charged impurities affect monolayer graphene transport properties. To minimize the parameters entering the model we assume the charged impurities to be in a 2D plane placed at an effective distance d from the graphene sheet (and parallel to it).

We first study the density-dependent conductivity in monolayer graphene transport for large carrier densities ($n \gg n_i$) using the Boltzmann transport theory, where the density fluctuations of the system can be ignored. We then discuss $\sigma(n)$ close to the charge neutrality point, where the graphene landscape breaks up into puddles [19, 22, 51, 52, 103, 53] of electrons and holes due to the effect of the charged impurities using the effective medium theory developed in Ref. [24].

5.2.1 High density: Boltzmann transport theory

Using the Boltzmann theory for the carrier conductivity at temperature $T = 0$ we have

$$\sigma = \frac{e^2}{h} \frac{g E_F \tau(E_F)}{2\hbar},$$

(5.9)

where E_F is the Fermi energy, $g = 4$ is the total degeneracy of graphene, and τ is the transport relaxation time at the Fermi energy obtained using the Born approximation. The scattering time at $T = 0$ due to the disorder potential created by charged impurities taking into account the spatial correlations among impurities is given by [17, 40]:

$$
\begin{aligned}
\frac{\hbar}{\tau(\epsilon_{p\mathbf{k}})} &= 2\pi n_i \int \frac{d^2 k'}{(2\pi)^2} \left[\frac{V(|\mathbf{k} - \mathbf{k}'|)}{\varepsilon(|\mathbf{k} - \mathbf{k}'|)} \right]^2 S(\mathbf{k} - \mathbf{k}') \\
&\times \; g(\theta_{\mathbf{k}\mathbf{k}'}) \left[1 - \cos\theta_{\mathbf{k}\mathbf{k}'} \right] \delta(\epsilon_{p\mathbf{k}'} - \epsilon_{p\mathbf{k}})
\end{aligned}
$$

(5.10)

where $V(q) = 2\pi e^2/\kappa q e^{-qd}$ is the Fourier transformation of the 2D Coulomb potential created by a single charged impurity in an effective background dielectric constant κ, $\varepsilon(q)$ is the static dielectric function, $\epsilon_{s\mathbf{k}} = s\hbar v_F k$ is the carrier energy for the pseudospin state "s", v_F is graphene Fermi velocity, $\mathbf{k}$ is the 2D wave vector, $\theta_{\mathbf{k}\mathbf{k}'}$ is the scattering angle between in- and out- wave vectors $\mathbf{k}$ and $\mathbf{k}'$, $g(\theta_{\mathbf{k}\mathbf{k}'}) = \left[1 + \cos\theta_{\mathbf{k}\mathbf{k}'} \right]/2$ is a wave function form-factor associated with the chiral nature of MLG (and is determined by its band structure). The two dimensional static dielectric function $\varepsilon(q)$ is calculated within the random phase approximation

(RPA) [17], and given by

$$\varepsilon(q) = \begin{cases} 1 + \dfrac{4k_F r_s}{q} & \text{if } q < 2k_F \\[2ex] 1 + \dfrac{\pi r_s}{2} & \text{if } q > 2k_F \end{cases} \tag{5.11}$$

After simplifying Eq. 5.10, the relaxation time in the presence of correlated disorder is given by:

$$\frac{\hbar}{\tau} = \left(\frac{\pi n_i \hbar v_F}{4k_F}\right) r_s^2 \int \frac{d\theta\,(1 - \cos^2\theta)}{\left(\sin\frac{\theta}{2} + 2r_s\right)^2} S\!\left(2k_F \sin\frac{\theta}{2}\right), \tag{5.12}$$

where k_F is the Fermi wavevector ($k_F = E_F/(\hbar v_F)$), and r_s is the graphene fine structure constant ($r_s = e^2/(\hbar v_F \kappa) \simeq 0.8$ for graphene on a SiO_2 substrate). For uncorrelated random impurity scattering (i.e., $r_0 = 0$, $g(\mathbf{r}) = 1$, and $S(\mathbf{q}) \equiv 1$) we recover the standard formula for Boltzmann conductivity by screened random charged impurity centers [16, 15, 77], where the conductivity is a linear function of carrier density.

By approximating the structure factor $S(2k_F \sin\theta/2)$ that appears in (5.12) by a Taylor expansion around $k_F \sin\theta/2 = 0$ it is possible to obtain an analytical expression for $\sigma(n)$ that allows us to gain some insight on how the spatial correlation among charged impurities affect the conductivity in MLG. Expanding $J_1(x)$ in Eq. 5.8 around $x \sim 0$ to third order

$$J_1(x) \simeq \frac{x}{2} - \frac{x^3}{16}. \tag{5.13}$$

from Eq. (5.12) we obtain:

$$\frac{\hbar}{\tau} \simeq \frac{4\pi n_i \hbar v_F}{k_F} r_s^2 \left[G_1(r_s)\left(1 - \pi n_i r_0^2\right) + G_2(r_s)\frac{\pi n_i k_F^2 r_0^4}{2} \right], \tag{5.14}$$

91

where the dimensionless functions $G_1(x)$ and $G_2(x)$ are given by, [104]

$$G_1(x) = \frac{\pi}{4} + 6x - 6\pi x^2 + 4x(6x^2 - 1)g_1(x),$$

(5.15)

$$G_2(x) = \frac{\pi}{16} - \frac{4x}{3} + 3\pi x^2 + 40x^3[1 - \pi x + \frac{4}{5}(5x^2 - 1)g_1(x)],$$

where

$$g_1(x) = \begin{cases} \dfrac{\text{sech}^{-1}(2x)}{\sqrt{1-4x^2}} & \text{if } x < \frac{1}{2}, \\ \\ \dfrac{\text{sec}^{-1}(2x)}{\sqrt{4x^2-1}} & \text{if } x > \frac{1}{2}. \end{cases}$$

(5.16)

Using Eq. (5.9), (5.14), and recalling that $k_F = \sqrt{\pi n}$, we find:

$$\sigma(n) = \frac{An}{1 - a + Ba^2 n/n_i},$$

(5.17)

where

$$
\begin{aligned}
A &= \frac{e^2}{h} \frac{1}{2n_i r_s^2 G_1(r_s)} \\
a &= \pi n_i r_0^2 \\
B &= \frac{G_2(r_s)}{2G_1(r_s)}.
\end{aligned}
$$

(5.18)

Note $a < 1$ in our model because the correlation length can not exceed the average impurity distance, i.e., $r_0 < r_i = (\pi n_i)^{-1/2}$. Eq. (5.17) indicates that at low carrier densities the conductivity increases linearly with n at a rate that increases with r_0

$$\sigma(n) \sim \frac{An}{(1-a)};$$

(5.19)

whereas at large carrier densities the dependence of σ on n becomes sublinear:

$$\sigma(n) \sim 1 - \frac{n_c}{n},$$

(5.20)

92

where $n_c = (1-a)n_i/(Ba^2) \sim O(1/n_i r_0^4)$. Note that the above equation is valid for $\sqrt{\pi n} r_0 \ll 1$, where we expand the structure factor as a power series of $\sqrt{\pi n} r_0$. The crossover density n_c, where the sublinearity $(n > n_c)$ manifests itself, increases strongly with decreasing r_0. This generally implies that the higher mobility annealed samples should manifest stronger nonlinearity in $\sigma(n)$, since annealing leads to stronger impurity correlations (and hence larger r_0). This behavior has been observed recently in experiments in which the correlation among charged impurities was controlled via thermal annealing [90]. Contrary to the standard-model with no spatial correlation among charged impurities in which the resistivity increases linearly in n_i, Eq. (5.17) indicates that the resistivity could decrease with increasing impurity density if there are sufficient inter-impurity correlations. This is due to the fact that, for fixed r_0, higher density of impurities are more correlated causing $S(\mathbf{q})$ to be more strongly suppressed at low q as shown in Fig. 5.1 and 5.2. In the extreme case, i.e., $r_0 = a_0$ and $r_i = r_0$, the charged impurity distribution would be strongly correlated, indeed perfectly periodic, and the resistance, neglecting other scattering sources, would be zero. From Eq. (5.17) we find that the resistivity reaches a maximum when the condition

$$r_i/r_0 = \sqrt{2(1 - \pi B n r_0^2)}. \tag{5.21}$$

is satisfied. Equation (5.21) can be used as a guide to improve the mobility of graphene samples in which charged impurities are the dominant source of disorder.

Figs. 5.3(a) and (b) present the results for $\sigma(n)$ obtained integrating numerically the r.h.s. of Eq. (5.12) and keeping the full momentum dependence of the
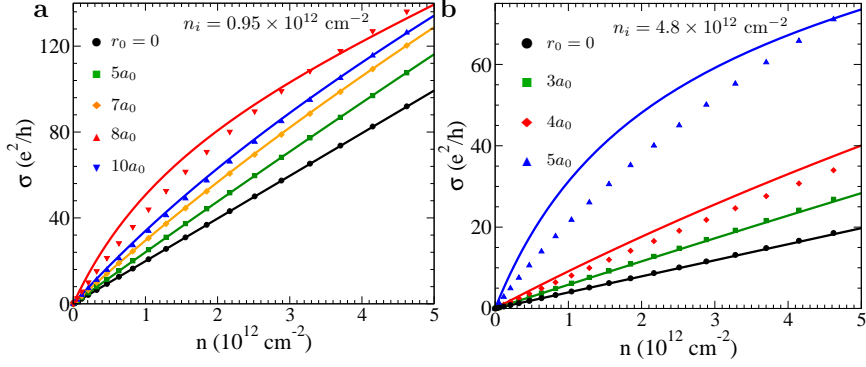
Figure 5.3: Calculated $\sigma(n)$ in monolayer graphene with $S(\mathbf{q})$ obtained from the Monte Carlo simulations, symbols, and $S(\mathbf{q})$ given by Eq. 5.8, solid lines for (a) $n_i = 0.95 \times 10^{12}$ cm^{-2}, and (b) $n_i = 4.8 \times 10^{12}$ cm^{-2}. The different lines correspond to different values of r_0, from top to bottom $r_0 = 10a_0, 8a_0, 7a_0, 5a_0, 0$ in (a) and $r_0 = 5a_0, 4a_0, 3a_0, 0$ in (b).

structure factor. The solid lines show the results obtained using the $S(\mathbf{q})$ given by the continuum model, Eq. (5.8), the symbols show the results obtained using the $S(\mathbf{q})$ obtained via Monte Carlo simulations. The comparison between the two results shows that the analytic continuum correlation model is qualitatively and quantitatively reliable. It is clear that, *for the same value of r_0*, the dirtier (cleaner) system shows stronger nonlinearity (linearity) in a fixed density range consistent with the experimental observations [90] since the correlation effects are stronger for larger values of n_i.

Fig. 5.4(a) presents that the resistivity $\rho = 1/\sigma$ in monolayer graphene as a function of impurity density n_i with correlation length $r_0 = 5a_0$ for different values of carrier density. It is clear that the impurity correlations cause a highly nonlinear resistivity as a function of impurity density and that this nonlinearity in $\rho(n_i)$ is much stronger for lower carrier density. In Fig. 5.4(b) we show the value of the ratio r_i/r_0 for which ρ is maximum as a function of $\sqrt{n}r_0$ The analytical expression
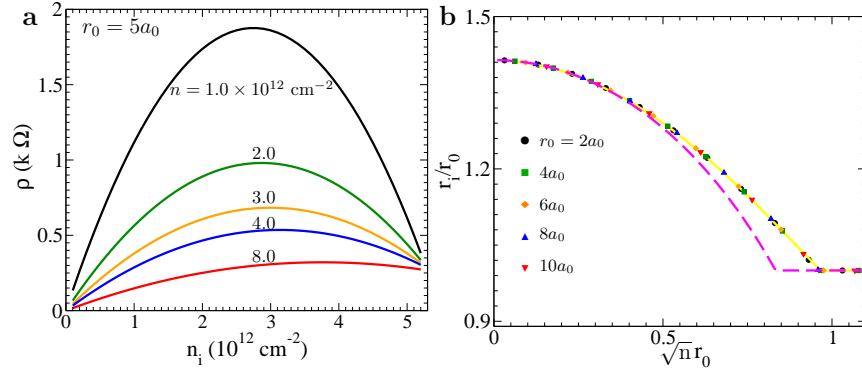
Figure 5.4: (a) Calculated resistivity ρ in monolayer graphene as a function of impurity density n_i for different carrier densities with $r_0 = 5a_0$. (b) The relationship between r_i/r_0 and $\sqrt{n}r_0$ in monolayer graphene, where the conductivity is minimum. The dashed line is obtained using Eq. 5.21.

of Eq. 5.21 is in very good agreement with the result obtained numerically using the full momentum dependence of $S(\mathbf{q})$.

5.2.2   Low density: Effective medium theory

Due to the gapless nature of the band structure, the presence of charged impurities induce strong carrier density inhomogeneities in MLG and BLG. Around the Dirac point, the 2D graphene layer becomes a spatially inhomogeneous semi-metal with electron-hole puddles randomly located in the system. To characterize these inhomogeneities we use the Thomas-Fermi-Dirac (TFD) theory [22]. Ref. [24] has shown that the TFD theory coupled with the Boltzmann transport theory provides an excellent description of the minimum conductivity around the Dirac point with randomly distributed Coulomb impurities. We further improve this technique to calculate the density landscape and the minimum conductivity of monolayer graphene in the presence of correlated charged impurities. To model the disorder, we have assumed that the impurities are placed in a 2D plane at a distance $d = 1$ nm from
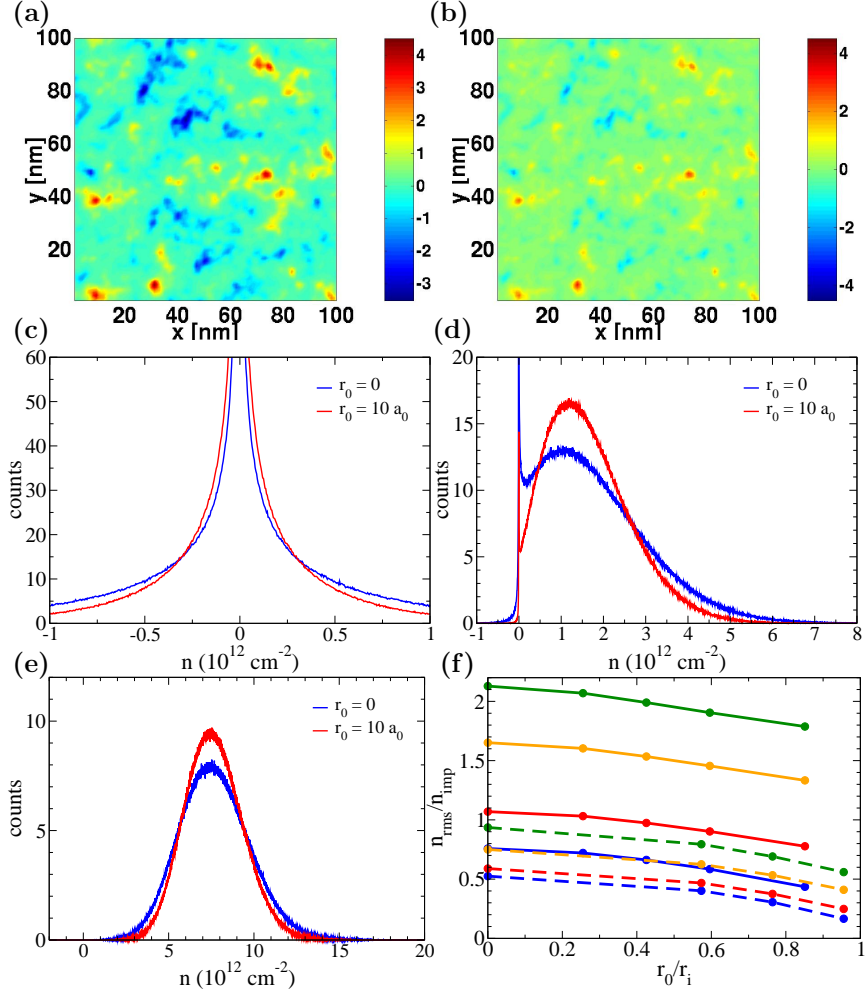
Figure 5.5: The carrier density in monolayer graphene for a single disorder realization obtained from the TFD theory (a) for the uncorrelated case and (b) $r_0 = 10\ a_0$ with $n_i = 0.95 \times 10^{12}$ cm^{-2}. Carrier probability distribution function $P(n)$ are shown in (c), (d), (e) for $\langle n \rangle = 0$, 1.78, 7.7×10^{12} cm^{-2}, respectively. In (f) the ratio n_{rms}/n_i is shown as a function of r_0/r_i for $n_i = 0.95 \times 10^{12}$ cm^{-2}, solid lines, and $n_i = 4.8 \times 10^{12}$ cm^{-2}, dashed lines. We use $\langle n \rangle = 7.7$, 3.14, 0.94, 0×10^{12} cm^{-2} for the solid lines (from top to bottom) and $\langle n \rangle = 8.34$, 4.10, 1.7, 0×10^{12} cm^{-2} for the dashed lines.

the graphene layer. Fig. 5.5(a), (b) show the carrier density profile for a single

disorder realization for the uncorrelated case and correlated case ($r_0 = 10\ a_0$) for

$n_i = 0.95 \times 10^{12}$ cm^{-2}. We can see that in the correlated case the amplitude of

the density fluctuations is much smaller than in the uncorrelated case. The TFD

approach is very efficient and allows the calculation of disorder averaged quantities

such as the density root mean square, n_{rms}, and the density probability distribution

$P(n)$. Figs. 5.5(c), (d), (e) show $P(n)$ at the CNP, and away from the Dirac point

($n_i = 0.95 \times 10^{12}$ cm^{-2}). In each figure both the results for the uncorrelated case

and the one for the correlated case are shown. $P(n)$ for the correlated case is in

general narrower than $P(n)$ for the uncorrelated case resulting in smaller values of

n_{rms} as shown in Fig. 5.5(f) in which n_{rms}/n_i as a function of r_0/r_i is plotted for

different values of the average density, $\langle n \rangle$, and two different values of the impu-

rity density, $n_i = 0.95 \times 10^{12}$ cm^{-2} ("low impurity density") for the solid lines,

and $n_i = 4.8 \times 10^{12}$ cm^{-2} ("high impurity density") for the dashed lines. To de-

scribe the transport properties close to the CNP and take into account the strong

disorder-induced carrier density inhomogeneities we use the effective medium theory

(EMT), where the conductivity is found by solving the following integral equation

[35, 36, 105, 1, 24, 38, 42]:

$$\int dn \frac{\sigma(n) - \sigma_{EMT}}{\sigma(n) + \sigma_{EMT}} P(n) = 0 \tag{5.22}$$

where $\sigma(n)$ is the local Boltzmann conductivity obtained in Section 5.2.1. Fig. 5.6(a)

and (b) show the EMT results for $\sigma(n)$. The EMT results give similar behavior of

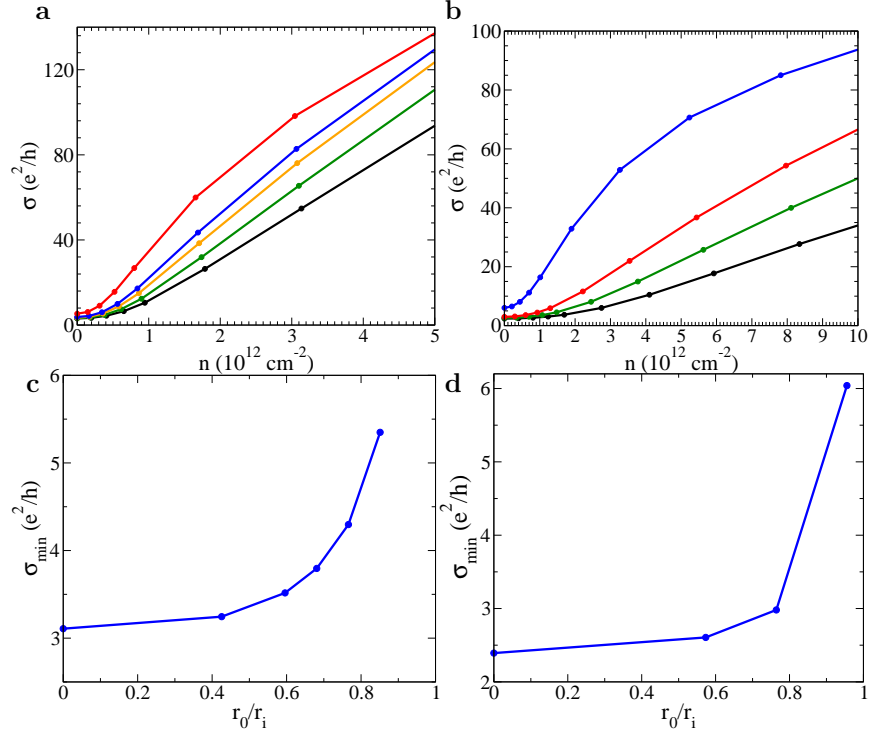$\sigma(n)$ at high carrier density as shown in Fig. 5.3, where the density fluctuations are

Figure 5.6: (a) and (b) show the results for $\sigma(\langle n \rangle)$ in monolayer graphene obtained from the EMT for $n_i = 0.95 \times 10^{12}$ cm^{-2} and $n_i = 4.8 \times 10^{12}$ cm^{-2} respectively. The different lines correspond to different values of r_0, from top to bottom $r_0 = 10a_0, 8a_0, 7a_0, 5a_0, 0$ in (a) and $r_0 = 5a_0, 4a_0, 3a_0, 0$ in (b). (c) and (d) show the value of σ_{min} in monolayer graphene as a function of r_0/r_i.

strongly suppressed. However, close to the Dirac point, the graphene conductivity obtained using TFD-EMT approach is approximately a constant, with this constant minimum conductivity plateau strongly depending on the correlation length r_0. Fig. 5.6(c) and (d) show the dependence of σ_{min} on the size of the correlation length r_0. σ_{min} increases slowly with r_0 for $r_0/r_i < 0.5$, but quite rapidly for $r_0/r_i > 0.5$. The results in Fig. 5.6(c) and (d) are in qualitative agreement with the scaling of σ_{min} with temperature, proportional to r_0, observed in experiments [90].

5.3 Bilayer graphene conductivity

In this section we extend the theory presented in the previous section for monolayer graphene to bilayer graphene. The most important difference between MLG and BLG comes from the fact that, in BLG, at low energies, the band dispersion is approximately parabolic with effective mass $m \simeq 0.033 m_e$ (m_e being the bare electron mass) [106] rather than linear as in MLG. As a consequence in BLG the scaling of the conductivity with doping, at high density, differs from the one in MLG. We restrict ourselves to the case in which no perpendicular electric field is present so that no gap is present between the conduction and the valence band [2, 74, 75, 55, 27].

To characterize the spatial correlation among charged impurities we use the same model that we used for MLG.

5.3.1 High density: Boltzmann transport theory

Within the two-band approximation, the BLG conductivity at zero temperature $T = 0$ is given by:

$$\sigma = \frac{e^2 n \tau}{m} \tag{5.23}$$

where τ is the relaxation time in BLG for the case in which the charged impurities are spatially correlated. τ is given by Eq. 5.10 with $\epsilon_{s\mathbf{k}} = s\hbar^2 k^2/2m$ for the pseudo-spin state "s", $\epsilon(|\mathbf{k} - \mathbf{k}'|)$ the static dielectric screening function of BLG Ref. [71]], and $g(\theta_{\mathbf{kk}'}) = [1 + \cos 2\theta_{\mathbf{kk}'}]/2$ the chiral factor for states on the lowest energy bands of BLG.

The full static dielectric constant of gapless BLG at $T = 0$ is given by [71]

$$\begin{aligned}
\varepsilon(q) &= [1 + V(q)\Pi(q)]^{-1} \\
&= [1 + V(q)D_0 [g_2(q) - f(q)\theta(q - 2k_F)]]^{-1}
\end{aligned} \tag{5.24}$$

where $\Pi(q)$ is the BLG static polarizability, $D_0 = \dfrac{2m}{\pi\hbar^2}$ the density of states, and

$$\begin{aligned}
f(q) &= \frac{2k_F^2 + q^2}{2k_F^2 q}\sqrt{q^2 - 4k_F^2} + \ln\frac{q - \sqrt{q^2 - 4k_F^2}}{q + \sqrt{q^2 - 4k_F^2}} \\
g_2(q) &= \frac{1}{2k_F^2}\sqrt{q^4 + 4k_F^4} - \ln\left[\frac{k_F^2 + \sqrt{k_F^4 + q^4/4}}{2k_F^2}\right]
\end{aligned} \tag{5.25}$$

To make analytical progress, we calculate the density-dependent conductivity using the dielectric function of BLG within the Thomas-Fermi approximation:

$$\varepsilon(q) = 1 + \frac{q_{TF}}{q} \tag{5.26}$$

where $q_{TF} = \dfrac{4me^2}{\kappa\hbar^2} \simeq 1.0 \times 10^9 \text{m}^{-1}$ for bilayer graphene on SiO$_2$ substrate, which is a density independent constant and is larger than $2k_F$ for carrier density $n <$

$8 \times 10^{12} \text{cm}^{-2}$. The relaxation time including correlated disorder is then simplified as:

$$\frac{\hbar}{\tau} = \frac{n_i \pi \hbar^2 q_0^2}{m} \int_0^1 dx \left[\frac{1}{x + q_0} \right]^2 \frac{x^2 (1 - 2x^2)^2}{\sqrt{1 - x^2}} S(2k_F x) \tag{5.27}$$

where $q_0 = q_{TF}/(2k_F)$. To incorporate analytically the correlation effects of charged impurities, we again expand $S(x)$ around $x \sim 0$:

$$S(2k_F x) \simeq 1 - a + \frac{1}{2} \frac{n}{n_i} a^2 x^2 - \frac{1}{12} \frac{n^2}{n_i^2} a^3 x^4 \tag{5.28}$$

Combining Eqs. (5.23), (5.27), and (5.28) we obtain for $\sigma(n)$ at $T = 0$ in the presence of correlated disorder

$$\sigma = \frac{e^2}{h} \frac{2n}{n_i} \frac{1}{\left[(1 - a)G_3[q_0] + \frac{n}{2n_i} a^2 G_4[q_0] - \frac{n^2}{12n_i^2} a^3 G_5[q_0] \right]}, \tag{5.29}$$

where

$$\begin{aligned}
G_3(q_0) &= q_0^2 \int_0^1 \frac{1}{(x + q_0)^2} \frac{x^2 (1 - 2x^2)^2}{\sqrt{1 - x^2}} dx \\
G_4(q_0) &= q_0^2 \int_0^1 \frac{1}{(x + q_0)^2} \frac{x^4 (1 - 2x^2)^2}{\sqrt{1 - x^2}} dx \\
G_5(q_0) &= q_0^2 \int_0^1 \frac{1}{(x + q_0)^2} \frac{x^6 (1 - 2x^2)^2}{\sqrt{1 - x^2}} dx
\end{aligned} \tag{5.30}$$

For each value of r_0 and carrier density n, the resistivity of BLG for correlated disorder is also not a linear function of impurity density, and its behavior is close to that in MLG. The maximum resistivity of BLG is found to be at

$$r_i/r_0 = \sqrt{2(1 - \pi B_B \pi n r_0^2 - C_B \pi^2 n^2 r_0^4)}. \tag{5.31}$$

with $B_B = G_4[q_0]/(2G_3[q_0])$ and $C_B = -G_5[q_0]/(12G_3[q_0])$, which are functions weakly depending on carrier density n.

It is straightforward to calculate the asymptotic density dependence of BLG conductivity from the above formula. We will discuss $\sigma(n)$ in the strong $(q_0 \gg 1)$ and weak $q_0 \ll 1$ screening limits separately.

In the strong screening limit $q_0 \gg 1$, $G_3[q_0] \simeq \pi/8$, $G_4[q_0] \simeq 7\pi/64$ and $G_5[q_0] \simeq 13\pi/128$. For randomly distributed charged impurity, we can express the conductivity as a linear function of carrier density $\sigma(n) \sim n$ [14]. In the presence of correlated charged impurity we find:

$$\sigma(n) = \frac{A_B n}{1 - a + a^2 \dfrac{7n}{16n_i} + a^3 \dfrac{13n^2}{192n_i^2}}, \tag{5.32}$$

where $a = \pi n_i r_0^2$, and $A_B \simeq \dfrac{e^2}{h} \dfrac{16}{\pi n_i}$. In the strong screening limit $q_0 \gg 1 \Rightarrow n \ll n_i$ from (5.32) we obtain $\sigma(n) \sim A_B n/(1-a)$. With the increase of carrier density, the calculated conductivity in BLG also shows the sublinear behavior as in MLG due to the third and fourth terms in the denominator of Eq. 5.32.

In the weak screening limit, $q_0 \ll 1$, we have $G_3[q_0] \simeq \pi q_0^2/4$, $G_4[q_0] \simeq \pi q_0^2/8$ and $G_5[q_0] \simeq 7\pi q_0^2/64$. The conductivity of BLG in the limit $q_0 \ll 1$ is a quadratic function of carrier density for randomly distributed Coulomb disorder:

$$\sigma(n) = \frac{e^2}{h} \frac{32n^2}{n_i q_{TF}^2} \tag{5.33}$$

For the correlated disorder, the calculated conductivity of BLG shows the sub-quadratic behavior:

$$\sigma(n) = \frac{A_b n^2}{1 - a + a^2 \dfrac{n}{4n_i} - a^3 \dfrac{7n^2}{192n_i^2}}, \tag{5.34}$$

with $A_b = \dfrac{e^2}{h} \dfrac{32}{n_i q_{TF}^2}$.

In Figs. 5.7(a) and (b), we show the $\sigma(n)$ within Boltzmann transport theory obtained numerically taking into account the screening via the static dielectric function given by Eq. 5.24. We show the results for several different correlation
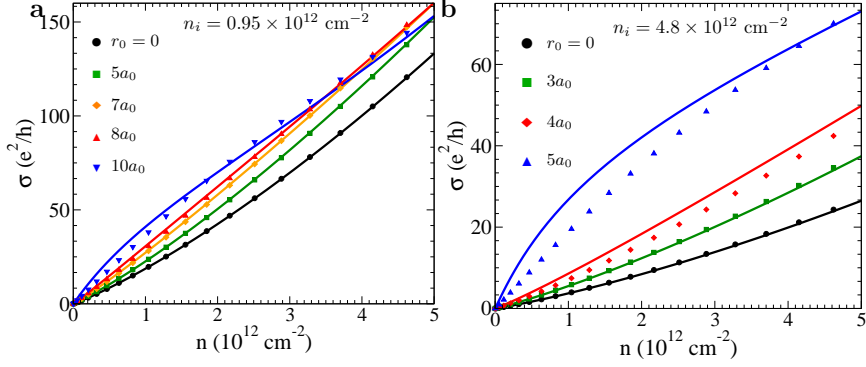
102

Figure 5.7: Calculated $\sigma(n)$ in bilayer graphene with $S(\mathbf{q})$ obtained from the Monte Carlo simulations (symbols) and $S(\mathbf{q})$ given by Eq. (5.8) (solid lines) for two different impurity densities (a) $n_i = 0.95 \times 10^{12}$ cm^{-2} and (b) $n_i = 4.8 \times 10^{12}$ cm^{-2}. The different lines correspond to different values of r_0. In (a) we use $r_0 = 10a_0, 8a_0, 7a_0, 5a_0, 0$ (from top to bottom), and in (b) $r_0 = 5a_0, 4a_0, 3a_0, 0$ (from top to bottom).

lengths r_0 and two different charged impurity densities, (a) $n_i = 0.95 \times 10^{12}$ cm^{-2} and (b) $n_i = 4.8 \times 10^{12}$ cm^{-2}. From Figs. 5.7(a), (b) we see that the conductivity increases with r_0 as in MLG. However the details of the scaling of σ with doping differ between MLG and BLG. In BLG $\sigma(n) \approx n^\alpha$ where $1 < \alpha < 2$ also depends on n. The effect of spatial correlations among impurities in BLG is to increase α at low densities and reduce it at high densities.

In Fig. 5.8(a), we present the resistivity of BLG as a function of impurity density for various carrier density with $r_0 = 5a_0$. The spatial correlation of charged impurity leads to a highly non-linear function of $\rho(n_i)$ as in MLG. We also present the relation between r_i/r_0 and $\sqrt{n}r_0$ where the maximum resistivity of BLG occurs in Fig. 5.8(b). The results are quite close to those of MLG shown in Fig. 5.4.
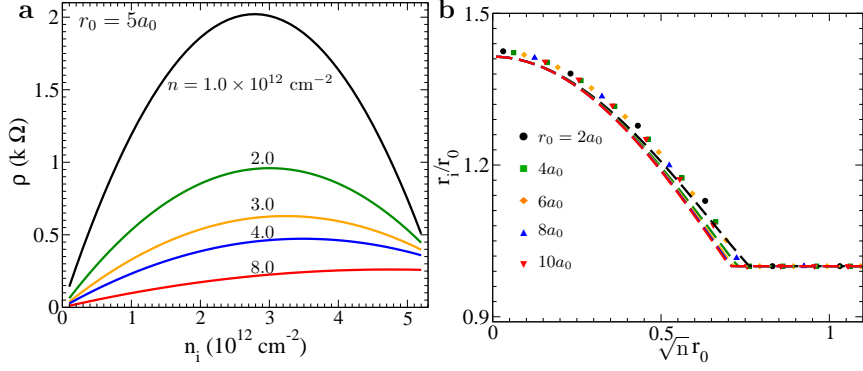
103

Figure 5.8: (a) The resistivity ρ in bilayer graphene is shown as a function of impurity density n_i for different carrier densities with $r_0 = 5a_0$. (b) The relationship between r_i/r_0 and $\sqrt{n}r_0$ in bilayer graphene, where the conductivity is minimum. The dashed lines are obtained using Eq. 5.31.

5.3.2 Low density: Effective medium theory

As in MLG, also in BLG, because of the gapless nature of the dispersion the presence of charged impurities induces large carrier density fluctuations [107, 108, 14, 27] that strongly affect the transport properties of BLG.

Fig. 5.9(a) shows the calculated density landscape for BLG for a single disorder realization, and Fig. 5.9(a) a comparison of the probability distribution function $P(n)$ for BLG and MLG [14]. Within the Thomas-Fermi approximation, approximating the low energy bands as parabolic, in BLG, with no spatial correlation between charged impurities, $P(n)$ is a Gaussian whose root mean square is independent of the doping and is given by the following equation [27]:

$$n_{\mathrm{rms}} = \frac{\sqrt{n_i}}{r_{\mathrm{sc}}} \left[\frac{2}{\pi} f_2(d/r_{\mathrm{sc}}) \right]^{1/2} \tag{5.35}$$

where $f_2(d/r_{\mathrm{sc}}) = e^{2d/r_{\mathrm{sc}}}(1 + 2d/r_{\mathrm{sc}})\Gamma(0, 2d/r_{\mathrm{sc}}) - 1$ is a dimensionless function, $r_{\mathrm{sc}} \equiv [(2e^2 m^*)/(\kappa \hbar^2)]^{-1} \approx 2$ nm is the screening length, and $\Gamma(a, x)$ is the incomplete gamma function. For small d/r_{sc}, $f_2 = -1 - \gamma - \log(2d/r_{\mathrm{sc}}) + O(d/r_{\mathrm{sc}})$ (where $\gamma =$
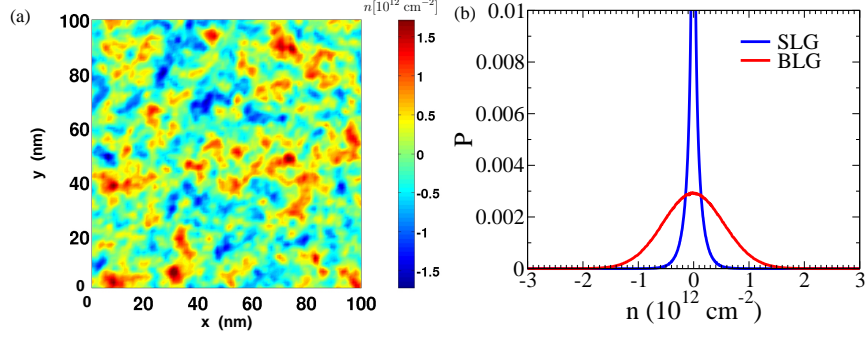
104

Figure 5.9: (a) $n(\mathbf{r})$ of BLG at the CNP for a single disorder realization with $n_i = 10^{11}\text{cm}^{-2}$ and $d = 1$ nm. (b) Disorder averaged $P(n)$, at the CNP for BLG (MLG) red (blue) for $n_i = 10^{11}\text{cm}^{-2}$ and $d = 1$ nm. For MLG $P(n = 0) \approx 0.1$, out of scale. The corresponding n_{rms} is $5.5 \times 10^{11}\text{cm}^{-2}$ for BLG and $1.2 \times 10^{11}\text{cm}^{-2}$ for MLG.

0.577216 is the Euler constant), whereas for $d \gg r_{\text{sc}}$ $f_2 = 1/(2d/r_{\text{sc}})^2 + O((d/r_{\text{sc}})^{-3})$.

As for MLG, also for BLG we find that the presence of spatial correlations among impurities has only a minor quantitative effect on $P(n)$. For this reason, and the fact that with no correlation between the impurities, $P(n)$ has a particularly simple analytical expression, for BLG we neglect the effect of impurity spatial correlations on $P(n)$.

As in MLG the effect of the strong carrier density inhomogeneities on transport can be effectively taken into account using the effective medium theory. Using Eq. (5.22), $\sigma(n)$ given by the Boltzmann theory, and $P(n)$ as described in the previous paragraph, the effective conductivity σ_{EMT} for BLG can be calculated taking into account the presence of strong carrier density fluctuations. Fig. 5.10(a) shows the scaling of σ with doping obtained using the EMT for several values of r_0 and $n_i = 4.8 \times 10^{12}$ cm^{-2}. Taking account of the carrier density inhomogeneities that dominate close to the charge neutrality point, the EMT returns a non-zero value of the conductivity σ_{min} for zero average density, a value that depends on the impurity
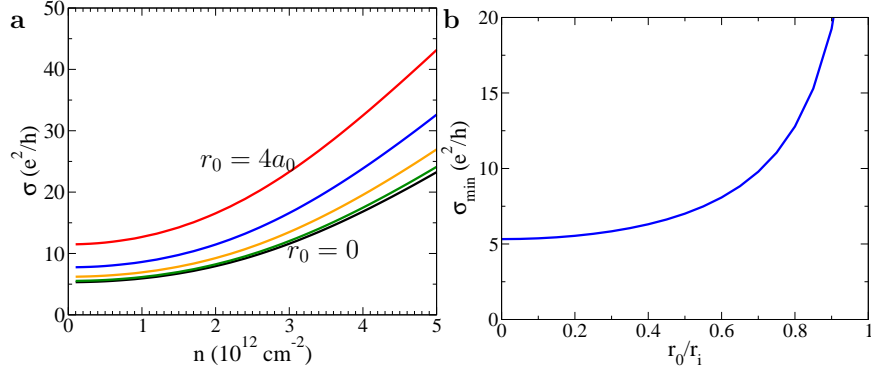
Figure 5.10: (a) BLG conductivity as a function of n obtained using the EMT for $n_i = 4.8 \times 10^{12}$ cm^{-2} for $r_0 = (4, 3, 2, 1, 0) \times a_0$ from top to bottom. (b) BLG $\sigma_{\min}$ as a function of r_0/r_i for $n_i = 4.8 \times 10^{12}$ cm^{-2}.

density and their spatial correlations. In particular, as shown in Fig. 5.10(b), in analogy to the MLG case $\sigma_{\min}$ grows with r_0.

5.4   Discussion of experiments

Although the sublinearity of $\sigma(n)$ can be explained by including both long- and short-range scatterers (or resonant scatterers) in the Boltzmann transport theory [87], it can not explain the observed enhancement of conductivity with increasing annealing temperatures as observed in Ref. [90]. Annealing leads to stronger correlations among the impurities since the impurities can move around to equilibrium sites. Our results show that by increasing r_0, at low densities, both the conductivity and the mobility of MLG and BLG increase. Moreover, our results for MLG [44] show that as r_0 increases the crossover density, at which $\sigma(n)$ from linear becomes sublinear, decreases. All these features have been observed experimentally for MLG [90]. In Ref. [90], Jun et al. studied the influence of thermal annealing on the electronic transport properties of a graphene device with adsorbed potassium atoms.
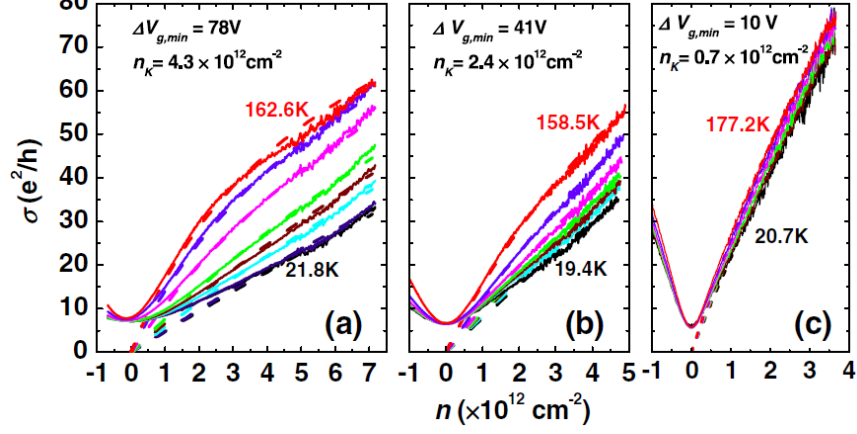
106

Figure 5.11: Carrier-density dependence of graphene conductivity at various anneal-
ing temperatures for three different potassium doping levels. (a) The temperatures
are 21.8, 42.5, 100, 116.5, 130.1, 146.3, 156.6, and 162.6 K. (b) The temperatures
are 19.4, 50.1, 94.9, 112.8, 126.8, 141.9, and 158.5 K. (c) The temperatures are
20.7, 132.7, 141.9, 150.4, 162, and 177.2 K. The lowest and highest temperatures
are indicated in each panel. Adapted from Fig. 2 of Ref. [90].

Fig. 5.11 presents the measured $\sigma(n)$ at different temperatures for three different

potassium doping levels. At all potassium doping levels, σ increases with tem-

perature, more rapidly at higher temperatures $T > 100$ K. In addition to mobility

improvements, $\sigma(n)$ also becomes significantly sublinear at higher annealing temper-

atures, in contrast to the linear $\sigma(n)$ observed for quenched disorder [10]. Fig. 5.11

also showed that the mobility improvement and nonlinearity are most pronounced

for the largest potassium doping. Their experimental data are well described by

Eq. 5.17. Our theory also enables the experimentalists to quantitatively extract the

temperature dependence of the correlation length (see Fig. 5.12).

In addition, our transport theory based on the correlated impurity model also

gives a possible explanation for the observed strong nonlinear $\sigma(n)$ in suspended

graphene [11, 12] where the thermal/current annealing is used routinely. Fig. 5.13

shows the experimentally observed strongly sublinear dependence of the conductivity
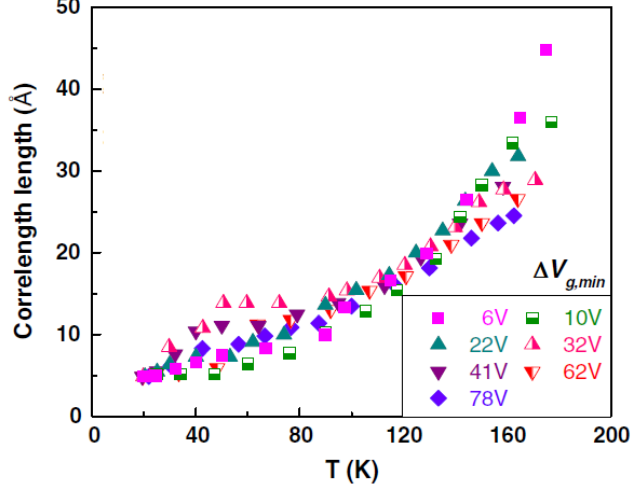
Figure 5.12: Fitting parameters for data in Fig. 5.11 to our correlated disorder theory. The figure shows the correlation length r_0 as a function of annealing temperature for the seven sets of data at different potassium densities reflected in the shift of the minimum conductivity point indicated in the legend. Adapted from Fig. 3 of Ref. [90].

as a function of carrier density in suspended graphene samples[11, 12]. Fig. 5.13(a) and (b) are for suspended monolayer and bilayer graphene samples, respectively.

Although we have used a minimal model for impurity correlations, using a single correlation length parameter r_0, which captures the essential physics of correlated impurity scattering, it should be straightforward to improve the model with more sophisticated correlation models if experimental information on impurity correlations becomes available [90]. Intentional control of spatial charged impurity distributions or by rapid thermal annealing and quenching, should be a powerful tool to further increase mobility in monolayer and bilayer graphene devices[90].
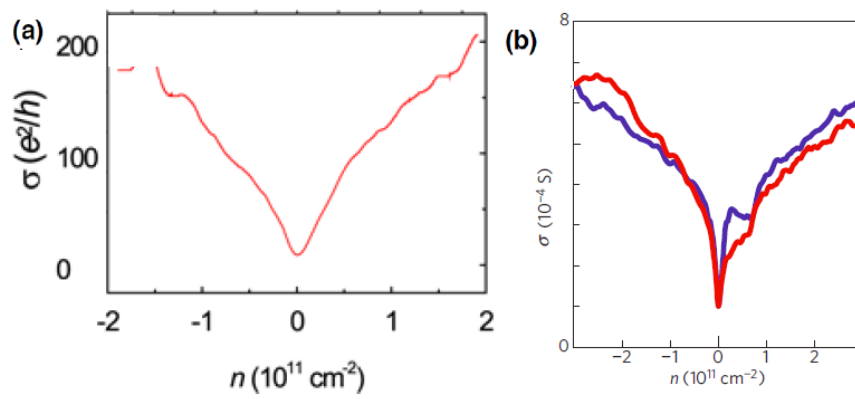
Figure 5.13: (a) Conductivity as a function of carrier density for suspended mono-layer graphene. Adapted from Fig. 3(c) of Ref. [11]. (b) $\sigma(n)$ in suspended bilayer graphene. Adapted from Fig. 1(f) of Ref. [12].

Chapter 6

Conclusion

In this Chapter, we summarize our findings as a conclusion to the dissertation.

In the first Chapter, we discussed the basic physics of carrier transport in graphene. In particular, we considered graphene transport for large carrier densities, where the system is homogeneous. We then discussed the graphene minimum conductivity problem and the physical puddle picture at low carrier densities. We also described a self-consistent theory and TFD-EMT theory to calculate graphene transport properties at low carrier densities.

In Chapter 2, we investigated both MLG and BLG transport in the presence of electron-hole puddles within an analytic statistical theory. Our theory explains the experimentally measured insulating behavior at low temperatures and the consequent nonmonotonic behavior for low mobility samples [21, 56, 55]. Reasonable quantitative agreement with the experimental data can be obtained by choosing appropriate disorder parameters in our theory (i.e. potential fluctuation and impurity strength) for different samples. We find that the puddle parameter s, defining typical potential fluctuations, to be around $10 - 80$ meV in typical graphene samples as extracted by fitting our theory to existing experimental transport data near the charge neutrality point. These values of potential fluctuations characteriz-

ing the graphene charge neutrality point are very consistent with direct numerical calculations of graphene electronic structure in the presence of quenched charged impurities[1, 24, 22, 14]. We also relate our current model to earlier theories using the picture of diffusive transport through disorder-induced electron-hole puddles. Finally, we show the similarity and the quantitative difference between MLG and BLG transport in the presence of puddles.

By using the theoretical formalism developed in Chapter 2, we establish that the recently observed intriguing phenomenon [41] of monotonically increasing graphene resistivity with decreasing carrier density in graphene samples of very high purity (with very high mobilities at high carrier densities) most likely arises not from Anderson localization, but from the semiclassical "disorder by order" phenomenon in Chapter 3. This phenomenon arises from the suppression of electron-hole puddles in the system by a near-by screening layer which then induces the system to show its intrinsic Drude behavior of the resistivity being inversely proportional to the carrier density down to much lower carrier densities without being cut off by the puddle-induced (and well-known [20, 1, 22, 70, 40]) "graphene conductivity minimum" mechanism. The qualitative difference between our "disorder by order" mechanism and localization is that in our case, the conductivity is always finite, eventually being cut off by remnant puddles in the system at much lower carrier densities determined by the details of disorder and screening by the second layer whereas in for localization the conductivity is truly zero at $T = 0$. The other qualitative difference is that the predicted temperature dependence of the resistivity at a fixed low carrier density near the Dirac point in our mechanism is a power law

whereas it must be exponential in the case of Anderson localization. The observed temperature and density dependence of the low-density resistivity in Ref. [41] is consistent with our predictions, and hence we believe that Ref. [41] is manifesting the "disorder by order" phenomenon, not Anderson localization. We believe that the experimental temperature range must be much lower than that used $(20 - 100$ K$)$ in Ref. [41] to see any quantum interference induced localization effects since the inelastic phase coherence length is simply too short for localization effects to manifest at higher temperatures. We urge transport experiments in high quality graphene at very low temperatures $(< 1$ K$)$ to discern localization/antilocalization versus semiclassical "disorder by order" puddle effects.

The main point of Chapter 4 is that the understanding of the graphene minimum conductivity phenomenon necessarily requires the inclusion of scattering by random charged impurities in the environment. We emphasize that since $\sigma_r/\sigma_c \sim \ln^2(\sqrt{n/n_0})$, where $\sigma_{r,c}$ are the resonant scattering and Coulomb scattering induced conductivity respectively, Coulomb disorder[1], with $\sigma_c \sim n$, must necessarily dominate graphene resistivity as one approaches the $n \to 0$ charge neutrality point, not just in SrTiO$_3$, but in all systems. The high density graphene transport is in general, however, nonuniversal where many scattering mechanisms may contribute depending on the density range.

In Chapter 5, we provide a novel physically motivated explanation for the observed sublinear scaling of the graphene conductivity with density at high dopings by showing that the inclusion of spatial correlations among the charged impurity locations leads to a significant sublinear density dependence in the conductivity of

MLG in contrast to the strictly linear-in-density graphene conductivity for uncorrelated random charged impurity scattering. We also show that the spatial correlation of charged impurities will also enhance the mobility of BLG. Our theoretical results are confirmed qualitatively by the experimental measurements presented in Ref. [90] in which the spatial correlations among charged impurities were modified via thermal annealing with no change of the impurity density. Our results, combined with the experimental observation of Ref. [90], demonstrate that in monolayer and bilayer graphene samples in which charged impurities are the dominant source of scattering the mobility can be greatly enhanced by thermal/current annealing processes that increase the spatial correlations among the impurities.

We now discuss some open problems as possible extensions of the work in this dissertation. First, we have neglected effects of quantum tunneling through the potential barriers in our analytic theory. It would be desirable to include the tunneling effects at the electron-hole boundaries in our 2-component transport model developed in Chapter 2. Second, in the absence of intervalley scattering, graphene should manifest antilocalization [109, 110] behavior for which there is some experimental evidence in some situations [111, 112]. The presence of intervalley scattering would restore the usual localization behavior [113]. When and how graphene can manifest strong Anderson localization phenomenon is an interesting question for the future. It will also be desirable for the measurements of Ref. [41] to be performed at a very low mK range of temperatures, where the necessary condition for quantum interference to be operational. One can then study the deviations of the experimental data from our semi-classical theory in this low temperature regime so as to learn about

the nature of graphene localization. Finally, we can also consider a more accurate spatial pair distribution function other than a step function. Then, our impurity correlation model can be improved to give a more accurate account of inter-impurity correlation effects on graphene devices.

Appendix A

A self-consistent formulation of graphene density of states in the presence of inhomogeneity

Below we provide a microscopic theory to calculate self-consistently the electronic density of states in the presence of the potential fluctuations caused by random charged impurities located near graphene/substrate interface, which has been applied to two dimensional semiconductor based electron gas systems[114]. This self-consistent approach mainly addresses two problems with the presence of random charged impurities. One is the screening of the long-range Coulomb interactions between the carriers and the charged impurities. The other is the real-space potential fluctuations produced by the random array of charged impurities.

The motivation for this appendix is two-fold: (1) providing a microscopic self-consistent theory of graphene density of states in the presence of puddles; (2) showing that our approximate physically-motivated density of states (Eq. 2.2) is an excellent approximation to the self-consistent density of states.

A.0.1   Monolayer graphene

First, we apply the self-consistent consideration of random charged impurities on the density of states in monolayer graphene.
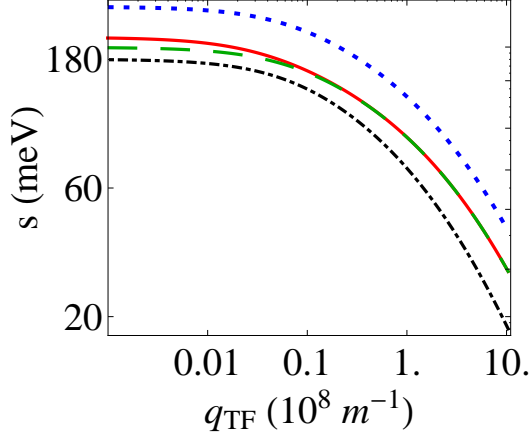
Figure A.1: Standard deviation of potential fluctuation s versus the screening constant q_{TF} (loglog plot) in MLG by varying the Fermi level. The dotted blue line is for $n_{imp} = 1.0 \times 10^{12}$ cm^{-2}, $z_0 = 1$ nm and $d = 100$ nm. The solid red line is for $n_{imp} = 0.5 \times 10^{12}$ cm^{-2}, $z_0 = 1$ nm and $d = 200$ nm. The dashed green line is for $n_{imp} = 0.5 \times 10^{12}$ cm^{-2}, $z_0 = 1$ nm and $d = 100$ nm. The dotdashed black line is for $n_{imp} = 0.5 \times 10^{12}$ cm^{-2}, $z_0 = 2$ nm and $d = 100$ nm.
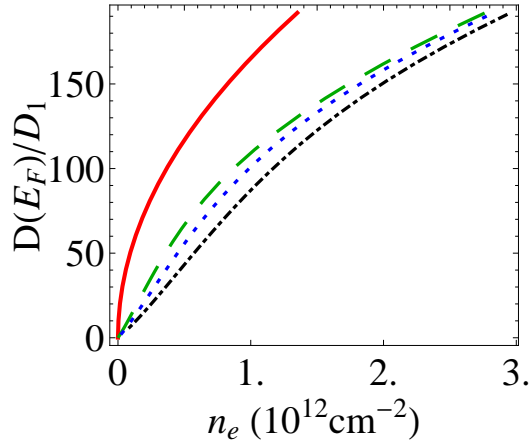

Figure A.2: Calculated the density of states of electron $D_e(E_F)$ in MLG versus electron density using the following parameters: the insulator thickness $d = 100$ nm, the impurity distance from the interface $z_0 = 1$ nm. The solid red line is for unperturbed density of states. The dashed green, dotted blue and dotdashed black lines are corresponding to $n_{imp} = 0.5$, 1.0 and 2.0×10^{12} cm^{-2}, respectively.

116

The simple theory of linear screening gives[114]:

$$q_{TF} = \frac{2\pi e^2}{\kappa} D_e(E_F) \tag{A.1}$$

where q_{TF} is the Thomas-Fermi screening wavevector, $D_e(E_F)$ is the density of states at the Fermi level and κ is the dielectric constant ($\kappa \simeq 2.5$ for graphene on SiO_2 substrate).

The screening constant shown in Eq. A.1 enters Poisson's equation for the potential change $\phi(r, z)$ produced by a charge density ρ_{ext} (associated with the charged impurities in the graphene/substrate environment). For a charge Ze (we use $Z \equiv 1$ in the calculation) located at $r \equiv \sqrt{x^2 + y^2} = 0$ and $z = z_0 > 0$ (on top of the graphene layer), the additional Coulomb potential satisfies:

$$\nabla^2 \phi(r, z) - 2q_{TF} g(z)\phi_0(r) = -\frac{4\pi Ze\delta(x)\delta(y)\delta(z - z_0)}{\kappa_0} \tag{A.2}$$

where $\kappa_0 = \kappa_v = 1.0$ in the vacuum ($z > 0$), $\kappa_0 = \kappa_{ins} = 3.9$ in SiO_2 ($z < 0$) and $\kappa = \frac{\kappa_{ins} + \kappa_v}{2}$. For graphene, $g(z) = \delta(z)$ is the carrier density distribution normal to the interface and $\phi_0(r) = \int \phi(r, z)g(z)dz = \phi(r, 0)$.

To solve Eq. A.2 we take advantage of the cylindrical symmetry to write[115] :

$$\phi(r, z) = \int_0^\infty J_0(k'r)A_{k'}(z)k'dk' \tag{A.3}$$

The potential will satisfy Eq. A.2 if

$$\frac{d^2 A_k}{dz^2} - k^2 A_k - 2q_{TF}A_k(0)g(z) = -\frac{2Ze\delta(z - z_0)}{\kappa_0} \tag{A.4}$$

At the interface $z = 0$, $A_k(z)$ must be continuous and satisfy $\kappa_v(dA_k/dz) - \kappa_{ins}(dA_k/dz) = 2q_{TF}A_k(0)\kappa$. $A_k(z)$ should also satisfies the boundary condition $A_k(z) \to 0$ as

$z \to \infty$. In addition, the impurity potential ϕ will go to zero at the metallic contact below the SiO$_2$ (i.e., $A_k(-d) \equiv 0$ and d is the thickness of the SiO$_2$ layer). Such screening effects are absent in the SiO$_2$. After some algebra, the explicit expression of $A_k(k,0)$ for insulator thickness d and the impurity distance from graphene/substrate interface z_0 is given by:

$$A_k(k,0) = \frac{2e^{-kz_0}Ze\,\sinh(dk)}{k\kappa_{ins}\cosh(dk) + (k\kappa_v + 2q_{TF}\kappa)\sinh(dk)} \tag{A.5}$$

For the thickness of insulator in the limit $d \to \infty$, we have $A_k(k,0) = \dfrac{e^{-kz_0}Ze}{(k + q_{TF})\kappa}$, which has been given in the Appendix B of Ref. [115]. The potential fluctuations with an array of point charges at random positions in the plane $z = z_0$ have a mean-square variation about the average potential [114]:

$$V_{rms}^2 = 2\pi n_{imp}e^2 \int [A_k(0)]^2 k\,dk \tag{A.6}$$

To obtain specific results for the electronic density of states and the screening constant we use the simple Gaussian broadening approximation for the density of states[60]. The disorder-induced potential energy fluctuations is described by $P(V) = \frac{1}{\sqrt{2\pi s^2}}\exp(-V^2/2s^2)$ (Eq. A.6). Then the density of states becomes

$$D_e(E) = \int_{-\infty}^{E} \frac{g_s g_v (E - V)}{2\pi(\hbar v_F)^2} P(V)dV \tag{A.7}$$

$$= D_1 \Big[\frac{E}{2}\mathrm{erfc}\Big(-\frac{E}{\sqrt{2}s}\Big) + \frac{s}{\sqrt{2\pi}}\exp\Big(-\frac{E^2}{2s^2}\Big) \Big]$$

where $\mathrm{erfc}(x)$ is the complementary error function, $s = V_{rms}$, $D_1 = \dfrac{g_s g_v}{2\pi(\hbar v_F)^2}$, v_F is the graphene (Fermi) velocity, $g_s = 2$ and $g_v = 2$ are the spin and valley degeneracies, respectively.
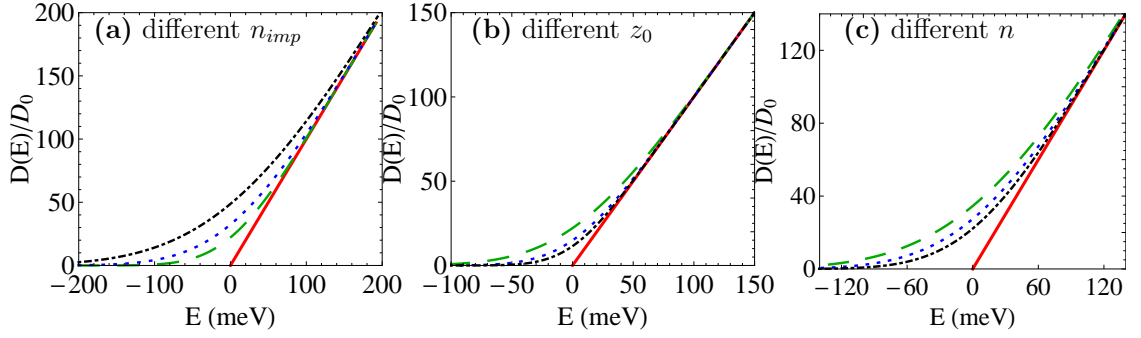
Figure A.3: Calculated density of states of electron $D_e(E)$ of MLG versus energy E for different impurity configurations and carrier densities n. The solid red lines are for the non-interacting MLG system. (a) Calculated $D_e(E)$ in MLG for the insulator thickness $d = 100$ nm, the impurity distance from the interface $z_0 = 1$ nm and carrier density $n = 2.0 \times 10^{12}$ cm^{-2}. The dashed green, dotted blue and dotdashed black lines are corresponding to $n_{imp} = 0.5, 1.0, 2.0 \times 10^{12}$ cm^{-2}, respectively. (b) Calculated $D_e(E)$ in MLG for $d = 100$ nm, $n_{imp} = 0.5 \times 10^{12}$ cm^{-2} and $n = 2.0 \times 10^{12}$ cm^{-2}. The dashed green, dotted blue and dotdashed black lines are corresponding to $z_0 = 1, 2, 3$ nm, respectively. (c) Calculated $D_e(E)$ in MLG for $d = 100$ nm, $z_0 = 1$ nm and $n_{imp} = 0.5 \times 10^{12}$ cm^{-2}. The dashed green, dotted blue and dotdashed black lines are corresponding to $n = 0.5, 1.0, 2.0 \times 10^{12}$ cm^{-2}, respectively.

By choosing the chemical potential E_F as a tuning parameter we have the following coupled equations:

$$q_{TF} = \frac{2\pi e^2}{\kappa} D_e(E_F)$$
$$s^2 = 2\pi n_{imp} e^2 \int [A_k(0)]^2 k dk \tag{A.8}$$

For fixed values of E_F, n_{imp}, d and z_0, we get the self consistent results for s, q_{TF} by solving the above two coupled equations. The electron density could be gotten from the formula:

$$n_e = \int_{-\infty}^{\infty} D_e(\epsilon) f(\epsilon) d\epsilon \tag{A.9}$$

where $f(\epsilon)$ is the Fermi-Dirac distribution function. The electron density in the presence of disorder-induced electron-hole puddles has been discussed in Sec. 2.1, where we use the potential fluctuation s as a fixed parameter. And here we self-consistently solve the parameter s from a microscopic point of view, which is in

119

good agreement with the results shown in Sec. 2.1. The potential fluctuation in Eq. A.6 affects the electronic density of states. But the fluctuations depend on the screening via Eq. A.4 while the screening depends on the density of states via Eq. A.1. Therefore, we have a coupled problem which must be solved self-consistently.

In Fig. A.1, the standard deviation of the potential fluctuation s and the screening constant q_{TF} are plotted for different values of the Fermi level. The self-consistently solved parameters (s, q_{TF}) depend on the fixed charged impurity density n_{imp}, the SiO_2 thickness d, the location of the fixed charged impurity z_0, and the Fermi level E_F (i.e. the carrier density n). All these four effects can be understood from physical intuition. The reduction of the SiO_2 thickness weakens the potential fluctuations when the screening length is small even though there is a little effect for strong screening. As the charged impurities go away from the graphene layer the potential fluctuations is also reduced, while the potential fluctuations becomes stronger with the higher impurity density. Increasing the carrier density n gives rise to the stronger screening effects, and leads to weaker potential fluctuations.

In Fig. A.2, the density of states of monolayer graphene is given with the parameters of SiO_2 thickness $d = 100$ nm and the distance of fixed charged impurities $z_0 = 1$ nm for different impurity densities n_{imp}. In Fig. A.3, we present the electronic density of states for different carrier densities and impurity configurations. The self-consistent calculation of the density of states verifies the results presented in Sec.2.1 as shown in Fig. 2.3, where we choose the potential fluctuation s as an adjustable parameter. For monolayer graphene, the presence of spatially random charged impurities increases the electronic density of states in the whole range of

energy. The corresponding hole density of states can be obtained by changing the sign of energy $D_h(E) = D_e(-E)$.
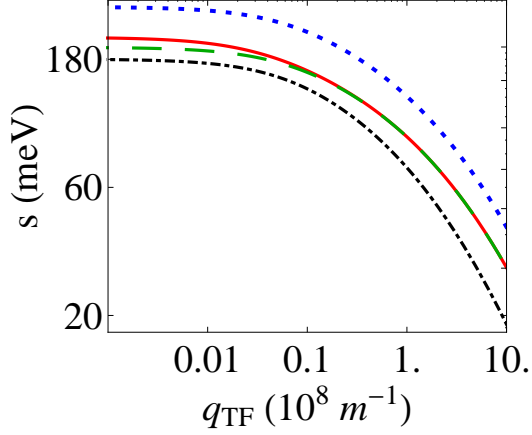
A.0.2 Bilayer graphene

Figure A.4: Standard deviation of potential fluctuation s versus the screening constant q_{TF} (loglog plot) in BLG by varying the Fermi level. The dotted blue line is for $n_{imp} = 1.0 \times 10^{12}$ cm^{-2}, $z_0 = 1$ nm and $d = 100$ nm. The solid red line is for $n_{imp} = 0.5 \times 10^{12}$ cm^{-2}, $z_0 = 1$ nm and $d = 200$ nm. The dashed green line is for $n_{imp} = 0.5 \times 10^{12}$ cm^{-2}, $z_0 = 1$ nm and $d = 100$ nm. The dotdashed black line is for $n_{imp} = 0.5 \times 10^{12}$ cm^{-2}, $z_0 = 2$ nm and $d = 100$ nm.

In this subsection, we provide the density of states in bilayer graphene in the presence of potential fluctuations. As shown for monolayer graphene, we use the linear screening written as[114]:

$$q_{TF} = \frac{2\pi e^2}{\kappa} D_e(E_F) \tag{A.10}$$

where $D_e(E_F)$ is the density of states of BLG at the Fermi level and κ is the dielectric constant and for BLG on SiO$_2$, $\kappa \simeq 2.5$.

Following the same procedure discussed for MLG, the disorder-induced potential fluctuation is described by the Gaussian form $P(V) = \frac{1}{\sqrt{2\pi s^2}}\exp(-V^2/2s^2)$ and
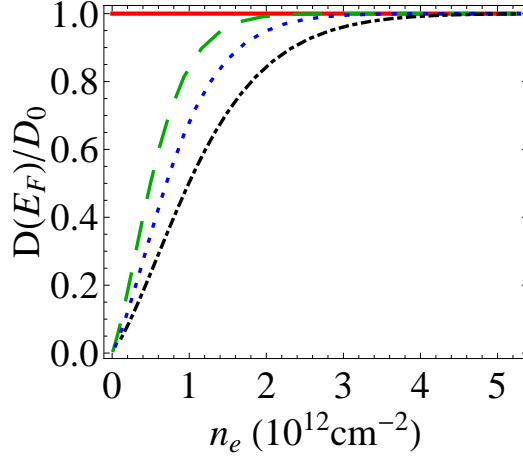
Figure A.5: Calculated density of states of electron $D_e(E_F)$ of BLG versus electron density using the following parameters: the insulator thickness $d = 100$ nm, the impurity distance from the interface $z_0 = 1$ nm. The solid red line is for unperturbed density of states. The dashed green, dotted blue and dotdashed black lines are corresponding to $n_{imp} = 0.5$, 1.0 and 2.0×10^{12} cm^{-2}, respectively.
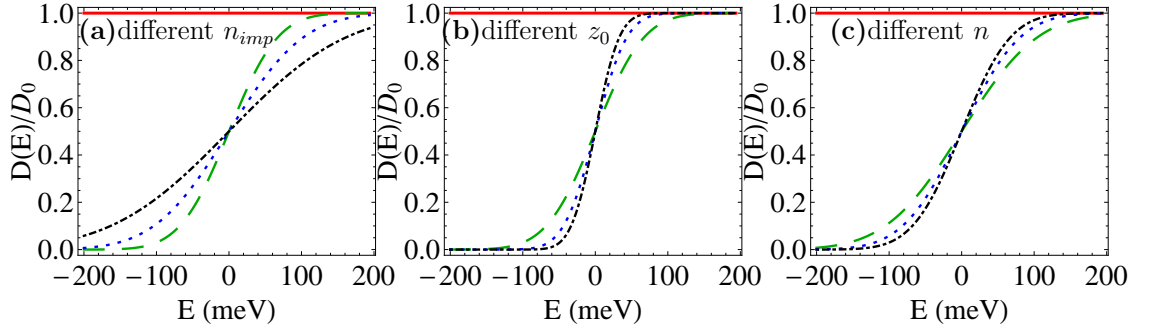

Figure A.6: Calculated density of states of electron $D_e(E)$ of BLG versus energy E for different impurity configuration and carrier densities n. The solid red lines are for the non-interacting BLG system. (a) Calculated $D_e(E)$ in BLG for the insulator thickness $d = 100$ nm, the impurity distance from the interface $z_0 = 1$ nm and carrier density $n = 2.0 \times 10^{12}$ cm^{-2}. The dashed green, dotted blue and dotdashed black lines are corresponding to $n_{imp} = 0.5$, 1.0, 2.0×10^{12} cm^{-2}, respectively. (b) Calculated $D_e(E)$ in BLG for $d = 100$ nm, $n_{imp} = 0.5 \times 10^{12}$ cm^{-2} and $n = 2.0 \times 10^{12}$ cm^{-2}. The dashed green, dotted blue and dotdashed black lines are corresponding to $z_0 = 1$, 2, 3 nm, respectively. (c) Calculated $D_e(E)$ in BLG for $d = 100$ nm, $z_0 = 1$ nm and $n_{imp} = 0.5 \times 10^{12}$ cm^{-2}. The dashed green, dotted blue and dotdashed black lines are corresponding to $n = 0.5$, 1.0, 2.0×10^{12} cm^{-2}, respectively.

the corresponding density of states can be written as (also see Sec. 2.3):

$$D_e(E) = \int_{-\infty}^{E} \frac{g_s g_v m}{2\pi\hbar^2} P(V) dV$$

(A.11)

$$= \frac{D_0}{2} \text{erfc}(-\frac{E}{\sqrt{2}s})$$

where $\text{erfc}(x)$ is the complementary error function, $s = V_{rms}$ (as given in Eq. A.6), $D_0 = \frac{g_s g_v m}{2\pi\hbar^2}$, $g_s = 2$ and $g_v = 2$ are the spin and valley degeneracies, respectively. The main difference between MLG and BLG is in their density of states of non-interacting systems. The homogeneous MLG system has the linear energy-dependent density of states while the density of states of the homogeneous BLG is independent of energy, which leads to different Thomas-Fermi screening wavevectors. The potential fluctuation in Eq. A.6 affects the electronic density of states in BLG. But the fluctuations depend on the screening via Eq. A.4 while the screening depends on the density of states via Eq. A.10. Therefore, we have a coupled problem which must be solved self-consistently.

In Fig. A.4, the broadening parameter s and the screening constant q_{TF} are plotted for various Fermi levels (i.e. the carrier density n). As shown for MLG, the BLG parameters (s, q_{TF}) are also non-trivial function of the fixed charge density n_{imp}, the SiO_2 thickness d, the location of the fixed charged impurity z_0, and the Fermi level. The different charged impurity configurations and carrier densities have similar effects on potential fluctuations of bilayer graphene as we discussed for monolayer graphene. The results for $s(q_{TF})$ are also quite similar to that of MLG (in Fig. A.1) only with small numerical difference.

In Fig. A.5, the self-consistent electronic density of states of BLG has been

calculated using SiO_2 thickness $d = 100$ nm and distance of fixed charged impurities $z_0 = 1$ nm for different impurity densities. The higher impurity density changes the density of states more dramatically. In Fig. A.6, we show the electronic density of states of BLG for different charged impurity configurations and carrier densities. The existence of random charged impurities reduces the electronic density of states for $E > 0$ but creates a band tail for $E < 0$.

Appendix B

The density of states smearing effect on the graphene conductivity

The density of states (DOS) of disordered graphene is calculated within the self-consistent Born approximation (SCBA). In calculating the DOS only a short range disorder potential is considered. The $T = 0$ conductivity is calculated with a simple formula

$$\sigma(n) = \frac{e^2 v_F^2}{2} D(E_F)\tau(E_F), \tag{B.1}$$

where $D(E_F)$ is the DOS at Fermi level, and $\tau(E_F)$ is the transport scattering time. Note that the scattering time is calculated with the DOS of the bare band and with two different disorders, short range potential and long range Coulomb potential. Thus, the scattering time is given by

$$\frac{1}{\tau} = \frac{1}{\tau_C} + \frac{1}{\tau_0}, \tag{B.2}$$

where τ_C (τ_0) is the scattering time due to the long-range Coulomb impurities (short range impurities) and they are given by in the Boltzmann transport approach

$$\frac{1}{\tau_C} \propto D_b(E_F)|V_c(k_F)|^2 \propto E_F^{-1},$$
$$\frac{1}{\tau_0} \propto D_b(E_F)|V_0(k_F)|^2 \propto E_F, \tag{B.3}$$

where $D_b(E) \propto E$ is the DOS of bare band. In low density limit, $E_F \to 0$, the scattering rate by Coulomb impurities dominates and the total scattering time behaves as $\tau(E_F) \propto E_F$, i.e., $\tau(E_F) \propto n^{1/2}$. Thus, even though the DOS is finite at $\omega = 0$ the conductivity, $\sigma(n) \propto D(E_F)\tau(E_F) \propto \sqrt{n}$ as $n \to 0$.

We calculate the disorder-broadened DOS for graphene following Refs. [116, 117, 118], and then calculate the conductivity following Eqs. (B.1)–(B.3) above. Our results for the broadened DOS and the resulting conductivity are shown in Figs. B.1 and B.2. The important points to note are :(1) the disorder-broadened DOS leads to an enhanced (suppressed) conductivity at low (high) carrier densities for more (less) disordered systems in agreement with Ref. [41]; (2) but the Dirac point conductivity is always zero independent of whether the DOS is smeared by disorder or not and thus the smearing of the DOS by itself cannot be the explanation for the existence of the minimum conductivity plateau in graphene which necessitates the existence of electron-hole puddles in the system.

We can consider the DOS of disordered graphene (rather than the DOS of the bare graphene as done above) to calculate the scattering time. Now we have a finite DOS as $E \to 0$. Then with the same approach as Eq. (B.3) we have the scattering times as $E_F \to 0$

$$
\begin{aligned}
\frac{1}{\tau_C} &\propto D(E_F)|V_c(k_F)|^2 \propto E_F^{-2}, \\
\frac{1}{\tau_0} &\propto D(E_F)|V_0(k_F)|^2 \propto E_F^{0}.
\end{aligned}
\tag{B.4}
$$

Similarly we have $\tau \propto E_F^2 \propto n$, and $\sigma(n) \propto n$ as $n \to 0$.

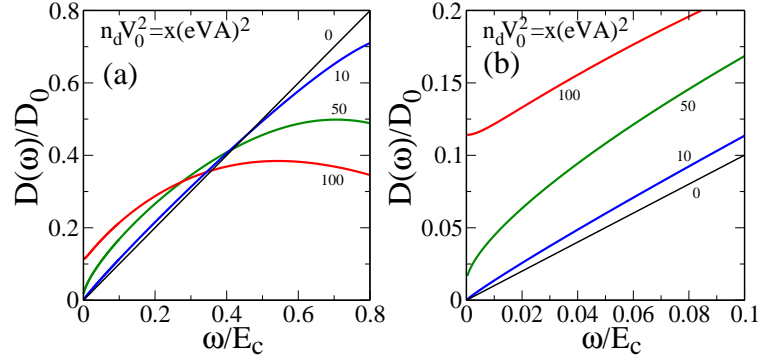Thus, the DOS smearing by disorder always produces zero conductivity at the

Figure B.1: Calculated the density of states within SCBA for different strengths of δ-range disorder potential V_0, $n_d V_0^2 = 0, 10, 50, 100$ $(eV\text{Å})^2$, where n_d is the short range impurity density. Here $E_c = \hbar v_F k_c$ is the cut-off energy with $k_c \sim 1/a$ where $a = 1.42\text{Å}$ is the lattice constant. $D_0 = g_s g_v E_c/(2\pi(\hbar v_F)^2)$. (b) shows the same results of (a) at low energy regime. The DOS at $\omega = 0$ is given by the formula, $D(0)/D_0 = \ln E_0/(2\pi E_0)$, where $E_0 = E_c/\sqrt{e^{2\pi/\gamma} - 1}$ and $\gamma = n_d V_0^2/(2(\hbar v_F)^2)$.

Dirac point ($n = 0$) in graphene although close to the Dirac point the smearing of the DOS does indeed lead to an enhanced conductivity as shown in the figures. Although our results are shown within the SCBA theory of the DOS smearing, the qualitative findings are the same within the simpler Born approximation where the disorder broadening of the DOS does not lead to a finite DOS at zero density. Thus, the DOS smearing by disorder cannot be an explanation for the graphene finite minimum conductivity around the Dirac point which arises from the Coulomb disorder induced density inhomogeneity and electron-hole puddles in the system.
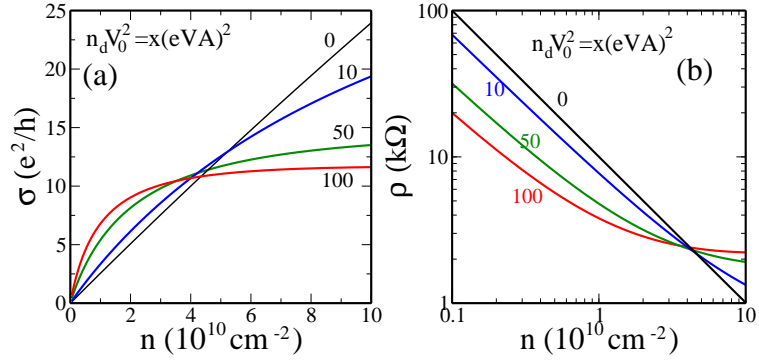
Figure B.2: Calculated conductivity as a function carrier density. Parameters of graphene on h-BN are used. The conductivity is calculated with Eq. B.1, $\sigma = \frac{e^2 v_F^2}{2} D(E_F)\tau(E_F)$, where $D(E_F)$ is the DOS at Fermi level which is given in Fig. B.1, and $\tau(E_F)$ is the transport scattering time calculated with DOS for the bare band. The conductivity is calculated for a fixed long range charged impurity $n_i = 10^{11}$ cm^{-2} , but for different short range disorder potentials as given in the figure. Both the DOS and conductivity are calculated with the same short range disorders. Note that the conductivity approaches zero as the carrier density goes to zero. (b) shows the resistivity $\rho = 1/\sigma$ calculated with the same parameters of (a) as a function carrier density in log-log scale.

List of Publications

This thesis is based on the following publications:

1. Qiuzi Li, E. H. Hwang, and S. Das Sarma, *Disorder-induced temperature-dependent transport in graphene: Puddles, impurities, activation, and diffusion*, Physical Review B **84**, 115442 (2011)

2. S. Das Sarma, E. H. Hwang, and Qiuzi Li, *Disorder by order in graphene*, Physical Review B **85**, 195451 (2012)

3. S. Das Sarma, Qiuzi Li, *Graphene on $SrTiO_3$*, Solid State Communications Fast track communication **152**, 1795 (2012)

4. Qiuzi Li, E. H. Hwang, E. Rossi, and S. Das Sarma, *Theory of 2D transport in graphene for correlated disorder*, Physical Review Letters **107**, 156601 (2011)

5. Qiuzi Li, E. H. Hwang and E. Rossi, *Effect of charged impurity correlation on transport in monolayer and bilayer graphene*, Solid State Communications **152**, 1390 (2012)

Other publications that I contributed to:

6. Dimitrie Culcer, Lukasz Cywinski, Qiuzi Li, Xuedong Hu, and S. Das Sarma, *Realizing singlet-triplet qubits in multivalley Si quantum dots*, Physical Review B **80**, 205302 (2009)

7. Qiuzi Li, Lukasz Cywinski, Dimitrie Culcer, Xuedong Hu, and S. Das Sarma, *Exchange coupling in silicon quantum dots: Theoretical considerations for quantum computation*, Physical Review B **81**, 085313 (2010)

8. Dimitrie Culcer, Lukasz Cywinski, Qiuzi Li, Xuedong Hu, and S. Das Sarma, *Quantum dot spin qubits in Silicon: Multivalley physics*, Physical Review B **82**, 155312 (2010)

9. Qiuzi Li, E. H. Hwang, and S. Das Sarma, *Collective modes of monolayer, bilayer, and multilayer fermionic dipolar liquid*, Physical Review B **82**, 235126 (2010)

10. Qiuzi Li, Parag Ghosh, Jay D. Sau, Sumanta Tewari, and S. Das Sarma, *Anisotropic surface transport in topological insulators in proximity to a helical spin density wave*, Physical Review B **83**, 085110 (2011)

11. Qiuzi Li, E. H. Hwang, and S. Das Sarma, *Temperature-dependent compressibility in graphene and two-dimensional systems*, Physical Review B **84**, 235407 (2011)

12. Dohun Kim, Qiuzi Li, Paul Syers, Nicholas P. Butch, Johnpierre Paglione, S. Das Sarma, Michael S. Fuhrer, *Intrinsic Electron-Phonon Resistivity in Bi_2Se_3 in the Topological Regime*, Physical Review Letters **109**, 166801 (2012)

13. Qiuzi Li, Enrico Rossi, and S. Das Sarma, *Two-dimensional electronic transport on the surface of 3D topological insulators*, Physical Review B, **86**, 235443 (2012)

14. Qiuzi Li and S. Das Sarma, *Finite temperature inelastic mean free path and quasiparticle lifetime in graphene*, Physical Review B **87**, 085406 (2013)

Bibliography

[1] S. Das Sarma, S. Adam, E. H. Hwang, and E. Rossi, Rev. Mod. Phys. **83**, 407 (2011).

[2] E. V. Castro, K. S. Novoselov, S. V. Morozov, N. M. R. Peres, J. M. B. L. Dos Santos, J. Nilsson, F. Guinea, A. K. Geim, and A. H. C. Neto, Phys. Rev. Lett. **99**, 216802 (2007).

[3] A. H. C. Neto, F. Guinea, N. M. R. Peres, K. S. Novoselov, and A. K. Geim, Rev. Mod. Phys. **81**, 109 (2009).

[4] N. M. R. Peres, Rev. Mod. Phys. **82**, 2673 (2010).

[5] M. O. Goerbig, Rev. Mod. Phys. **83**, 1193 (2011).

[6] Y. Lee, S. Bae, H. Jang, S. Jang, S.-E. Zhu, S. H. Sim, Y. I. Song, B. H. Hong, and J.-H. Ahn, Nano Letters **10**, 490 (2010).

[7] K. S. Novoselov, D. Jiang, F. Schedin, T. J. Booth, V. V. Khotkevich, S. V. Morozov, and A. K. Geim, Proc. Natl. Acad. Sci. USA **102**, 10451 (2005).

[8] K. S. Novoselov, A. K. Geim, S. V. Morozov, D. Jiang, M. I. Katsnelson, I. V. Grigorieva, S. V. Dubonos, and A. A. Firsov, Nature **438**, 197 (2005).

[9] Y.-W. Tan, Y. Zhang, K. Bolotin, Y. Zhao, S. Adam, E. H. Hwang, S. Das Sarma, H. L. Stormer, and P. Kim, Phys. Rev. Lett. **99**, 246803 (2007).

[10] J.-H. Chen, C. Jang, S. Adam, M. S. Fuhrer, E. D. Williams, and M. Ishigami, Nature Phys. **4**, 377 (2008).

[11] K. Bolotin, K. Sikes, Z. Jiang, M. Klima, G. Fudenberg, J. Hone, P. Kim, and H. Stormer, Solid State Commun. **146**, 351 (2008).

[12] B. E. Feldman, J. Martin, and A. Yacoby, Nature Phys. **5**, 889 (2009).

[13] X. Hong, K. Zou, and J. Zhu, Phys. Rev. B **80**, 241415 (2009).

[14] S. Das Sarma, E. H. Hwang, and E. Rossi, Phys. Rev. B **81**, 161407 (2010).

[15] T. Ando, J. Phys. Soc. Jpn. **75**, 074716 (2006).

[16] E. H. Hwang, S. Adam, and S. Das Sarma, Phys. Rev. Lett. **98**, 186806 (2007).

[17] E. H. Hwang and S. Das Sarma, Phys. Rev. B **75**, 205418 (2007).

[18] A. Ferreira, J. Viana-Gomes, J. Nilsson, E. R. Mucciolo, N. M. R. Peres, and A. H. Castro Neto, Phys. Rev. B **83**, 165402 (2011).

[19] J. Martin, N. Akerman, G. Ulbricht, T. Lohmann, J. H. Smet, K. von Klitzing, and A. Yacobi, Nature Physics **4**, 144 (2008).

[20] S. Adam, E. H. Hwang, V. M. Galitski, and S. Das Sarma, Proc. Natl. Acad. Sci. USA **104**, 18392 (2007).

[21] J. Heo, H. J. Chung, S.-H. Lee, H. Yang, D. H. Seo, J. K. Shin, U.-I. Chung, S. Seo, E. H. Hwang, and S. Das Sarma, Phys. Rev. B **84**, 035421 (2011).

[22] E. Rossi and S. Das Sarma, Phys. Rev. Lett. **101**, 166803 (2008).

[23] V. W. Brar, Y. Zhang, Y. Yayon, T. Ohta, J. L. McChesney, A. Bostwick, E. Rotenberg, K. Horn, and M. F. Crommie, Appl. Phys. Lett. **91**, 122102 (2007).

[24] E. Rossi, S. Adam, and S. Das Sarma, Phys. Rev. B **79**, 245423 (2009).

[25] L. Brey and H. A. Fertig, Phys. Rev. B **80**, 035406 (2009).

[26] S. Das Sarma and E. H. Hwang, Phys. Rev. Lett. **102**, 206412 (2009).

[27] E. Rossi and S. Das Sarma, Phys. Rev. Lett. **107**, 155502 (2011).

[28] M. M. Fogler, D. S. Novikov, L. I. Glazman, and B. I. Shklovskii, Phys. Rev. B **77**, 075420 (2008).

[29] C. Beenakker, Rev. Mod. Phys. **80**, 1337 (2008).

[30] M. I. Katsnelson, K. S. Novoselov, and A. K. Geim, Nat. Phys. **2**, 620 (2006).

[31] A. V. Shytov, M. S. Rudner, and L. S. Levitov, Phys. Rev. Lett. **101**, 156804 (2008).

[32] N. Stander, B. Huard, and D. Goldhaber-Gordon, Phys. Rev. Lett. **102**, 026807 (2009).

[33] A. Young and P. Kim, Nature Physics **5**, 222 (2009).

[34] E. Rossi, J. H. Bardarson, P. W. Brouwer, and S. Das Sarma, Phys. Rev. B **81**, 121408R (2010).

[35] D. A. G. Bruggeman, Ann. Physik **416**, 636 (1935).

[36] R. Landauer, J. Appl. Phys. **23**, 779 (1952).

[37] M. Hori and F. Yonezawa, J. Math. Phys. **16**, 352 (1975).

[38] M. M. Fogler, Phys. Rev. Lett. **103**, 236801 (2009).

[39] E. Rossi, J. H. Bardarson, M. S. Fuhrer, and S. Das Sarma, Phys. Rev. Lett. **109**, 096801 (2012).

[40] Q. Li, E. H. Hwang, and S. Das Sarma, Phys. Rev. B **84**, 115442 (2011).

[41] L. A. Ponomarenko, A. K. Geim, A. A. Zhukov, R. Jalil, S. V. Morozov, K. S. Novoselov, I. V. Grigorieva, E. H. Hill, V. V. Cheianov, V. I. Fal'ko, K. Watanabe, T. Taniguchi, and R. V. Gorbachev, Nat. Phys. **7**, 958 (2011).

[42] S. Das Sarma, E. H. Hwang, and Q. Li, Phys. Rev. B **85**, 195451 (2012).

[43] S. Das Sarma and Q. Li, Solid State Communications **152**, 1795 (2012).

[44] Q. Li, E. H. Hwang, E. Rossi, and S. Das Sarma, Phys. Rev. Lett. **107**, 156601 (2011).

[45] Q. Li, E. Hwang, and E. Rossi, Solid State Communications **152**, 1390 (2012).

[46] F. Chen, J. Xia, and N. Tao, Nano Letters **9**, 1621 (2009).

[47] Y.-W. Tan, Y. Zhang, H. L. Stormer, and P. Kim, Eur. Phys. J. **148**, 15 (2007).

[48] J. H. Chen, C. Jang, S. Xiao, M. Ishigami, and M. S. Fuhrer, Nature Nanotechnology **3**, 206 (2008).

[49] E. H. Hwang and S. Das Sarma, Phys. Rev. B **79**, 165404 (2009).

[50] M. Lv and S. Wan, Phys. Rev. B **81**, 195409 (2010).

[51] Y. Zhang, V. W. Brar, C. Girit, A. Zettl, and M. F. Crommie, Nat. Phys. **5**, 722 (2009).

[52] A. Deshpande, W. Bao, F. Miao, C. N. Lau, and B. J. LeRoy, Phys. Rev. B **79**, 205411 (2009).

[53] A. Deshpande, W. Bao, Z. Zhao, C. N. Lau, and B. J. LeRoy, Phys. Rev. B **83**, 155409 (2011).

[54] W. Zhu, V. Perebeinos, M. Freitag, and P. Avouris, Phys. Rev. B **80**, 235402 (2009).

[55] K. Zou and J. Zhu, Phys. Rev. B **82**, 081407 (2010).

[56] S.-G. Nam, D.-K. Ki, and H.-J. Lee, Phys. Rev. B **82**, 245416 (2010).

[57] E. H. Hwang and S. Das Sarma, Phys. Rev. B **77**, 115449 (2008).

[58] H. Min, E. H. Hwang, and S. Das Sarma, Phys. Rev. B **83**, 161404 (2011).

[59] D. S. L. Abergel, E. H. Hwang, and S. Das Sarma, Phys. Rev. B **83**, 085429 (2011).

[60] E. Arnold, Appl. Phys. Lett. **25**, 705 (1974).

[61] P. San-Jose, E. Prada, and D. S. Golubev, Phys. Rev. B **76**, 195445 (2007).

[62] J. H. Bardarson, J. Tworzydlo, P. W. Brouwer, and C. W. J. Beenakker, Phys. Rev. Lett. **99**, 106801 (2007).

[63] E. Louis, J. A. Verges, F. Guinea, and G. Chiappe, Phys. Rev. B **75**, 085440 (2007).

[64] R. Zallen and H. Scher, Phys. Rev. B **4**, 4471 (1971).

[65] T. P. Eggarter and M. H. Cohen, Phys. Rev. Lett. **25**, 807 (1970).

[66] X. Du, I. Skachko, A. Barker, and E. Andrei, Nature Nanotechnology **3**, 491 (2008).

[67] K. I. Bolotin, K. J. Sikes, J. Hone, H. L. Stormer, and P. Kim, Phys. Rev. Lett. **101**, 096802 (2008).

[68] M. Müller, M. Bräuninger, and B. Trauzettel, Phys. Rev. Lett. **103**, 196801 (2009).

[69] S. Kirkpatrick, Rev. Mod. Phys. **45**, 574 (1973).

[70] E. H. Hwang and S. Das Sarma, Phys. Rev. B **82**, 081409 (2010).

[71] E. H. Hwang and S. Das Sarma, Phys. Rev. Lett. **101**, 156802 (2008).

[72] S. V. Morozov, K. S. Novoselov, M. I. Katsnelson, F. Schedin, D. C. Elias, J. A. Jaszczak, and A. K. Geim, Phys. Rev. Lett. **100**, 016602 (2008).

[73] S. Xiao, J.-H. Chen, S. Adam, E. D. Williams, and M. S. Fuhrer, Phys. Rev. B **82**, 041406 (2010).

[74] J. B. Oostinga, H. B. Heersche, X. Liu, A. F. Morpurgo, and L. M. K. Vandersypen, Nat. Mater. **7**, 151 (2008).

[75] K. F. Mak, C. H. Lui, J. Shan, and T. F. Heinz, Phys. Rev. Lett. **102**, 256405 (2009).

[76] V. Cheianov, V. Fal'ko, B. Altshuler, and I. Aleiner, Phys. Rev. Lett. **99**, 176801 (2007).

[77] K. Nomura and A. H. MacDonald, Phys. Rev. Lett. **98**, 076602 (2007).

[78] C. Jang, S. Adam, J.-H. Chen, E. D. Williams, S. Das Sarma, and M. S. Fuhrer, Phys. Rev. Lett. **101**, 146805 (2008).

[79] S. Adam, S. Cho, M. S. Fuhrer, and S. Das Sarma, Phys. Rev. Lett. **101**, 046404 (2008).

[80] A. K. M. Newaz, Y. S. Puzyrev, B. Wang, S. T. Pantelides, and K. I. Bolotin, Nat. Commun. **3**, 734 (2012).

[81] K. S. Novoselov, A. K. Geim, S. V. Morozov, D. Jiang, Y. Zhang, S. V. Dubonos, I. V. Grigorieva, and A. A. Firsov, Science **306**, 666 (2004).

[82] D. Culcer, E. H. Hwang, T. D. Stanescu, and S. Das Sarma, Phys. Rev. B **82**, 155457 (2010).

[83] D. Kim, S. Cho, N. P. Butch, P. Syers, K. Kirshenbaum, J. Paglione, and M. S. Fuhrer, Nat. Phys. **8**, 460 (2012).

[84] D. B. Farmer, V. Perebeinos, Y.-M. Lin, C. Dimitrakopoulos, and P. Avouris, Phys. Rev. B **84**, 205417 (2011).

[85] C. R. Dean, A. F. Young, I. Meric, C. Lee, L. Wang, S. Sorgenfrei, K. Watanabe, T. Taniguchi, P. Kim, K. L. Shepard, and J. Hone, Nat. Nanotechnol. **5**, 722 (2010).

[86] S. Adam and S. Das Sarma, Solid State Commun. **146**, 356 (2008).

[87] S. Das Sarma and E. H. Hwang, Phys. Rev. B **83**, 121405 (2011).

[88] N. J. G. Couto, B. Sacépé, and A. F. Morpurgo, Phys. Rev. Lett. **107**, 225501 (2011).

[89] T. Stauber, N. M. R. Peres, and F. Guinea, Phys. Rev. B **76**, 205423 (2007).

[90] J. Yan and M. S. Fuhrer, Phys. Rev. Lett. **107**, 206601 (2011).

[91] J.-H. Chen, W. G. Cullen, C. Jang, M. S. Fuhrer, and E. D. Williams, Phys. Rev. Lett. **102**, 236805 (2009).

[92] M. Ishigami, J. H. Chen, W. G. Cullen, M. S. Fuhrer, and E. D. Williams, Nano Letters **7**, 1643 (2007).

[93] M. I. Katsnelson and A. K. Geim, Phil. Trans. R. Soc. A **366**, 195 (2008).

[94] W. Bao, F. Miao, Z. Chen, H. Zhang, W. Jang, C. Dames, and C. N. Lau, Nature Nanotech. **4**, 562 (2009).

[95] M. Monteverde, C. Ojeda-Aristizabal, R. Weil, K. Bennaceur, M. Ferrier, S. Guéron, C. Glattli, H. Bouchiat, J. N. Fuchs, and D. L. Maslov, Phys. Rev. Lett. **104**, 126801 (2010).

[96] T. O. Wehling, S. Yuan, A. I. Lichtenstein, A. K. Geim, and M. I. Katsnelson, Phys. Rev. Lett. **105**, 056802 (2010).

[97] D. K. Efetov and P. Kim, Phys. Rev. Lett. **105**, 256805 (2010).

[98] E. H. Hwang and S. Das Sarma, Phys. Rev. B **77**, 235437 (2008).

[99] L. A. Ponomarenko, R. Yang, T. M. Mohiuddin, M. I. Katsnelson, K. S. Novoselov, S. V. Morozov, A. A. Zhukov, F. Schedin, E. W. Hill, and A. K. Geim, Phys. Rev. Lett. **102**, 206603 (2009).

[100] F. Schedin, A. K. Geim, S. V. Morozov, E. W. Hill, P. Blake, M. I. Katsnelson, and K. S. Novoselov, Nature Materials **6**, 652 (2007).

[101] T. Kawamura and S. Das Sarma, Solid State Communications **100**, 411 (1996).

[102] M. Caragiu and S. Finberg, J. Phys.: Condens. Matter **17**, R995 (2005).

[103] S. Adam, E. Hwang, E. Rossi, and S. Das Sarma, Solid State Communications **149**, 1072 (2009).

[104] E. H. Hwang and S. Das Sarma, Phys. Rev. B **77**, 195412 (2008).

[105] R. Landauer, Electrical conductivity in inhomogeneous media, in *Electrical transport and optical properties of inhomogeneous media.*, edited by J. C. Garland and D. B. Tanner, p. 2, 1978.

[106] E. McCann, K. Kechedzhi, V. I. Fal'ko, H. Suzuura, T. Ando, and B. Altshuler, Phys. Rev. Lett. **97**, 146805 (2006).

[107] S. Adam and S. Das Sarma, Phys. Rev. B **77**, 115436 (2008).

[108] A. Deshpande, W. Bao, Z. Zhao, C. N. Lau, and B. J. LeRoy, Appl. Phys. Lett. **95**, 243502 (2009).

[109] H. Suzuura and T. Ando, Phys. Rev. Lett. **89**, 266603 (2002).

[110] S. V. Morozov, K. S. Novoselov, M. I. Katsnelson, F. Schedin, L. A. Ponomarenko, D. Jiang, and A. K. Geim, Phys. Rev. Lett. **97**, 016801 (2006).

[111] X. Wu, X. Li, Z. Song, C. Berger, and W. A. de Heer, Phys. Rev. Lett. **98**, 136801 (2007).

[112] F. V. Tikhonenko, A. A. Kozikov, A. K. Savchenko, and R. V. Gorbachev, Phys. Rev. Lett. **103**, 226801 (2009).

[113] I. Aleiner and K. Efetov, Phys. Rev. Lett. **97**, 236801 (2006).

[114] F. Stern, Surface Science **58**, 162 (1976).

[115] F. Stern and W. E. Howard, Phys. Rev. **163**, 816 (1967).

[116] P. M. Ostrovsky, I. V. Gornyi, and A. D. Mirlin, Phys. Rev. B **74**, 235443 (2006).

[117] B. Y. K. Hu, E. H. Hwang, and S. Das Sarma, Phys. Rev. B **78**, 165411 (2006).

[118] B. Dora, K. Ziegler, and P. Thalmeier, Phys. Rev. B **77**, 115422 (2008).